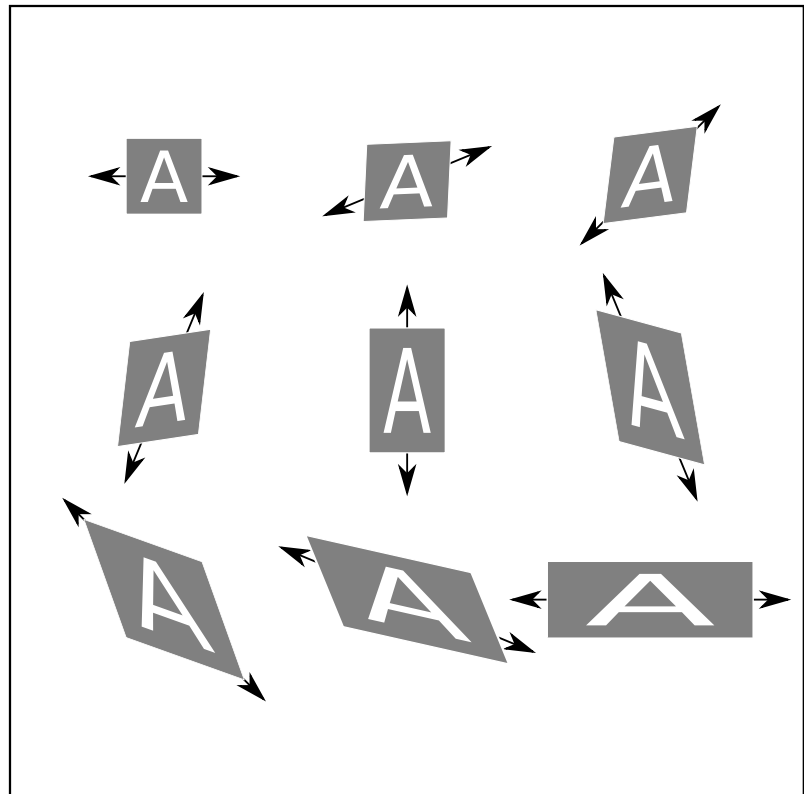


Matthew Scot Swan

Constitutive Modeling of the Densification Process of Ceramic Powders Subjected to Cold, Quasi-Static Pressing



UNIVERSITY OF TRENTO - Italy
Department of Civil, Environmental
and Mechanical Engineering



Doctoral School in Civil, Environmental and Mechanical Engineering
Topic 3. Modelling and Simulation - XXIX cycle 2014/2016

Doctoral Thesis - April 2017

Matthew Scot Swan

Constitutive Modeling of the Densification Process of Ceramic Powders Subjected to Cold, Quasi-Static Pressing

Supervisors

Davide Bigoni, University of Trento
Andrea Piccolroaz, University of Trento



Except where otherwise noted, contents on this book are licensed under a Creative
Common Attribution - Non Commercial - No Derivatives
4.0 International License

University of Trento
Doctoral School in Civil, Environmental and Mechanical Engineering
<http://web.unitn.it/en/dricam>
Via Mesiano 77, I-38123 Trento
Tel. +39 0461 282670 / 2611 - *dicamphd@unitn.it*

*Dedicated to my grandfather Mark Percival
who inspired me to be a scientist
and to my daughter, Arianne,
who I hope to inspire to explore
and learn throughout her life.*

Acknowledgements

This work was made possible the by the support that I have received from many people throughout my educational and professional career. In particular, I would like to thank Rebecca Brannon of the University of Utah for the help and guidance through my undergraduate and masters degrees that got me into the world of solid mechanics. I would also like to thank David Benson of the University of California, San Diego, for the guidance and tutelage during the first two years of my PhD studies. Finally, I would like to thank my current advisors, Andrea Piccolroaz and Davide Bigoni, for their help in continuing my education and giving me the freedom to explore these topics and encouraging me to do new things, explore the unexplored, and, above all, keep learning.

I also gratefully acknowledge financial support from the European Union's Seventh Framework Programme FP7/2007-2013/ under REA grant agreement number PITN-GA-2013-606878-CERMAT2.

Trento, March 23, 2017

Scot Swan

Contents

Acknowledgements	iii
Contents	v
List of Figures	ix
List of Tables	xix
Summary	xxi
Published papers	xxiii
Introduction	1
1 Test-Driven Development in Material Modeling Applications	7
1.1 Test-Driven Development Basics	8
1.2 Definition of a Simple Constitutive Model	9
1.3 Types of Tests	10
1.3.1 Unit Tests	10
1.3.2 Integration Tests (Module Tests)	11
1.3.3 System Tests (Verification Tests)	12
1.3.4 Regression Tests	13
1.4 Motivation for a Material Point Simulator	14
1.5 Equations for a Material Point Simulator	16
1.5.1 Prescribed Deformation Gradient Simulations	16
1.5.2 Prescribed Strain Simulations	18
1.6 Logarithmic Strain Rate vs. Deformation Rate (Unit and System Tests)	19
1.6.1 Driving Strain for Other Values of k	21
1.7 Tresca Verification Test	23
1.8 Conclusion	28

2	Application of Tomographic Reconstruction Techniques for Density Analysis of Green Bodies	29
2.1	Introduction	29
2.2	Presentation of the Method	31
2.3	Tomographic Reconstruction	32
2.3.1	Theoretical basis of tomography	33
2.3.2	Algebraic Reconstruction Technique	34
2.3.3	Number of Projections	36
2.3.4	Strengths and weaknesses of 2-projection ART	37
2.4	Virtual Experiment	39
2.5	Green Body Reconstruction	47
2.6	Conclusion	49
	Appendices	51
2.A	Moiré Diagrams	51
3	Constitutive Modeling of the Cold-Forming of Ceramic Powders	57
3.1	Introduction	57
3.2	Notation	58
3.3	Constitutive Model Theory	59
3.3.1	Cooper and Eaton Compaction Relation	59
3.3.2	Weighted Transition Law	61
3.3.3	Parameters Subject to the Weighted Transition Law	62
3.3.4	Elastic potential	63
3.3.5	Yield function	64
3.3.6	Nonassociativity	65
3.3.7	Combining the Constitutive Equations	66
3.4	Conclusions	69
	Appendices	71
3.A	Inverses of Selected Fourth-Order Tensors	71
3.B	Yield Function Gradient and Derivatives	76
3.C	BP Yield Surface Analysis	78
3.C.1	Asymmetrical Pressure-Dependence Term	78
3.C.2	Cap Shape Term	81
3.D	Parameterization for Classical Plasticity Models	91
3.D.1	Sphere	91
3.D.2	Elasticity	92
3.D.3	von Mises	92
3.D.4	Tresca	93

3.D.5	Linear Drucker-Prager	93
3.D.6	Principal Stress Cutoff	94
3.D.7	Mohr-Coulomb	94
3.D.8	Gurson	95
4	Parameterizing Tridentum for Alumina Powder KMS-	96
	Experiments	97
4.1	Experiments	97
4.1.1	Uniaxial Strain - Disk Forming	98
4.1.2	Ultrasonic Measurement of Elastic Parameters	101
4.1.3	Triaxial Compression and Extension	101
4.2	Hydrostatic Limit Parameters	102
4.2.1	Initial Pressure Cutoff p_{c0}	103
4.2.2	Initial Cohesion c_I	103
4.2.3	Cooper-Eaton Compaction ($a_1, a_2, \Lambda_1, \Lambda_2$) . .	104
4.3	Elasticity	106
4.3.1	Elastic Response from Ultrasonic Tests	106
4.3.2	Elastic Response from Triaxial Compression Tests	109
4.3.3	Elastic Response from Disk-Forming Tests . . .	109
4.3.4	Unifying Elasticity Parameters	111
4.4	Yield Surface Parameterization	113
4.4.1	Powder Phase Yield Surface Parameters	113
4.4.2	Compacted Phase Yield Surface Parameters . .	114
4.4.3	Using Triaxial Tests to Unify Yield Surface Pa- parameterizations	115
4.5	Parameters Not Mentioned	116
4.6	Inverse Analysis Using a Material Point Simulator . .	116
4.6.1	Basic Response	117
4.6.2	Optimized Response	119
4.7	Conclusion	121
	Appendices	123
4.A	Tridentum Inputs for Alumina Powder	123
5	Green Body Truncated Cylinder Experiment and Sim-	127
	ulation Comparison	127
5.1	Introduction	127
5.2	Model Validation against Experimental Results	128
5.3	Evaluation of the Predictive Capabilities	129
5.4	Conclusions	134
6	Conclusions	137

List of Figures

- 1.1 A graphical representation of a rotating constant uni-axial strain rate operating on glyphs (discussed in Section 1.6). Note, the loading direction is undergoing rotation, not the glyph itself. The initial condition is in the top-left corner and is read left-to-right, top-to-bottom and in time increments of $\Delta t = 0.25$ 20

- 1.2 A comparison of the deformation and deformation rate of the strain and symmetric part of the velocity gradient. The analytical solution is derived in Section 1.6 and a graphical representation is shown in Figure 1.1. The parameter $a = 1/2$ such at at time $t = 2$ the logarithmic axial strain is 1. 22

- 1.3 A representation in the deviatoric plane of the verification test in Section 1.7. The blue line represents the yield surface and the red arrows represent the loading legs of the test. The initial and final states are coincident at the origin. 23

- 1.4 Plots showing the principal strains (top) and the principal stresses (bottom) of the Tresca verification test using $\psi = 15^\circ$, $Y_s = 1\text{MPa}$, and $G = 1\text{GPa}$. The thick, gray lines are the analytical solution and the dotted lines are the response predicted by a model written in Fortran driven by strain. 26

2.1	Texture of a 10g alumina green body formed by 120MPa mean axial stress in the shape of a truncated cylinder with 30mm diameter and 10° incline in the process of being milled. The left portion of the sample is the smooth, inclined surface that was created by the mold during pressing. The other surfaces are created by the milling process and demonstrate the rough but uniform texture produced by the CNC mill in the cutting process. The vertical difference between successive layers is 1mm (e.g. the step between the surfaces in the top-right and bottom-right of the image).	32
2.2	A body with a continuously-varying density field $f(x, y)$ is projected in the direction θ and is gathered into m bins denoted P_j of the projection P . Multiple projections along different values of θ are used to reconstruct the density field $f(x, y)$	34
2.3	An example of a phantom/sinogram pair. The sinogram was produced using the open-source <code>scikit-image</code> Python library. The analysis domain consists of the inscribed black circle with the white circle and square inclusions. The analysis domain is circular such that the cross-section width is uniform for all projection angles. Notice that, as the projection direction changes in the sinogram, the circle's projection is constant while the square's projection has two intertwining density peaks (from the corners of the square) that both have a period of 180°.	35
2.4	A demonstration of why a 2-projection reconstruction is conducive to reconstructing on a cartesian grid, such as a digital image. Compare with the arbitrary nature of Figure 2.2. When more than the two projections in the principal directions ($\theta = 0^\circ, 90^\circ$), it is then necessary to determine how to partition the projections into cells that span multiple columns or rows.	38
2.5	A demonstration of the strengths and weaknesses of the 2-projection (vertical and horizontal) additive, multiplicative, mixed, and simultaneous algebraic reconstruction technique (ART). The plots are based on the function $f(x, y) = e^{-(2x^2+10y^2)}$. Note: the reconstruction in (e) is an exact reconstruction of the image in (a).	40

2.6	A demonstration of the strengths and weaknesses of the 2-projection (vertical and horizontal) additive, multiplicative, mixed, and simultaneous algebraic reconstruction technique (ART). The plots are based on the function $f(x, y) = e^{-(2x^2+10y^2)}$, rotated by 30° . These plots demonstrate how the 2-projection ART is unable to correctly capture the rotation of the density field.	41
2.7	A demonstration of the strengths and weaknesses of the constrained 2-projection (vertical and horizontal) additive, multiplicative, mixed, and simultaneous algebraic reconstruction technique (ART). The plots are based on the function $f(x, y) = e^{-(2x^2+10y^2)}$, rotated by 30° and solved under the constraint that all points outside the unit circle are zero. The reconstruction using multiplicative ART (e)(f) did not converge.	42
2.8	A demonstration of the strengths and weaknesses of the 2-projection (vertical and horizontal) additive, multiplicative, mixed, and simultaneous algebraic reconstruction technique (ART). The plots are based on the function $f(x, y) = 1 - e^{-(2x^2+10y^2)}$	43
2.9	A demonstration of the strengths and weaknesses of the 2-projection (vertical and horizontal) additive, multiplicative, mixed, and simultaneous algebraic reconstruction technique (ART). The plots are based on the function $f(x, y) = 1 - e^{-(2x^2+10y^2)}$, rotated by 30°	44
2.10	A demonstration of the strengths and weaknesses of the constrained 2-projection (vertical and horizontal) additive, multiplicative, mixed, and simultaneous algebraic reconstruction technique (ART). The plots are based on the function $f(x, y) = 1 - e^{-(2x^2+10y^2)}$, rotated by 30° and solved under the constraint that all points outside the unit circle are zero. The reconstruction using multiplicative ART (e)(f) did not converge.	45

2.11	A virtual experiment where a representative density field is extracted from a ceramic powder compaction simulation and reconstructed from two orthogonal projections using multiplicative ART. The ART reconstruction method adequately reconstructs the density simulated field, although it does smooth along the projection directions. Because the method is insensitive to the magnitude of the density, the density field of the simulated green body is normalized according to the average density of the slice.	46
2.12	A demonstration of the method to regularize the projections in the presence of experimental variation (such as flaking) during the milling process. The experimentally-measured mass can be converted to density by dividing by projection-element volume (found by using sample geometry and milling path). The density profile can then be smoothed by minimizing a mass-weighted root-mean-squared error function while requiring total mass to be unchanged.	48
2.13	Visualized experimental data on a truncated cylindrical green body made of alumina powder (see Figure 2.1 for geometry specifications). All densities are given in kg/m^3 with $1200\text{kg}/\text{m}^3$ as the uncompressed powder density and $2400\text{kg}/\text{m}^3$ as the green density at 100MPa. The projections have been smoothed and then re-sampled from a strip width of 1.5mm to 0.1mm.	50
2.A.1A	A single projection of a 2D gaussian function $f(x, y) = e^{-(2x^2+12.5y^2)}$, rotated by 20° where the domain of interest is the unit circle. This demonstrates a vertical projection into mass, area, and density data.	52
2.A.2A	A graphical depiction of how to determine line spacing for the Moiré projection. The red lines are equally spaced along the ordinate, with the black lines being equally spaced between the red lines. Because the integral is strictly monotonic, the transformation from the evenly-spaced values along the ordinate to the abscissa is unique and easily found given the piecewise-linear nature of the integral.	53

2.A.3	Reconstruction of a 2D gaussian function $f(x, y) = e^{-(2x^2+12.5y^2)}$, rotated by 20° (compare with Figure 2.7) where the domain of interest is the unit circle. The rotation angle of 20° was chosen so as to be large enough to be noticeable and yet not coincide with any of the projections, a worst-case scenario for determining orientation. The red axis protruding out of each circle is included only to demonstrate the angle by which the 2D gaussian was rotated.	55
3.1	A demonstration of how to parameterize the Cooper and Eaton compaction relation using Martoxid KMS-96 alumina powder. A comparison with the small-strain version is included to demonstrate that it underpredicts by a large margin the volumetric plastic strain for a given forming pressure and is unable to achieve the manufacturer-recommended green body density at 100MPa.	61
3.C.1A	plot of the asymmetrical pressure-dependence term from the meridional function of the yield surface.	80
3.C.2A	plot of the cap shape term from the meridional function of the yield surface. Note that at $\Phi = 1/2$ the function is always equal to unity for all values of α	81
3.C.3	Plots of the total meridional shape term for various values of m and α . Notice that, for $\alpha = 1$ the upper bounds are exact.	84
3.C.4A	3D plot depicting the Φ -location of the maximum permissible shear for given values of α and m . Not surprisingly, the ϕ value at maximum approaches unity as m increases.	85
3.C.5A	3D plot depicting the ratio of the upper bound of the maximum permissible shear (Equation 3.110) divided by the actual maximum permissible shear for common ranges of α and m	86
3.C.6A	plot depicting the Φ -location of the maximum permissible shear over the entire domain of α of the total meridional shape term for $m = 2$	88

3.C.7A	plot depicting the θ_c -location of the minimum of $g(\theta_c)$ for various values of β and γ . The black grid shows the contours for constant β or γ . The blue lines depict the contours of constant θ_c . The lower plateau is at $\theta_c = 0$ which is triaxial extension, while the upper plateau is at $\theta_c = \pi/3$ which is triaxial compression.	89
3.C.8A	plot of $\max(g(\theta_c))$ for all allowable values of γ and β . Note the symmetry around the $\beta = 1$ line.	90
4.1	A demonstration of the difference of the machine-reported crosshead displacement with the displacement as measured by a transducer for a disk-forming experiment with a maximum load of approximately 56kN. The press is a Beta 100 from Messphysik Materials Testing and the transducer is a PY-2-F-010-S01M external displacement transducer from Gefran Italy. The working limit of the equipment (press and load cell) is 100kN.	99
4.2	A demonstration of the effects of vibrating the sample while in the mold prior to the test. Each test is of 6g of alumina powder. Note the significant difference in strain to produce the same target stress between vibrated and non-vibrated samples. The average initial density of the unvibrated samples is 1120kg/m ³ and 1320kg/m ³ for the vibrated samples.	100
4.1	Plot of the experimental data and the calibrated Cooper-Eaton compaction law.	105
4.1	Plots of the elastic moduli (top) and Poisson's ratio (bottom) with respect to forming pressure for alumina powder. In each plot, the markers represent the ultrasonic experimental data and the solid lines represent the model interpolation function.	107

4.2	Compressive axial stress versus compressive axial strain from triaxial compression tests of alumina powder. The triaxial tests were all loaded hydrostatically to 40MPa, then unloaded hydrostatically to one of 2MPa, 10MPa, 15MPa, 20MPa, and 30MPa. At that point, the lateral stresses were held constant with increasing axial pressure. The dashed lines represent stress assuming a constant cross-section during compression and the dashed-dotted line assumes constant volume. Young's modulus was calculated from the initial slopes as 0.59GPa, 2.19GPa, 3.12GPa, 3.81GPa, and 5.60GPa for the 2MPa, 10MPa, 15MPa, 20MPa, and 30MPa tests, respectively, and is depicted by the solid tangent lines.	108
4.3	The tail-end of compressive axial stress versus compressive axial strain of uniaxial strain compression tests on alumina powder. The black lines are the linear regressions of the unloading portion, neglecting the spurious tail. The slope of the linear regressions are, by definition, the constrained modulus.	110
4.4	The ratio of the constrained modulus to Young's modulus versus Poisson's ratio. This plot is a union of the elastic modulus information from the triaxial compression data (Figure 4.2) and the uniaxial strain data (Figure 4.3). Compare the range of Poisson's ratios with that of the ultrasonic test data (Figure 4.1). Note: the last two points (with "X" markers) are undefined as M cannot be less than E (which would yield an imaginary Poisson's ratio).	111
4.1	A plot in isomorphic stress space depicting the triaxial compression (positive r) and triaxial extension (negative r) experimental data with the evolution of the fitted yield surface. The red yield surface is the 40MPa yield surface that the data points were fitted to. The evolution of the yield surface is depicted with preconsolidation pressures of 2MPa, 5MPa, 10MPa, 20MPa, 40MPa, 60MPa, 80MPa, and 100MPa.	115

4.1	Plots comparing the simulated response using the tentative parameterization to the experimental data for disk-forming experiments. The upper plot shows the stress-strain response while the lower compares the axial stress and axial logarithmic plastic strain. Note, in the lower plot each data point represents a single disk-forming experiment.	118
4.2	Plots comparing the simulated response using the optimized inverse-analysis parameterization to the experimental data for disk-forming experiments. The upper plot shows the stress-strain response while the lower compares the axial stress and axial logarithmic plastic strain. Note, in the lower plot each data point represents a single disk-forming experiment.	120
5.1	A cross-section of the truncated cylinder experimental setup.	129
5.1	Comparison of the reconstructed density fields from the experiment (top) and the simulation (bottom) from the production of a truncated cylinder from alumina powder. All densities are given in kg/m^3 with $1200\text{kg}/\text{m}^3$ as the uncompressed powder density and $2400\text{kg}/\text{m}^3$ as the manufacturer-reported green density at 100MPa. The true measure of the accuracy of the model is related to how well the reconstructed fields agree. Regions of low density along the inclined surface of the simulation are non-physical effects of the reconstruction process.	130
5.2	A comparison of the force-displacement data for the experiment and simulated green body forming. The simulation was driven by imposing a prescribed displacement on the punch. The excess simulated load is likely due to inaccuracies in the implementation of friction (e.g. incorrect friction coefficient or non-realistic friction law).	131
5.3	A 3D view of the final simulated density field. Inclined surface facing up.	132
5.4	A view of the top (inclined surface) of the final simulated density field. Thinnest section on top.	132
5.5	A view of the bottom (punch surface) of the final simulated density field. Thinnest section on top.	133

5.6	A view of the inside of the final simulated density field. Inclined surface facing up.	133
5.7	A probability density function (PDF) and cumulative density function (CDF) for the density distributions of the reconstructed experimental density field, reconstructed simulated density field, and the actual simulated density field. Note: the median values for the simulated distributions are coincident.	135

List of Tables

1.1	Table of piecewise-linear principal strains and stresses for the Tresca verification benchmark. The time-fraction at which the vertex is reached in each plastic step is $\eta = (3 - \sqrt{3})/6$, the yield in shear is Y_s , and the shear modulus is G . As the state at the end of step 1 and step 7 are equivalent, it is possible to traverse the yield surface multiple times by repeating steps 2-7. Note that the strains at vertices $(i + \eta)$ are for reference as the strain rate is constant though each step (from i to $i + 1$).	27
3.A.1	Eigensystem of the fourth-order tensor from Equation 3.49.	74
3.C.1A	table of absolute maximum and minimum values for the constituent functions of the BP yield surface. This table takes into account all possible parameter values and combinations. Values with a * denote an exclusive interval endpoint.	78
3.C.2A	table of bounded maximum and minimum values for the constituent functions of the BP yield surface. This table takes into account all possible parameter values and combinations and attempts to give better bounds than in Table 3.C.1. *Exclusive interval endpoint. **This minimum for $g(\theta_c)$ is not a tight bound (see Equation 3.127).	79
4.A.1	The final parameterization for the material model Tridentum for alumina powder.	123

Summary

The present research is focused on the numerical modeling of the compaction of ceramic powders to form green bodies. The primary deliverables are:

- The formulation of a constitutive model which combines many advanced techniques such as nonlinear elasticity, pressure- and Lode angle-dependent plasticity, elastoplastic coupling, and nonassociativity.
- The numerical implementation of the above-mentioned constitutive model in Fortran95 to be used in full-featured finite-element codes.
- A new method for assessing internal density inside green bodies using readily available laboratory equipment. This method utilizes tomographic reconstruction techniques to reconstruct a density field from two projections. The projections are produced using the green body geometry, an analytical balance, and a CNC mill.
- An assessment of the application of test-driven development (TDD) to the development of the numerical material model and extensive verification of the numerical routine. These principles were found to be essential for the proper development of the model.

The above four points advance the body of scientific knowledge by enabling industry and research institutions to predictively simulate the densification process, evaluate the density fields, and produce quality numerical codes for use in production environments.

Published papers

The main results presented in this thesis have been summarized in the following papers:

1. M.S. Swan, A. Piccolroaz, and D. Bigoni.
Application of tomographic reconstruction techniques for density analysis of green bodies. *Ceramics International*, 2017, volume 43, 749-754;
2. M.S. Swan and T.J. Fuller.
A Case Study of Test-Driven Development in Material-Modeling Applications. *Submitted for publication*;
3. M.S. Swan, A. Piccolroaz, D. Bigoni, A. Gajo, and S. Stupkiewicz.
Constitutive modeling and experimental results of cold forming of ceramic powders. *Not yet submitted*;

Introduction

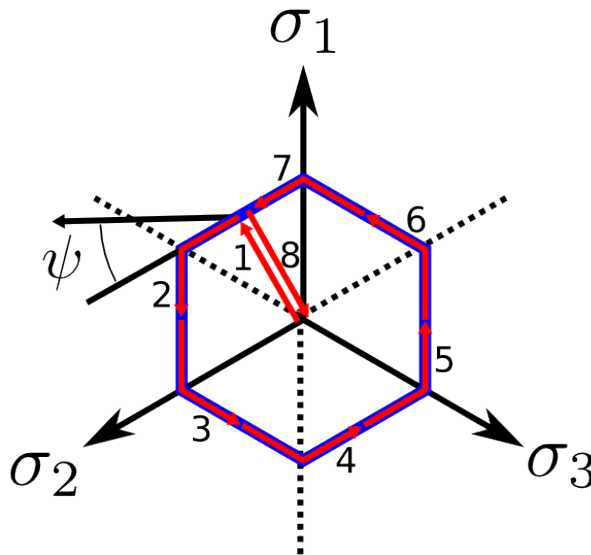
The consistent, uniform pressing of green bodies is a necessary part of producing high-quality, high-performance ceramics with predictable qualities and behavior. Undesirable density variation in the compacted ceramic powder causes variability in performance, failure to meet quality control standards, and, possibly, complete piece failure during successive processing. These issues contribute directly to a decrease in production efficiency through lost time and an increase in energy and material use. The careful control of the green body density field is of the utmost importance to consistently producing high-performance ceramics. Current methods for minimizing heterogeneity of the density field are often based on trial-and-error to optimize mold geometry and forming pressure, which is both expensive and prolongs development. The present research presents a continuum-level constitutive model for accurately modeling the densification of ceramic powders into green bodies and outlines the numerical implementation of said model. The constitutive model incorporates non-linear elasticity, elastic-plastic coupling, cap evolution, pressure- and Lode angle-dependent plasticity, and hardening. To evaluate the constitutive model, a new method for measuring density in green bodies has been developed. This method utilizes readily-available laboratory equipment to produce density projection data for the sample and subsequently processes that data to produce a 3D density field using well-developed tomographic reconstruction techniques. Finally, a green body is produced from alumina powder (Martoxid KMS-96) and the density field is evaluated and compared to that of a numerical simulation. They are shown to agree within the error of the density measurements. These comparisons demonstrate the performance of the developed constitutive model and the potential utility for companies and research institutions that are in the ceramics production field.

Test-Driven Development in Material Modeling Applications

This chapter focuses on the programming paradigm used to create a material model because the quality of the model is directly related to the quality of the coding. The programming paradigm of Test-Driven Development (TDD) has been found to work very well with constitutive model development.

The basis of TDD is that of “tests done first” as opposed to “tests done last” or “tests done never.” Specifically, before any functionality is added to a model the developer writes automated tests that cover the entire range of functionality. After the tests are written, the entire testing suite is run and the developer verifies that all tests pass except the newly added ones (for which the functionality has not yet been added). Then the functionality is added and is deemed sufficient when all the tests pass.

This chapter contains a development example Tresca perfect plasticity model with isotropic, linear elasticity. As functionality of the model is expanded, sample (but not exhaustive) tests are suggested. Finally, a system-level test is presented where the stress path traverses all six sides of the yield surface and returns to the origin, as shown below.



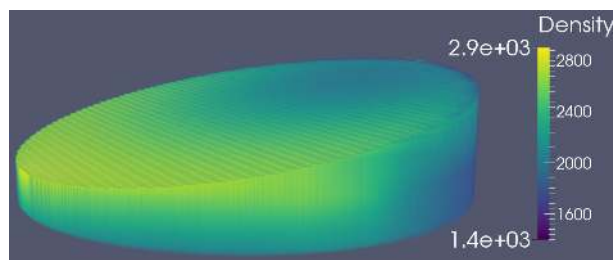
Application of Tomographic Reconstruction Techniques for Density Analysis of Green Bodies

Progress in the manufacturing of ceramics, but also of sintered metals, strongly relies on the evaluation of the density distribution in green bodies. The importance of density in green bodies is related to the heterogeneity of the density field in the green body. Density variation is associated with residual stresses and residual strains which cause breakage during sintering and/or variability in performance.

Significant resources have been poured into addressing the issues of density field heterogeneity within the ceramics industry, but is usually addressed on a per-product basis through the process of trial-and-error. This chapter focuses on comparing green-body density fields to the density fields produced by numerical models. When the numerical models demonstrate that they can consistently reproduce the actual density fields they can then be used in virtual prototyping. Virtual prototyping of cold-pressed ceramic powders can increase production efficiency by decreasing the defect rate, increasing product performance, and decreasing development time.

The presented method utilizes the concepts of tomographic reconstruction with a CNC mill and analytical balance to produce 3D density fields. As an example, a green body made of alumina powder (KMS-96) is produced in the form of a truncated cylinder with a radius of 15mm and a face inclined by 10° . It is processed with the CNC mill and analytical balance and that data is transformed into a 3D density field as shown below.





Constitutive Modeling of the Cold-Forming of Ceramic Powders

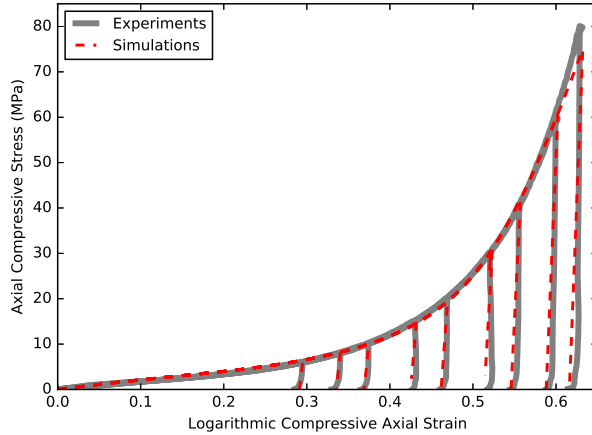
A presentation of equations for a new material model, called **Tridentum**, that is focused on predictive modeling of the cold-forming process of ceramic powders. The model is capable of simulating the material response from the initial loose-powder state all the way to fully consolidated. This model is the natural successor to the density analysis through tomographic reconstruction techniques as the primary goal is to accurately model the forming process.

The model **Tridentum** incorporates nonlinear elasticity with induced anisotropy, a pressure and J_3 dependent yield surface (the BP yield surface), elastoplastic coupling, and nonassociativity. The initial state is defined by nonlinear elasticity with induced anisotropy and a Bigoni-Piccolroaz yield surface. The final state is defined by isotropic, linear elasticity with a Bigoni-Piccolroaz yield surface. The transition between the two states is characterized by the elastoplastic coupling and the transition function.

Parameterizing Tridentum for Alumina Powder KMS-96

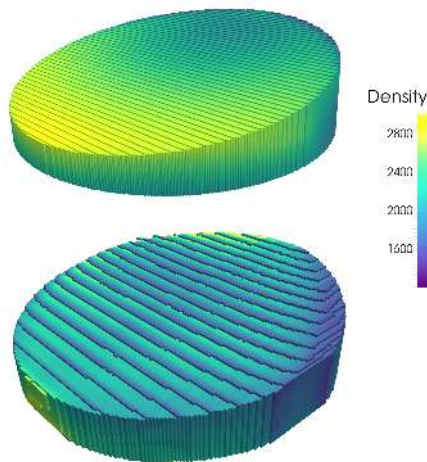
The complex material model **Tridentum** has nearly 30 user inputs. This chapter guides the reader through the process of taking disk forming, triaxial extension, triaxial compression, and ultrasonic experiments to get a parameterization for a given material. It also shows the intermediate steps of fitting and optimization of parameters, and justifies any assumptions made. Finally, it shows the application of inverse analysis to further improve the parameterization. The final parameterization is able to reproduce experimental data to a sufficient degree of accuracy, as shown below where a comparison between a uniaxial deformation test on a ceramic powder (alumina)

is compared to its numerical simulation using the Tridentum model.



Results

The predictive capabilities of the model has been demonstrated with the following comparison of density fields from a numerical simulation and an experiment. The density fields were compared in a reconstructed space after evaluating projections and reconstructing them using tomographic reconstruction methods. The reconstructed density fields agreed to a large extent and give confidence that the model is accurately predicting the actual density field of the green body.



In this image, the upper body is the reconstructed density field (as discussed in the above section of Tomography) and the lower body is

the reconstructed density field from the simulation. Mesh sensitivity caused the actual density field to be asymmetric and that asymmetry was amplified by the reconstruction process.

Test-Driven Development in Material Modeling Applications

As more and more scientific experiments are performed in silico, there is a greater need for scientists to be computationally literate and capable of producing quality code and editing the code of others. This has caused an influx of scientists that write code as part of their research but that lack any substantial formal training in software development, particularly concerning software testing. The seriousness of this absence of formal instruction in software testing is underscored by the fact that even computer science graduates often are not trained[21]. This lack of proper training causes an increase in software maintenance costs and buggier software[71], with the added consequence of previously-made software being abandoned because of a lack of comments, readability, or stability and the eventual reproduction of work. Here, the case for the use of Test-Driven Development (TDD) as a way for scientists to produce better code with fewer bugs and that is easier to understand is presented. The case for exercising models using a material point simulator is discussed with analytic solutions for conversions between deformation measures as well as a system-level analytical verification test of a Tresca plasticity model. Scientists performing numerical modeling are in a unique situation where many aspects of their code can easily be tested against analytical solutions.

The skill of material model development has become much more prevalent in recent decades as the number of computers has increased and the number of scientists creating models has increased. The creation of constitutive models is usually treated as a necessary step of a much larger process that yields a global result and, as it is only one step, is often glossed over and not given the proper attention.

The role of a constitutive model is to implement constitutive equations in a manner consistent with the response of a given material over the domain of interest such that the system of equations for simulation is closed. Constitutive models are necessary because the laws of conservation of mass, conservation of momentum, conservation of

energy, *etc.* do not form a closed system of equations. Many companies and laboratories have invested resources over decades to the development of simulation frameworks that can efficiently solve particular types of differential equations. However, all of these solvers need constitutive models to close the system to provide a solution.

Regrettably, material modeling and model parameterization are often an afterthought, with the common solution of using isotropic, linear elasticity and, if plasticity is warranted, von Mises plasticity to describe the materials. This is a common pitfall as the constitutive relations are just as important as the conservation of momentum and the limits of applicability of the material model limit the credibility of the simulation as a whole.

This chapter focuses on the development of the material model, from the inception to the final verification testing, with an eye to minimizing bugs and ensuring consistent, correct behavior with fewer faults and faster development.

1.1 Test-Driven Development Basics

Before a material model is created, the governing equations are first conceived. This step defines what properties the model will have, such as:

- isotropic, linear elasticity; Hyper-elasticity; Hypoelasticity;
- viscosity; Rate dependence;
- Perfect plasticity, isotropic or kinematic hardening;
- elastoplastic coupling;
- piezoelectric response;
- Associativity or nonassociativity;

All of these characteristics are decided before any code is written or even before a programming language is chosen and offer a convenient partitioning of the model into independent (or quasi-independent) modules.

The fact that the model is planned out at a high level before any code is written is a great benefit because it lends itself to the programming paradigm of Test-Driven Development (TDD). The basis of TDD is that of “tests done first” as opposed to “tests done last”

or “tests never done”. Regrettably, as many of the constitutive modelers are not software developers by trade, they lack the fundamental knowledge of programming best practices, such as self-documenting code, leaving useful comments when the code isn’t self-documenting, unit tests, automated testing, or even a consistent style. Even trained software developers are not always trained in these things[71]. TDD is effective at minimizing bugs and ensuring code maintainability through thorough testing[73]. When programming under TDD, the programmer takes a single concept that is to be implemented and writes a battery of automated tests that covers that one concept and that one concept only. Ideally, the agglomeration of tests will cover every aspect of the desired functionality including edge cases and every possible branch combination. After the test suite is created, the test suite is run to verify that every new test will fail, as expected, because the desired functionality has not yet been implemented. Then the programmer implements the functionality and can be assured that it has been implemented correctly when all of the tests in the test suite pass.

The true benefit to the constitutive modeler is that often the basic equations governing material behavior have analytical solutions. Even the most complicated equations or even the entire model usually have some analytical solutions for contrived cases, such as setting parameters to mimic isotropic, linear elasticity. The modeler is then able to make tests for each function, module, and class in the code to get complete code coverage.

The existence and frequent use of these tests ensures that incremental changes to the model do not depart from known correct behavior and that previous bugs are not re-introduced (regression testing). All of these aspects combine to produce code that is more stable, better documented (each test is, in a way, documentation), and better designed[55].

1.2 Definition of a Simple Constitutive Model

The test examples given in this document are all based around a simple elastic, perfectly-plastic model. The elastic response is that of isotropic, linear elasticity with the Tresca yield surface for the plastic part. Specifically, the Cauchy stress-logarithmic strain relation is given

$$\sigma = K \operatorname{tr} \varepsilon I + 2G \operatorname{dev} \varepsilon \quad (1.1)$$

with K and G being the elastic bulk and shear moduli, respectively. The yield function is defined

$$F = \sqrt{J_2} \cos \theta_s - Y_s = \sqrt{J_2} \cos(\theta_c - \pi/2) - Y_s \quad (1.2)$$

with the yield surface defined by the zero-isosurface of the yield function.

1.3 Types of Tests

Many software developers, let alone scientist-programmers, do not actually perform in-depth tests on the code that they have created. Often, a couple of “sanity checks” after the code is finished is erroneously deemed sufficient. Given such an environment, it is important to define different types of tests and exactly what is meant here when they are mentioned:

- Unit tests
- Integration tests (Module tests)
- System tests (black box tests)
- Regression tests.

Each of these things is meant to assist in the creation of stable, maintainable, and understandable code.

1.3.1 Unit Tests

These are intended to test small pieces of code called ‘units’. The existence of these tests helps the programmer adhere to the guideline of “write short units of code”[72]. While the definition of “short” varies, most texts on the matter suggest that each unit (function, subroutine, *etc.*) contain around 15 lines of code. The reasoning behind shorter segments of code is that the defect density (bugs per line of code) goes up with longer segments of code[53]. So, given the same number of lines, there would be more defects in the version where everything is done in a single subroutine than there would be in the version that has been segmented into smaller blocks of code. The shift from legacy code where there is only a single subroutine that spans 20,000 lines is a far cry from the ideal of around 15 lines of code per unit of code.

As most modern languages support Object-Oriented Programming (OOP), it becomes easier to break down each part of the constitutive model into individual units. For example, calculating the isotropic or deviatoric part of a tensor, evaluating the yield function, or calculating the elastic stiffness could all be individual units of code. While it would be possible to find the stress deviator inside of the primary subroutine in a model, when it is isolated into a single unit of code it can be thoroughly tested and reused in other parts of the code, decreasing code repetition.

Elastic Unit Test

A sample unit test for the elastic portion of the model is to set

$$K = 8 \quad G = 3 \quad \varepsilon = \begin{bmatrix} 2 & 0 & 0 \\ 0 & 1 & 0 \\ 0 & 0 & 0 \end{bmatrix} \quad (1.3)$$

and verify the output is

$$\sigma = \begin{bmatrix} 30 & 0 & 0 \\ 0 & 24 & 0 \\ 0 & 0 & 18 \end{bmatrix}. \quad (1.4)$$

Yield Function Unit Test

A sample unit test for the yield function of the model is to set

$$Y_s = 1 \quad \sigma = \begin{bmatrix} 1 & 0 & 0 \\ 0 & 0 & 0 \\ 0 & 0 & -1 \end{bmatrix} \quad (1.5)$$

and verify that the yield function gradient at that point is

$$\frac{\partial F}{\partial \sigma} = \frac{1}{\sqrt{2}} \begin{bmatrix} 1 & 0 & 0 \\ 0 & 0 & 0 \\ 0 & 0 & -1 \end{bmatrix}. \quad (1.6)$$

1.3.2 Integration Tests (Module Tests)

In the context of a material model, a module could be considered as the aggregation of the smaller units of code with a common characteristic. An example of this would be a module that controls the behavior of the yield surface containing individual units for the yield function, yield surface normal, and hardening parameters. Module

tests make use of multiple sub-units of code and increase confidence that the code is functioning as expected at each level.

One of the more important components to check with a module-level tests is the return algorithm. While it is very common to have very complex physics present for the return algorithm, usually a pathological case can be developed where the return can be analytically determined. Good candidates are hydrostatic loading or pure-shear loading.

Module-level tests can also make use of other functions to assist in the testing. A common problem for very complicated models is the difficulty in deriving or lack of analytical solutions from which testing can occur. In a module-level test, one could use the previously-tested yield function to numerically generate the yield function derivative as an additional check that coded version of the yield function derivative is correct. This allows at least some testing to happen in areas where the analytic solutions are intractable. This same technique is applicable for any other derivative or integral made in the model to ensure that the model is self-consistent but should not take the place of thorough unit testing. The benefits of these numerical tests are based entirely on correctly and thoroughly testing the individual units upon which they depend.

Return Algorithm Module Test

Two sample module tests for the return algorithm are

$$Y_s = 1 \quad \sigma^{\text{trial}} = \begin{bmatrix} 2 & 0 & 0 \\ 0 & 0 & 0 \\ 0 & 0 & -2 \end{bmatrix} \quad \sigma^{\text{ret}} = \begin{bmatrix} 1 & 0 & 0 \\ 0 & 0 & 0 \\ 0 & 0 & -1 \end{bmatrix} \quad (1.7)$$

and, with $Y_s = 1$,

$$\sigma^{\text{trial}} = \begin{bmatrix} 2 & 0 & 0 \\ 0 & -1 & 0 \\ 0 & 0 & -1 \end{bmatrix} \quad \sigma^{\text{ret}} = \frac{2}{\sqrt{3}} \begin{bmatrix} 2 & 0 & 0 \\ 0 & -1 & 0 \\ 0 & 0 & -1 \end{bmatrix} \quad (1.8)$$

for a pure shear return and a return to a vertex, respectively.

1.3.3 System Tests (Verification Tests)

System testing (or verification testing or black-box testing) is performed on the whole model using only the publicly-available call signature. This is the most common test as most software developers

perform some “sanity checks” or “smoke checks” by manually running the model in such a way that some simple behavior can be easily checked against a known solution. A common solution is setting the yield surface to infinity and observing isotropic, linear elasticity.

However, with modern testing frameworks there is no reason that these tests should not be automated and run consistently. Most models can be degenerated to simpler constitutive models, such as the above-mentioned elastic-plastic model mimicking isotropic-linear elasticity or a non-linear elastic model being set to mimic isotropic-linear elasticity. More complicated models can benefit from the analytical solutions from sources such as [10][42][47] that give analytical solutions to basic plasticity models like von Mises plasticity (with and without hardening) or linear Drucker-Prager.

Single-Step Verification Test

Given the initial condition

$$\sigma^{\text{init}} = \begin{bmatrix} 0 & 0 & 0 \\ 0 & 0 & 0 \\ 0 & 0 & 0 \end{bmatrix} \quad \varepsilon^{\text{init}} = \begin{bmatrix} 0 & 0 & 0 \\ 0 & 0 & 0 \\ 0 & 0 & 0 \end{bmatrix} \quad (1.9)$$

$$K = 8 \quad G = 3 \quad Y_s = 1 \quad (1.10)$$

and driving it with a strain increment of

$$\Delta\varepsilon = \begin{bmatrix} 1 & 0 & 0 \\ 0 & 0 & 0 \\ 0 & 0 & -1 \end{bmatrix} \quad (1.11)$$

the expected output stress is

$$\sigma^{\text{final}} = \begin{bmatrix} 1 & 0 & 0 \\ 0 & 0 & 0 \\ 0 & 0 & -1 \end{bmatrix}. \quad (1.12)$$

Multiple-Step Verification Test

An example of a tests covering more than a single step is discussed later in Section 1.7.

1.3.4 Regression Tests

When the code has reached the point where it starts being exercised, eventually bugs will be found and reported. After code inspection

and finding what when wrong, the problem is fixed and a new version released. However, the inclusion of a regression test is important to ensure that old bugs are not re-introduced into the code. Usually, regression tests are kept primarily to ensure that customer-specific functionality is maintained and that the same bug is never seen twice.

Yield Function Regression Test

Suppose that the following yield function, as given in [22][52]), was used instead of Equation 1.2

$$F = 4J_2^3 - 27J_3^2 - 36k^2 J_2^2 + 96k^4 J_2 - 64k^6. \quad (1.13)$$

Eventually, a user might encounter odd plastic behavior near the vertices of the yield surface. After investigating the problem, it is discovered that the new yield function has false elastic domains[10] and the yield function is changed to the one given in 1.2. Adding a regression test ensures that those false elastic domains do not return into the code base. A possible regression test has the inputs

$$Y_s = 1 \quad \sigma = \begin{bmatrix} 2 & 0 & 0 \\ 0 & -1 & 0 \\ 0 & 0 & -1 \end{bmatrix} \quad (1.14)$$

and the output

$$F = \frac{\sqrt{3} - 2}{2}. \quad (1.15)$$

1.4 Motivation for a Material Point Simulator

There are many benefits to using a material point simulator, most of which fall under the umbrella of “ease-of-use”.

The first, and probably most important, reason to use a material point simulator instead of a full-featured finite-element code to system test constitutive models is that you can be absolutely certain of the inputs and outputs of the model being tested. When the model is being used, it can be difficult to determine exactly what the driving input is; for example, is it being driven by deformation rate or strain rate? Is the strain rate logarithmic strain rate or some other strain measure? How is the host code handling rotations? Is the model responsible for incorporating co-rotational rates in the returned stress? What is the correct ordering for the stresses? Should the off-diagonal components be multiplied by a scalar?

A related concept to the input-output issue is the necessity of choosing a proper element type. Different elements have different properties and modes of deformation and these differences can affect what would otherwise be a single element simulation. For example, a tetrahedral element is known to be artificially stiffer than a similar hexahedral element[27].

Another issue with full-featured host codes is the possible existence of hourglass stiffness, artificial viscosity, volumetric locking, mass-scaling, inertial effects, and enforcing boundary conditions. The effects from these, and similar, corrections can be negligible for certain loading scenarios and the effects can be dramatic in others. The boundary between negligible and dominant can be fuzzy and can cause some users difficulty when trying to verify their model in the host code. Then, there are also issues of how boundary conditions are applied and what are the solver tolerances when enforcing those boundary conditions.

The Abaqus User Subroutines Reference Guide[26] states at the very top of the section “UMAT” for User Subroutines:

Warning: The use of this subroutine generally requires considerable expertise. You are cautioned that the implementation of any realistic constitutive model requires extensive development and testing. Initial testing on a single-element model with prescribed traction loading is strongly recommended.

However, it is still common practice for professors and managers to task fresh graduate students or junior engineers to develop and implement new, complex material models. Often, these people have no formal training in software development and absolutely no experience with testing code, be it unit testing, integration testing, or system testing.

The use of a material point simulator makes testing easier to run by only running what is necessary. There are several open-source material point simulators available such as the Material Model Laboratory (previously Payette)[30] or CONSTLAB[19]. The literature mentions others, such as MMD (the material model driver)[29], EVER-CD[24], or a Material model driver for DYNA3D[37]. One benefit of using an open source material point simulator is that there are no licensing fees or licensing servers required to simply exercise or test a material model. This allow testing to happen on any machine, from a Raspberry Pi to a cluster, and the whole testing suite can be completed in a matter of seconds. This allows for constant

integration testing, where bugs can be caught as soon as they enter the code base and tests can be run frequently during development. When testing requires the use of the full simulation package, testing can be laborious and take a long time with the consequences that it is done less frequently, catches fewer bugs, and decreases productivity.

1.5 Equations for a Material Point Simulator

For those wishing to implement a material point simulator, the following equations can aid them in converting between different deformation measures and the inputs required for the model being used. The expected use-case is for the material point simulator to be given a table of inputs (deformation gradients, strains, stretches, *etc.*) and to drive the simulation using those inputs. From the table of inputs, both the current value of the input and its rate can be inferred by interpolating between values (for deformations) or by integrating rates (for deformation rates).

In several instances in the following relations, the rate of a matrix function is used. It is presented here in general form, and referenced later. Given a real, symmetric matrix \mathbf{A} , its rate $\dot{\mathbf{A}}$, and the matrix function $\mathbf{B} = f(\mathbf{A})$, it is possible to find the rate $d\mathbf{B}/dt$ using the following relation. As it is always possible to perform a spectral decomposition of any real, symmetric matrix into the eigenvalues λ_i and eigenprojections \mathbf{P}_i such that $\mathbf{A} = \sum_{i=1}^3 \lambda_i \mathbf{P}_i$, the spectral decomposition is computed and then, using the following relation from [12], the rate can be found

$$\dot{\mathbf{B}} = \sum_{i=1}^3 \sum_{j=1}^3 \gamma_{ij} \mathbf{P}_i \cdot \dot{\mathbf{A}} \cdot \mathbf{P}_j \quad (1.16)$$

where

$$\gamma_{ij} = \begin{cases} \frac{f(\lambda_i) - f(\lambda_j)}{\lambda_i - \lambda_j} & \text{if } \lambda_i \neq \lambda_j \\ f'(\lambda_i) & \text{if } \lambda_i = \lambda_j \end{cases} \quad (1.17)$$

1.5.1 Prescribed Deformation Gradient Simulations

The polar decomposition of the deformation gradient can be found using the Higham iterative method[41] to find the tensor \mathbf{R} with orthonormal rows/columns and the positive semi-definite tensor \mathbf{U} such that

$$\mathbf{F} = \mathbf{R} \cdot \mathbf{U} \quad (1.18)$$

If the simulation is to be driven by the strain, it can be found using the Seth-Hill formula for strains[67]

$$\epsilon = \frac{1}{k} \left(\mathbf{U}^k - \mathbf{I} \right) \quad (1.19)$$

or, for when $k \rightarrow 0$,

$$\epsilon = \ln(\mathbf{U}). \quad (1.20)$$

This formula for defining strain is very flexible and allows for many different definitions of strain depending on the value of k . As a 1D example, four common strain measures are represented with $k = -1, 0, 1, 2$, with $k = 0$ being the limit as $k \rightarrow 0$. In one dimension, let L_0 be the initial length, L be the current length, and λ be the ratio of L/L_0 . Then it is possible to define the Lagrange strain ($k = 2$)

$$\epsilon^{\text{lag}} = \frac{1}{2}(\lambda^2 - 1), \quad (1.21)$$

engineering strain ($k = 1$)

$$\epsilon^{\text{eng}} = \lambda - 1, \quad (1.22)$$

logarithmic strain ($k \rightarrow 0$)

$$\epsilon^{\text{log}} = \ln(\lambda), \quad (1.23)$$

and “true” strain ($k = -1$)

$$\epsilon^{\text{true}} = 1 - \frac{1}{\lambda}. \quad (1.24)$$

The deformation rate is found using the standard equation by first finding the velocity gradient

$$\mathbf{L} = \dot{\mathbf{F}} \cdot \mathbf{F}^{-1} \quad (1.25)$$

and finding the deformation rate by taking the symmetric part of \mathbf{L}

$$\mathbf{D} = \frac{1}{2} (\mathbf{L} + \mathbf{L}^T) \quad (1.26)$$

Calculating the right stretch rate $\dot{\mathbf{U}}$ from the deformation gradient \mathbf{F} and its rate $\dot{\mathbf{F}}$ is more complicated. Once the stretch rate is found, either through finite difference or analytically, the strains and strain rates can then be calculated. For the nonzero values of k , the

strain rate can be found using Equation 1.16 and with the following substitutions

$$\mathbf{A} = \mathbf{U} \quad \mathbf{B} = \epsilon \quad (1.27)$$

$$f(\lambda) = \frac{1}{k} (\lambda^k - 1) \quad f'(\lambda) = \lambda^k - 1. \quad (1.28)$$

This relation holds for all nonzero values of k . When $k = 1$, the above relation still holds, but is not necessary to perform a spectral decomposition as the strain rate is

$$\dot{\epsilon} = \dot{\mathbf{U}}. \quad (1.29)$$

The rate of the logarithmic strain (when $k \rightarrow 0$) also requires the rate of a matrix function, just as in Equation 1.27, but redefines

$$f(\lambda) = \ln(\lambda) \quad f'(\lambda) = \frac{1}{\lambda}. \quad (1.30)$$

1.5.2 Prescribed Strain Simulations

When using prescribed strain, the equations are similar to those given in Section 1.5.1, but inverted. When given a strain or strain rate it is only necessary to find the stretch and stretch rate. From those, it is possible to use Equations 1.19, 1.20, 1.27 and 1.30 to find the right stretch and its rate in order to find the deformation rate using Equation 1.26.

For nonzero values of k , the following relation can be used to find \mathbf{U}

$$\mathbf{U} = (k\epsilon + \mathbf{I})^{1/k}, \quad (1.31)$$

and for $k \rightarrow 0$

$$\mathbf{U} = \exp(\epsilon). \quad (1.32)$$

Equation 1.31 does not require an eigendecomposition when $k = 1$ or when ϵ is diagonal. Likewise, Equation 1.32 requires an eigendecomposition to perform the matrix exponent, except when ϵ is diagonal.

The general formula for the right stretch rate is similar to Equation 1.27 and also makes use of Equation 1.16 but makes the following substitutions

$$\mathbf{A} = \epsilon \quad \mathbf{B} = \mathbf{U} \quad f(\lambda) = (k\lambda + 1)^{1/k} \quad f'(\lambda) = (k\lambda + 1)^{1/k-1} \quad (1.33)$$

which can directly be used as the deformation gradient with no superimposed rotation, or can be used to compute the deformation rate

from Equation 1.26. Exactly like Equation 1.29, when $k = 1$ the relation simplifies to

$$\dot{\mathbf{U}} = \dot{\epsilon}. \quad (1.34)$$

When $k \rightarrow 0$, the same relations hold as in 1.33 but with the following substitutions

$$f(\lambda) = f'(\lambda) = e^\lambda. \quad (1.35)$$

1.6 Logarithmic Strain Rate vs. Deformation Rate (Unit and System Tests)

A common source of error in material model verification is the mismatch between the analytical solution and the simulated response when the model is first used in a full-featured code. One possible reason for the difference is that the codes usually furnish the model with the symmetric part of the velocity gradient \mathbf{D} (the deformation rate) instead of the rate of the logarithmic strain ϵ . For simple loading configurations along principal strain directions, \mathbf{D} is exactly ϵ , but the differences can even be observed under constant strain rate loading for very complex loadings.

To assist the material modeler in developing a material point simulator, here is presented a unit test that could be used for a function the converts between different deformation measures. To demonstrate the difference, a constant strain rate for uniaxial strain is assumed

$$\epsilon^{\text{uni}} = \begin{bmatrix} at & 0 & 0 \\ 0 & 0 & 0 \\ 0 & 0 & 0 \end{bmatrix} \quad (1.36)$$

and is transformed under a time-varying rotation around the \mathbf{e}_3 axis (such that at time $t = 1$ and $t = 2$ there is a rotation of 90° and 180° , respectively). The rotation tensor is

$$\mathbf{R} = \begin{bmatrix} \cos(\frac{\pi t}{2}) & -\sin(\frac{\pi t}{2}) & 0 \\ \sin(\frac{\pi t}{2}) & \cos(\frac{\pi t}{2}) & 0 \\ 0 & 0 & 1 \end{bmatrix} \quad (1.37)$$

which gives a final form for the time-varying strain and strain rate

$$\epsilon = \mathbf{R} \cdot \epsilon^{\text{uni}} \cdot \mathbf{R}^T \quad (1.38)$$

$$\dot{\epsilon} = \dot{\mathbf{R}} \cdot \epsilon^{\text{uni}} \cdot \mathbf{R}^T + \mathbf{R} \cdot \dot{\epsilon}^{\text{uni}} \cdot \mathbf{R}^T + \mathbf{R} \cdot \epsilon^{\text{uni}} \cdot \dot{\mathbf{R}}^T, \quad (1.39)$$

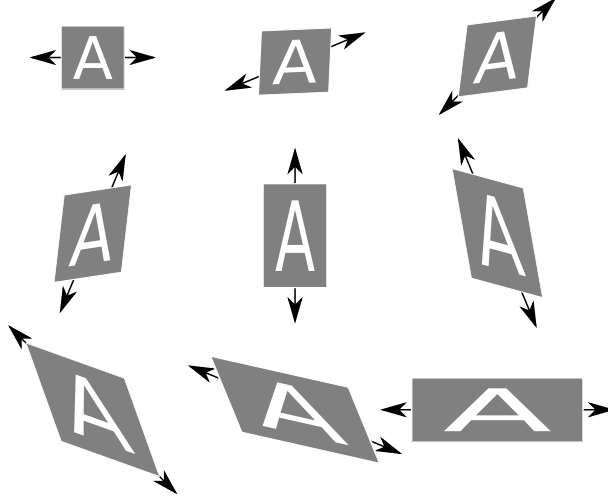


Figure 1.1: A graphical representation of a rotating constant uniaxial strain rate operating on glyphs (discussed in Section 1.6). Note, the loading direction is undergoing rotation, not the glyph itself. The initial condition is in the top-left corner and is read left-to-right, top-to-bottom and in time increments of $\Delta t = 0.25$.

or, explicitly, the nonzero components of the strain tensor are

$$\begin{aligned}
 \epsilon_{xx} &= at \cos^2\left(\frac{\pi t}{2}\right) \\
 \epsilon_{yy} &= at \sin^2\left(\frac{\pi t}{2}\right). \\
 \epsilon_{xy} &= \frac{1}{2}at \sin(\pi t)
 \end{aligned}
 \tag{1.40}$$

Figure 1.1 contains a graphical depiction of this deformation affecting a glyph. While the base uniaxial strain is subjected to a rotation, the actual deformation does not rotate the material as it is driven by logarithmic strain which contains no material rotation information.

To compare the rate of the logarithmic strain and the symmetric part of the velocity gradient, it is first necessary to convert the strain tensor ϵ to the deformation gradient \mathbf{F} , right stretch tensor \mathbf{U} , or the left stretch tensor \mathbf{V} , which are all equivalent as there is no rotation, through the following relation, which uses the matrix exponential,

$$\mathbf{F} = \mathbf{U} = \exp(\epsilon).
 \tag{1.41}$$

Once the right stretch is found the velocity gradient \mathbf{L} can be found

using the rate and transpose of \mathbf{U}

$$\mathbf{L} = \dot{\mathbf{U}} \cdot \mathbf{U}^{-1}. \quad (1.42)$$

The symmetric part of the velocity gradient is then found by

$$\mathbf{D} = \frac{1}{2} (\mathbf{L} + \mathbf{L}^T). \quad (1.43)$$

The final forms of the nonzero components of the strain rate, stretch rate, and symmetric part of the velocity gradient are

$$\begin{aligned} \dot{\epsilon}_{xx} &= \frac{a}{2}(1 + \cos(\pi t) - \pi t \sin(\pi t)) \\ \dot{\epsilon}_{yy} &= \frac{a}{2}(1 - \cos(\pi t) + \pi t \sin(\pi t)), \\ \dot{\epsilon}_{xy} &= \frac{a}{2}(\pi t \cos(\pi t) + \sin(\pi t)) \end{aligned} \quad (1.44)$$

$$\begin{aligned} \dot{U}_{xx} &= \frac{1}{2}(\pi \sin(\pi t) + e^{at}(a + a \cos(\pi t) - \pi \sin(\pi t))) \\ \dot{U}_{yy} &= \frac{1}{2}(e^{at}(a - a \cos(\pi t) + \pi \sin(\pi t)) - \pi \sin(\pi t)), \\ \dot{U}_{xy} &= \frac{1}{2}((e^{at} - 1)\pi \cos(\pi t) + ae^{at} \sin(\pi t)) \end{aligned} \quad (1.45)$$

$$\begin{aligned} D_{xx} &= \frac{1}{2}(a + a \cos(\pi t) - \pi \sin(\pi t) \sinh(at)) \\ D_{yy} &= \frac{1}{2}(a - a \cos(\pi t) + \pi \sin(\pi t) \sinh(at)). \\ D_{xy} &= \frac{1}{2}(a \sin(\pi t) + \pi \cos(\pi t) \sinh(at)) \end{aligned} \quad (1.46)$$

A comparison of ϵ and $\int \mathbf{D}$ as well as $\dot{\epsilon}$ and \mathbf{D} is shown in Figure 1.2.

1.6.1 Driving Strain for Other Values of k

The example presented in Section 1.6 demonstrates the difference between logarithmic strain rate and the rate of deformation, but also can be used as a unit test or system test of a material point simulator. To further the usefulness of that example, here is presented the equations for the driving strains defined by a non-zero Seth-Hill parameter k , but which describe the same deformation. The non-zero components of the strain tensor are

$$\begin{aligned} \epsilon_{xx} &= \frac{1}{k}(e^{kat} - 1) \cos^2\left(\frac{\pi t}{2}\right) \\ \epsilon_{yy} &= \frac{1}{k}(e^{kat} - 1) \sin^2\left(\frac{\pi t}{2}\right). \\ \epsilon_{xy} &= \frac{1}{2k}(e^{kat} - 1) \sin\left(\frac{\pi t}{2}\right) \end{aligned} \quad (1.47)$$

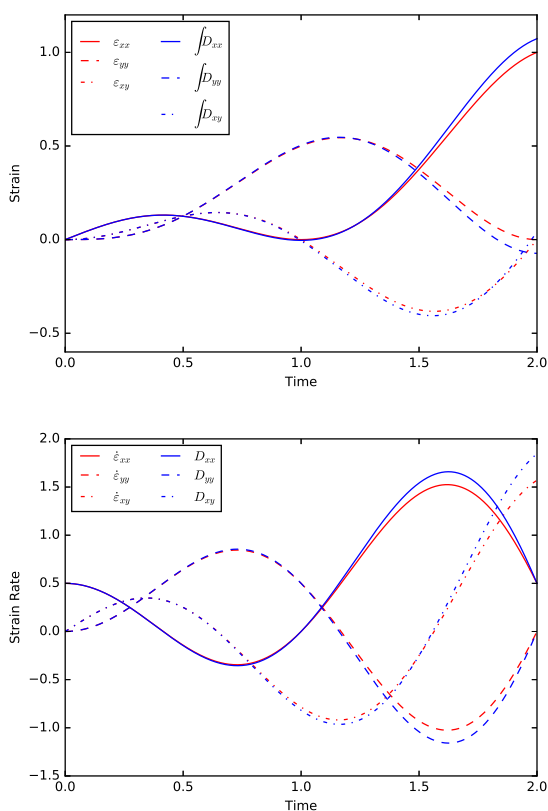


Figure 1.2: A comparison of the deformation and deformation rate of the strain and symmetric part of the velocity gradient. The analytical solution is derived in Section 1.6 and a graphical representation is shown in Figure 1.1. The parameter $a = 1/2$ such that at time $t = 2$ the logarithmic axial strain is 1.

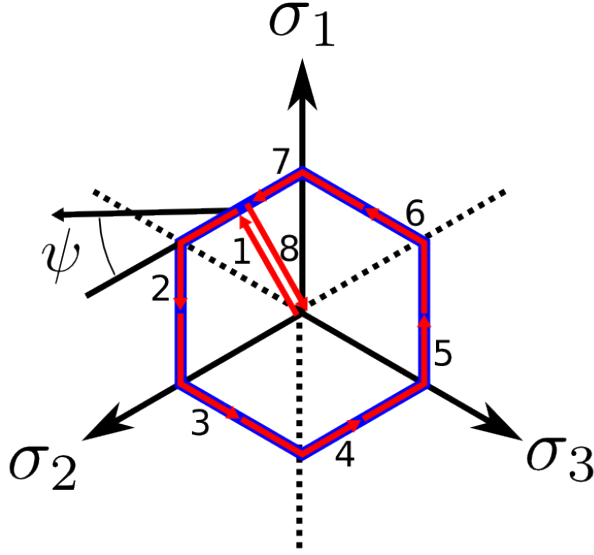


Figure 1.3: A representation in the deviatoric plane of the verification test in Section 1.7. The blue line represents the yield surface and the red arrows represent the loading legs of the test. The initial and final states are coincident at the origin.

The non-zero components of the strain rate tensor are

$$\begin{aligned}
 \dot{\epsilon}_{xx} &= \frac{\pi \sin(\pi t) + e^{kat}(ak + ak \cos(\pi t)) - \pi \sin(\pi t)}{2k} \\
 \dot{\epsilon}_{yy} &= \frac{e^{kat}(ak - ak \cos(\pi t) + \pi \sin(\pi t)) - \pi \sin(\pi t)}{2k}. \\
 \dot{\epsilon}_{xy} &= \frac{(e^{kat} - 1)\pi \cos(\pi t) + ake^{kat} \sin(\pi t)}{2k}
 \end{aligned} \tag{1.48}$$

1.7 Tresca Verification test

This section presents a system test for the plasticity model presented in Section 1.2. It is meant to exercise each part of the model: the elastic phase, the plastic phase (with both planes and vertices of the yield surface), as well as be a check against false elastic domains.

For this verification test we require the following values to be set

$$\begin{aligned}
 G &\in (0, \infty) && \text{Shear modulus} \\
 Y_s &\in (0, \infty) && \text{Yield in shear} \\
 \psi &\in [0^\circ, 30^\circ) && \text{Angle for plastic steps}
 \end{aligned} \tag{1.49}$$

This benchmark is entirely deviatoric and, therefore, the value of the bulk modulus is arbitrary. The test is composed of eight legs: 1) Load in pure shear to the yield surface, 2-7) Plastically load so that each leg moves the stress state from one point of pure shear on the yield surface to an adjacent point of pure shear on the yield surface, 8) Unload back to zero stress along the same trajectory as leg 1. While this verification test is written in terms of principal stresses and strains, the input strains can be arbitrarily rotated and the output stresses will be rotated by that same arbitrary rotation.

This test will make heavy use of rotation tensors defined by a unit axis of rotation \mathbf{a} and an angle of rotation α .

$$\mathbf{R}_\alpha = \cos \alpha \mathbf{I} + (1 - \cos \alpha) \mathbf{a}\mathbf{a} + \sin \alpha \begin{bmatrix} 0 & -a_3 & a_2 \\ a_3 & 0 & -a_1 \\ -a_2 & a_1 & 0 \end{bmatrix} \tag{1.50}$$

which, for a rotation of ϕ -degrees about the hydrostatic axis, simplifies to

$$\mathbf{R}_\phi = \frac{1}{3} \begin{bmatrix} 1 + 2 \cos \phi & 1 - \cos \phi - \sqrt{3} \sin \phi & 1 - \cos \phi + \sqrt{3} \sin \phi \\ 1 - \cos \phi + \sqrt{3} \sin \phi & 1 + 2 \cos \phi & 1 - \cos \phi - \sqrt{3} \sin \phi \\ 1 - \cos \phi - \sqrt{3} \sin \phi & 1 - \cos \phi + \sqrt{3} \sin \phi & 1 + 2 \cos \phi \end{bmatrix}. \tag{1.51}$$

The strain increment for the first leg is computed in the following manner. First, arbitrarily choose a unit tensor \mathbf{p} that represents pure shear, here taken to be

$$\mathbf{p} = \frac{1}{\sqrt{2}} \begin{bmatrix} 1 & 0 & 0 \\ 0 & 0 & 0 \\ 0 & 0 & 01 \end{bmatrix}, \tag{1.52}$$

and calculate the magnitude of strain required to achieve incipient yield. The stress and strain values for leg 0 and leg 1 are

$$\text{Initial Conditions} \quad \epsilon|_{t=0} = \epsilon_0 = \mathbf{0} \quad \sigma|_{t=0} = \sigma_0 = \mathbf{0} \tag{1.53}$$

$$\text{Leg 1} \quad \Delta \epsilon_1 = \frac{Y_s}{\sqrt{2}G} \mathbf{p} \quad \epsilon|_{t=1} = \epsilon_0 + \Delta \epsilon_1 \quad \sigma|_{t=1} = \sqrt{2} Y_s \mathbf{p}. \tag{1.54}$$

Legs 2-7 deal with plasticity and will traverse the limits of the yield surface. Our unit tensor \mathbf{p} from step 1 will now be rotated by $90^\circ - \psi$ degrees to create the new unit tensor $\mathbf{q} = \mathbf{R}_{(90^\circ - \psi)} \cdot \mathbf{p} \cdot \mathbf{R}_{(90^\circ - \psi)}^T$. Legs 2-7 all depend on

$$m_1 = \sqrt{\frac{2}{3}} \frac{Y_s}{\cos(\psi)} \quad m_2 = \sqrt{\frac{2}{3}} \frac{Y_s}{\cos(\psi + 60^\circ)} \quad \eta = \frac{m_1}{m_1 + m_2} \quad (1.55)$$

where η is the fraction of the leg that is on the same face of the Tresca yield surface as at the beginning of the leg or, equivalently, it is the point in the leg where the stress state arrives at the vertex.

All the state information for legs 2-7 can be found by the same set of equations (for $k = 1..6$):

Leg $k - 1$:

$$\begin{aligned} \Delta\epsilon_{k+1} &= \frac{m_1 + m_2}{2G} \mathbf{R}_{(k-1)60^\circ} \cdot \mathbf{q} \cdot \mathbf{R}_{(k-1)60^\circ}^T \\ \epsilon|_{t=k+\eta} &= \epsilon_0 + \sum_{i=1}^k \Delta\epsilon_i + \eta * \Delta\epsilon_{k+1} \\ \sigma|_{t=k+\eta} &= \sqrt{\frac{2}{3}} 2Y_s \mathbf{R}_{(k-1)60^\circ} \cdot \mathbf{R}_{30^\circ} \cdot \mathbf{p} \cdot \mathbf{R}_{30^\circ}^T \cdot \mathbf{R}_{(k-1)60^\circ}^T \\ \epsilon|_{t=k+1} &= \epsilon_0 + \sum_{i=1}^{k+1} \Delta\epsilon_i \\ \sigma|_{t=k+1} &= \sqrt{2} Y_s \mathbf{R}_{k60^\circ} \cdot \mathbf{p} \cdot \mathbf{R}_{k60^\circ}^T. \end{aligned} \quad (1.56)$$

Finally, leg 8 simply returning elastically to the origin along the same trajectory as leg 1

Leg 8 :

$$\begin{aligned} \Delta\epsilon_8 &= -\frac{Y_s}{\sqrt{2}G} \mathbf{p} \\ \epsilon|_{t=8} &= \epsilon_0 + \sum_{i=1}^8 \Delta\epsilon_i = \mathbf{0} \\ \sigma|_{t=8} &= \mathbf{0} \end{aligned} \quad (1.57)$$

This completes one full cycle of the verification test.

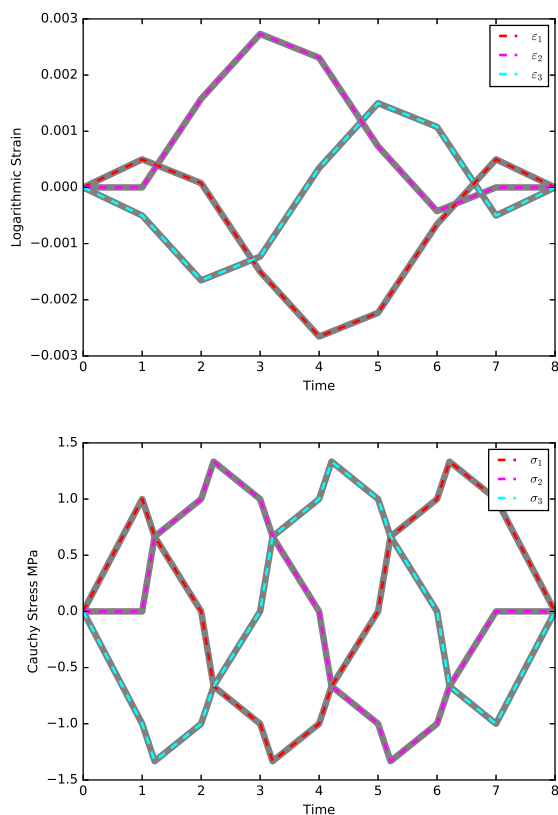


Figure 1.4: Plots showing the principal strains (top) and the principal stresses (bottom) of the Tresca verification test using $\psi = 15^\circ$, $Y_s = 1\text{MPa}$, and $G = 1\text{GPa}$. The thick, gray lines are the analytical solution and the dotted lines are the response predicted by a model written in Fortran driven by strain.

Time	ε_1	ε_2	ε_3	σ_1	σ_2	σ_3
0	0	0	0	0	0	0
1	$\frac{Y_s}{6G}3$	0	$-\frac{Y_s}{6G}3$	Y_s	0	$-Y_s$
1 + η	$-\frac{Y_s}{6G}(1 - 2\sqrt{3})$	$\frac{Y_s}{6G}2$	$-\frac{Y_s}{6G}(1 + 2\sqrt{3})$	$\frac{2Y_s}{3}$	$\frac{2Y_s}{3}$	$-\frac{4Y_s}{3}$
2	$-\frac{Y_s}{6G}(3 - 2\sqrt{3})$	$\frac{Y_s}{6G}(6 + 2\sqrt{3})$	$-\frac{Y_s}{6G}(3 + 4\sqrt{3})$	0	Y_s	$-Y_s$
2 + η	$-\frac{Y_s}{6G}(5 - 2\sqrt{3})$	$\frac{Y_s}{6G}(4 + 4\sqrt{3})$	$\frac{Y_s}{6G}(1 - 6\sqrt{3})$	$-\frac{Y_s}{\sqrt{3}}$	$\frac{2Y_s}{\sqrt{3}}$	$-\frac{Y_s}{\sqrt{3}}$
3	$-\frac{Y_s}{6G}9$	$\frac{Y_s}{6G}(6 + 6\sqrt{3})$	$\frac{Y_s}{6G}(3 - 6\sqrt{3})$	$-Y_s$	Y_s	0
3 + η	$-\frac{Y_s}{6G}(7 + 2\sqrt{3})$	$\frac{Y_s}{6G}(2 + 8\sqrt{3})$	$\frac{Y_s}{6G}(5 - 6\sqrt{3})$	$-\frac{2Y_s}{\sqrt{3}}$	$\frac{Y_s}{\sqrt{3}}$	$\frac{Y_s}{\sqrt{3}}$
4	$-\frac{Y_s}{6G}(9 + 4\sqrt{3})$	$\frac{Y_s}{6G}8\sqrt{3}$	$\frac{Y_s}{6G}(9 - 4\sqrt{3})$	$-Y_s$	0	Y_s
4 + η	$-\frac{Y_s}{6G}(5 + 6\sqrt{3})$	$-\frac{Y_s}{6G}(2 - 8\sqrt{3})$	$\frac{Y_s}{6G}(7 - 2\sqrt{3})$	$-\frac{Y_s}{\sqrt{3}}$	$-\frac{Y_s}{\sqrt{3}}$	$\frac{2Y_s}{\sqrt{3}}$
5	$-\frac{Y_s}{6G}(3 + 6\sqrt{3})$	$-\frac{Y_s}{6G}(6 - 6\sqrt{3})$	$\frac{Y_s}{6G}9$	0	$-Y_s$	Y_s
5 + η	$-\frac{Y_s}{6G}(1 + 6\sqrt{3})$	$-\frac{Y_s}{6G}(4 - 4\sqrt{3})$	$\frac{Y_s}{6G}(5 + 2\sqrt{3})$	$\frac{Y_s}{\sqrt{3}}$	$-\frac{2Y_s}{\sqrt{3}}$	$\frac{Y_s}{\sqrt{3}}$
6	$\frac{Y_s}{6G}(3 - 4\sqrt{3})$	$-\frac{Y_s}{6G}(6 - 2\sqrt{3})$	$\frac{Y_s}{6G}(3 + 2\sqrt{3})$	Y_s	$-Y_s$	0
6 + η	$\frac{Y_s}{6G}(1 - 2\sqrt{3})$	$-\frac{Y_s}{6G}2$	$\frac{Y_s}{6G}(1 + 2\sqrt{3})$	$\frac{2Y_s}{\sqrt{3}}$	$-\frac{Y_s}{\sqrt{3}}$	$-\frac{Y_s}{\sqrt{3}}$
7	$\frac{Y_s}{6G}3$	0	$-\frac{Y_s}{6G}3$	Y_s	0	$-Y_s$
8	0	0	0	0	0	0

Table 1.1: Table of piecewise-linear principal strains and stresses for the Tresca verification benchmark. The time-fraction at which the vertex is reached in each plastic step is $\eta = (3 - \sqrt{3})/6$, the yield in shear is Y_s , and the shear modulus is G . As the state at the end of step 1 and step 7 are equivalent, it is possible to traverse the yield surface multiple times by repeating steps 2-7. Note that the strains at vertices ($i + \eta$) are for reference as the strain rate is constant though each step (from i to $i + 1$).

1.8 Conclusion

The current state of material modeling lacks the formal training and best practices of software developers. The software development model known as Test-Driven Development is proposed as a method for decreasing fault density in constitutive models and increasing productivity and code quality. Constitutive modeling is a discipline that could easily embrace TDD as it focuses on verifying code based on analytic solutions. The benefits of TDD are: increased code stability, lower fault density, better documentation, and faster code development.

Constitutive modelers can also benefit from the use of a material point simulator to exercise the material models separately from a full-featured simulation package. The benefits of using material point simulators are: transparency for inputs and outputs, more simple boundary conditions, no need to choose an element type, execution speed (minimal overhead), and no inertial effects, hourglass stiffness, or artificial viscosity. Also, open-source material point simulators are freely available that have features such as stress-control and parameter optimization.

Finally, testing code at every level (unit, integration, system, and regression testing) is absolutely crucial to having confidence in the code and to ensure the model solves the equations correctly. Several examples of each type of test are presented for a sample Tresca plasticity model, as well as analytical solutions for deformation description conversions for use in material point simulators.

Application of Tomographic Reconstruction Techniques for Density Analysis of Green Bodies

Progress in the manufacturing of ceramics, but also of sintered metals, strongly relies on the evaluation of the density distribution in green bodies. This evaluation is crucial from many points of view, including the calibration of constitutive models for in-silico simulation of densification processes. To this end, X-ray tomography and other techniques are possible but can be unmanageable for some institutions. Therefore, a destructive method is introduced in the present chapter to measure the density field of a green body sample using a CNC mill, an analytical balance, and analysis techniques from the field of computational tomography. A virtual experiment is presented where the method is used to reconstruct a simulated green body density field and is found to satisfactorily correspond to the original solution. The green body density field of a truncated cylinder made of alumina powder is evaluated using this method and the reconstructed field is presented.

2.1 Introduction

The ceramics industry is interested in increasing efficiency, reducing waste, and, therefore, reducing costs. During the production process the extent of heterogeneity in the green body directly influences the final geometry, strength, and hardness after sintering[13]. Not only do these variations usually decrease product performance, they also amplify uncertainty in material behavior which is unacceptable when producing high-performance ceramics. Currently, the ceramics industry heavily relies on the process of trial-and-error to determine optimal mold geometry and forming pressures for a given piece[18].

High-performance ceramics are used in many sectors and are subjected to many different types of environments. Some usage examples

include: refractory products subject to extreme temperatures, piezoelectrics subject to extreme loading or electric fields, or ceramic plates subject to shock loading. Each of these use-cases requires predictable performance which is often limited by the uncertainty in macroscopic mechanical behavior of the piece.

Density inhomogeneities in green bodies are associated with stress variations which are usually caused by defects in the production process. However, when final residual stress fields can be predicted and utilized in the design process, these residual stresses can be used to pre-stress the sample to make it more resilient for the intended use-case.

Because so much of the final performance of the ceramic piece is dependent on the density of the green body, many different techniques have been developed to measure internal density. The most simple method for measuring bulk density accurately is to use Archimedes' principle with mercury displacement instead of water. More technical methods put inclusions in the powder before compaction in a known configuration, position, or concentration and infer the final density from the final positions of the inclusions. Some inclusions that have been used are: layers of colored powder[13], layers of film, or a thin lattice made of lead[45]. A more recent method for density measurement has been measure X-ray attenuation to measure the average bulk density along the path of an X-ray[2]. The main benefits of this last method are that it is non-destructive, rapid, and can be used on green bodies as well as sintered pieces.

However, the most commonly used density measurement technique in use in the literature today is to utilize surface hardness measures, either from indentation or from scratching, and convert them to density measures using a table that correlates hardness to density[28, 61, 15]. The two primary drawbacks to this method are that the table correlating density to hardness must be produced (either by experimentation or making material assumptions) and that the sample must have sufficient cohesion to be worked, scratched, or indented without failure. The latter drawback is usually overcome by partially sintering the green body before analysis.

Finally, it is worth mentioning that even the method of X-ray absorption requires a correlation table and calibration to set the relationship between the gray level of the X-ray images and the bulk density[2].

The density evaluation method introduced in the present chapter is intended to overcome the hurdles of high cost, adding inclusions to the sample, steep learning curves to perform or analyze the mea-

surement, and the need for previously-developed calibration tables. By decreasing the requirements to make these measurements, small laboratories or universities with limited equipment and budgets can perform 3D density measurements. As it makes use of simple computer numerical control (CNC) mills and an analytical balance, the accuracy of the analysis is directly related to the accuracy of the equipment and, to a greater extent, the number of data points taken for the measurement.

2.2 Presentation of the Method

The present method for density distribution evaluation is defined in the following steps: (i) a CNC mill is used to incrementally remove mass from a green body in parallel strips and an analytical balance is used to weigh the sample before and after each strip to obtain the corresponding lost mass; (ii) a collection of strips for a given transverse section are combined to make a single projection; (iii) steps (i) and (ii) are repeated in a different direction at least one additional time (see note below); (iv) these projections and the known geometry (defined by the path, milling bit used, and depth of the CNC mill) of the piece can be used in a tomographic reconstruction routine; (v) repeat steps (i) through (iv) for each transverse slice in the sample to create a 3D reconstruction.

Because the present technique requires at least two projections to reconstruct the density field and the projection method is a destructive method, it is advisable to either produce multiple samples (one per projection) or utilize symmetry of the body to get multiple projections from a single sample. Multiple projections from the same sample can be accomplished by milling for one projection on one symmetry section and changing directions for the other symmetry sections.

The basic concept for machining ceramics while in the green body state is discussed by Su *et al.*[69], but here it is applied to density evaluation, not shaping, finishing, or rapid prototyping. For a green body of compressed alumina powder, a CNC mill proved to be able to easily mill the body with sufficient precision. However, because the green body has not been sintered, the faces of the sample that have been milled are not smooth as powder grains become dislodged as the mill bit passes by. This was found to be invariant of the milling speed or the rotational velocity of the bit. The milled mass needs to be removed after milling each strip along, which can be accomplished



Figure 2.1: Texture of a 10g alumina green body formed by 120MPa mean axial stress in the shape of a truncated cylinder with 30mm diameter and 10° incline in the process of being milled. The left portion of the sample is the smooth, inclined surface that was created by the mold during pressing. The other surfaces are created by the milling process and demonstrate the rough but uniform texture produced by the CNC mill in the cutting process. The vertical difference between successive layers is 1mm (e.g. the step between the surfaces in the top-right and bottom-right of the image).

with a vacuum or compressed air to either suck up or blow away the filings. For all but the smallest sections, the magnitude of this effect was not excessive and did not invalidate the measurements. A sample of pressed alumina powder that is in the process of being milled is presented in Figure 2.1.

2.3 Tomographic Reconstruction

The mathematical basis of Tomography was laid by Johann Radon in 1917 with his seminal paper that proved that a 2D density function can be exactly reproduced from an infinite number of 1D projections[60]. In that paper, he describes what later became known as the Radon transform (the projection step), the output of which is a sinogram, and the inverse Radon transform (the reconstruction step). These

processes are still the basis for most reconstruction techniques.

The birth of modern computer tomography occurred around 1970 when computers with sufficient memory and processing power became available to researchers. One of the first iterative computational algorithms for reconstructing data from projections was published by Gordon, Bender, and Herman[35]. Their paper introduces an iterative method for solving a system of ill-constrained equations to produce a useful image that approximates the original structure. While there are currently many different algorithms in use, some more recent reconstruction methods have been reported to be able to reproduce internal structures exactly from highly incomplete frequency information[17].

2.3.1 Theoretical basis of tomography

The inverse Radon transform is simply solving a (typically non-linear and ill-constrained) system of equations that are derived from a set of projections. Each equation in the system represents an element of a single projection (see Figure 2.2). The formulation is written with a 2D density field $f(x, y) \in [0, \infty)$, a projection angle $\theta \in [0^\circ, 180^\circ)$, and a projection element P_j associated with a projection strip g_j such that

$$P_j = \int_{g_j} f(x, y) dy dx, \quad (2.1)$$

where $j = 1, \dots, m$. The projection P is the set of projection elements for one projection direction θ . For a complete reconstruction, many projections with different projection directions $\theta_1, \theta_2 \dots \theta_m$ are required.

In current X-ray tomography, hundreds of projections can be taken for a single reconstruction. These projections are usually compiled into a sinogram that can succinctly convey complete projection information in all directions in one plot (see Figure 2.3), but is not generally human-readable. The sinogram is constructed by representing each projection as a column of an image in a sequential manner according to the projection angle. However, when full projection data are not available, the sinogram is only defined for specific angle values. There are two methods to handle incomplete projection data: attempt to interpolate the sinogram[48] or perform the reconstruction using only the measured projections[34]. This work follows the latter method as most research involving interpolating sinogram data does not attempt to interpolate over breaks larger than 30 degrees.

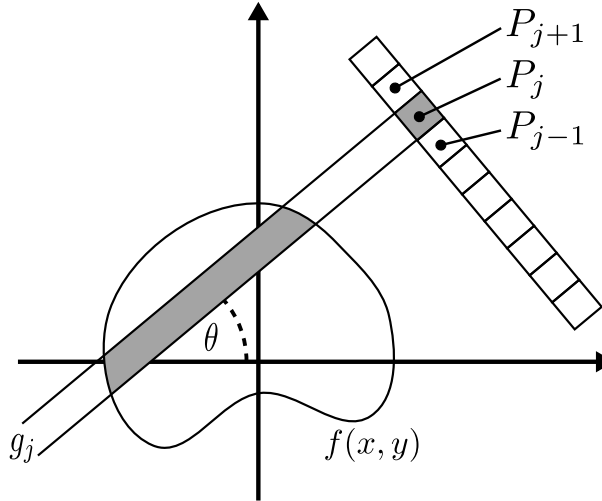


Figure 2.2: A body with a continuously-varying density field $f(x, y)$ is projected in the direction θ and is gathered into m bins denoted P_j of the projection P . Multiple projections along different values of θ are used to reconstruct the density field $f(x, y)$.

Three of the most common types of reconstruction methods are filtered back projection, algebraic reconstruction technique (ART), and 2D Fourier reconstruction[16].

2.3.2 Algebraic Reconstruction Technique

The algebraic reconstruction technique (ART), which is the reconstruction technique used in this work, is one of the first iterative reconstruction methods that was developed in 1974 by Gordon and Herman[34].

This method updates the i th reconstructed discretized field value at the q th iteration f_i^q by enforcing the reconstruction projection element P_j^q to agree exactly with the measured projection element P_j . This is accomplished by evaluating the difference between the measured projection element's value and the value of the current iteration and calculating a correction factor. If the correction factor is applied additively the method is called the additive ART or, if applied multiplicatively, it is called multiplicative ART. The additive and multiplicative ART iterative formulas are, respectively,

$$f_i^{q+1} = f_i^q + \frac{P_j - P_j^q}{N_j} f_i^q \quad \forall f_i \in g_j, \quad (2.2)$$

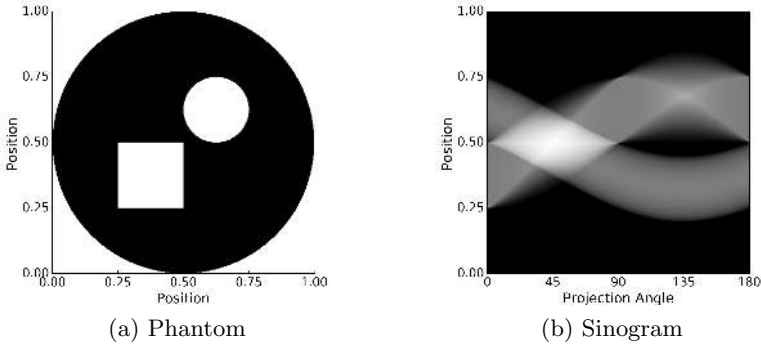


Figure 2.3: An example of a phantom/sinogram pair. The sinogram was produced using the open-source `scikit-image` Python library. The analysis domain consists of the inscribed black circle with the white circle and square inclusions. The analysis domain is circular such that the cross-section width is uniform for all projection angles. Notice that, as the projection direction changes in the sinogram, the circle's projection is constant while the square's projection has two intertwining density peaks (from the corners of the square) that both have a period of 180° .

and

$$f_i^{q+1} = \left(\frac{P_j}{P_j^q} \right) f_i^q \quad \forall f_i \in g_j, \quad (2.3)$$

with

$$f_i^0 = \hat{f} = \frac{\sum_j P_j}{n} \quad \forall f_i, \quad (2.4)$$

where N_j is the number of discretized field elements in the projection strip g_j and n is the total number of discrete values comprising the reconstructed field. Because the total slice mass is independent of the projection direction, it does not matter which projection is used for initializing the reconstruction field. Equations (2.2) or (2.3) are applied iteratively for each element in each projection until an equilibrium condition is met. A mixed version of the technique where additive ART is used during one iteration and multiplicative ART is used in the next is also sometimes used to help convergence. A more complicated, but also popular variation is called SART, for Simultaneous Algebraic Reconstruction Technique, where all the projection equations are simultaneously solved[3].

As there is always noise in data acquisition (both epistemic and aleatory uncertainty), it is not uncommon that all of the projection constraints are not able to be exactly met simultaneously. In an attempt to overcome this limitation, many different convergence criteria have been suggested over the years, including in Gordon's original publication. The three primary convergence criteria are based on the discrepancy D , entropy S , and variance V of the reconstruction. These are defined as

$$D = \sqrt{\frac{1}{m} \sum_{j=1}^m \frac{P_j - P_j^q}{N_j}}, \quad (2.5)$$

$$S = \frac{-1}{\ln n} \sum_{i=1}^n \left(\frac{f_i^q}{\bar{f}} \right) \ln \left(\frac{f_i^q}{\bar{f}} \right), \quad (2.6)$$

and

$$V = \sum_{i=1}^n (f_i^q - \bar{f})^2, \quad (2.7)$$

where \bar{f} is the arithmetic mean of the reconstructed field. As the iteration number increases, D approaches zero and both S and V tend to a minimum. If the discrepancy does not converge to zero, the reconstruction can be considered converged when the changes in S and/or V are sufficiently small. There are methods to alleviate some of the problems associated with non-convergence, for example, by interleaving iterations of additive and multiplicative ART or by applying relaxation factors to the correction factor for additive ART[44]. In this instance, the interleaved method was implemented to improve convergence.

The fidelity of the reconstruction can be enhanced by applying constraints to the reconstruction algorithm. An obvious constraint for reconstructing density fields is to require each element in the reconstructed field to be non-negative during every iteration or to only reconstruct the field over a specified domain. The latter can be accomplished simply by setting $f_i^0 = 0$ for all field elements outside of the reconstruction domain at each iteration.

2.3.3 Number of Projections

The real benefit of using tomographic techniques to reconstruct a density field inside a ceramic sample is that it increases the resolution of the field while decreasing the amount of labor otherwise required to

measure those values. Obviously, a researcher could cut the sample into an arbitrary number of sections and measure and weigh them to determine their density. However, for a square domain spanned by n elements in each direction, this would require n^2 measurements whereas reconstructing the field using p projections of n elements each, the total number of measurements is np . When less precise data is acceptable, the minimum $2n$ measurements can provide satisfactory aggregate information over the entire green body slice - much more efficient than the original n^2 measurements.

2.3.4 Strengths and weaknesses of 2-projection ART

Of course, the greater the number of projections the better the accuracy of the reconstructed field. One of the greatest drawbacks to only using 2 projections is the inability to detect field characteristics at an inclined angle with respect to the projection directions[62]. For this purpose, this method is best used when some *a priori* knowledge can be applied to the analysis such that the projection directions are in line with the natural orientation of the reconstructed field. This method has been found to be able to exactly reproduce unimodal density fields when principal axes are aligned with the projection directions (see Figure 2.5e). If *a priori* knowledge of the field is not available or the field has many local effects, additional projections should be incorporated to reconstruct the structure with greater accuracy. Once the additional projections have enabled the reconstruction to give more accurate results, such that the principal axes (if any) can be found, then successive density evaluations can be performed with fewer projections done in the optimal directions.

Another strength for 2-projection ART is the simplicity of the implementation. While commercial and open-source scientific libraries often have an inverse radon transform function, when doing a 2-projection reconstruction the implementation is simple. The simplification is due to the row-and-column nature of the reconstruction grid (pixels of the image) and that the projections operate along the rows and columns. This circumvents the necessity to partition projections when the reconstruction grid and the projection direction are not coincident. Some researchers have suggested using non-cartesian grids or basic reconstruction elements other than the industry-standard rectangular pixel or rectangular prismatic voxel[54].

All of the reconstruction methods (additive, multiplicative, and mixed) have been found to be dispersive. For a given density field, the reconstruction is always found to under-predict density variance

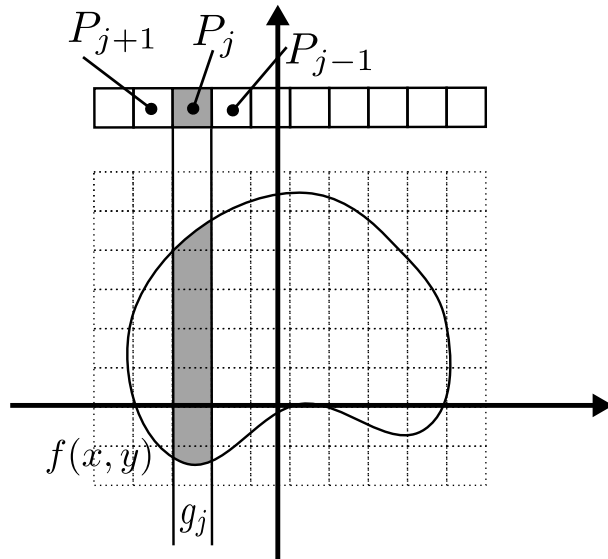


Figure 2.4: A demonstration of why a 2-projection reconstruction is conducive to reconstructing on a cartesian grid, such as a digital image. Compare with the arbitrary nature of Figure 2.2. When more than the two projections in the principal directions ($\theta = 0^\circ, 90^\circ$), it is then necessary to determine how to partition the projections into cells that span multiple columns or rows.

of the piece. However, there are instances where edge effects can cause the density to be much larger or much smaller than expected. These edge effects can be anything from corners of the reconstruction domain or when the reconstruction domain is in some other way constrained.

Figures 2.7 and 2.10 show examples of reconstructions when the domain is constrained to be entirely within the unit circle. Although the constraint is radially symmetric, it is still a uniform characteristic of the reconstruction methods for the density isosurfaces to form concentric diamonds in line with the principal axes of the image with the peak densities along the faces of the isosurface diamonds.

The additive ART is shown to have a particular propensity to creating diamond-like points in the density isosurfaces. A comparison of Figures 2.5c and 2.6c shows how the method introduces irregularities and verticies when reconstructing a field that is infinitely smooth.

It is interesting to compare Figures 2.5 and 2.8, Figures 2.6 and 2.9, and Figures 2.7 and 2.10. From these comparisons, the conclusion can be made that ART performs better on the traditional gaussian density function, rotated or unrotated, than it does with the “inverse” gaussian function. While this is true for these examples, it is important to acknowledge that the reconstruction techniques are invariant to positive or negative shifts in the entire field (e.g. if the function used in Figures 2.5, 2.6, or 2.7 were $f(x, y) = e^{2x^2 + 10y^2} + C$, the magnitude of the errors would be exactly the same).

2.4 Virtual Experiment

A virtual experiment is now presented with the purpose of examining the efficacy of the two-projection algebraic reconstruction technique. The examination is performed by comparing the reconstruction of a density field to a known solution produced by finite element software using a ceramic powder compaction model similar to that used by Stupkiewicz *et al.*[68]. In the simulated experiment, a ceramic powder is compacted in a circular mold with a flat punch and a 10° inclined base to form a green body in the shape of a truncated cylinder (such as the sample depicted in Figure 2.1). The simulation was performed using Abaqus Standard and a user material routine of the above-mentioned model with 425 reduced-integration 3D hexahedral elements for a full 3D simulation of the compaction process. A representative transverse slice of the simulated green body is used to generate two orthogonal projections with one of the projections

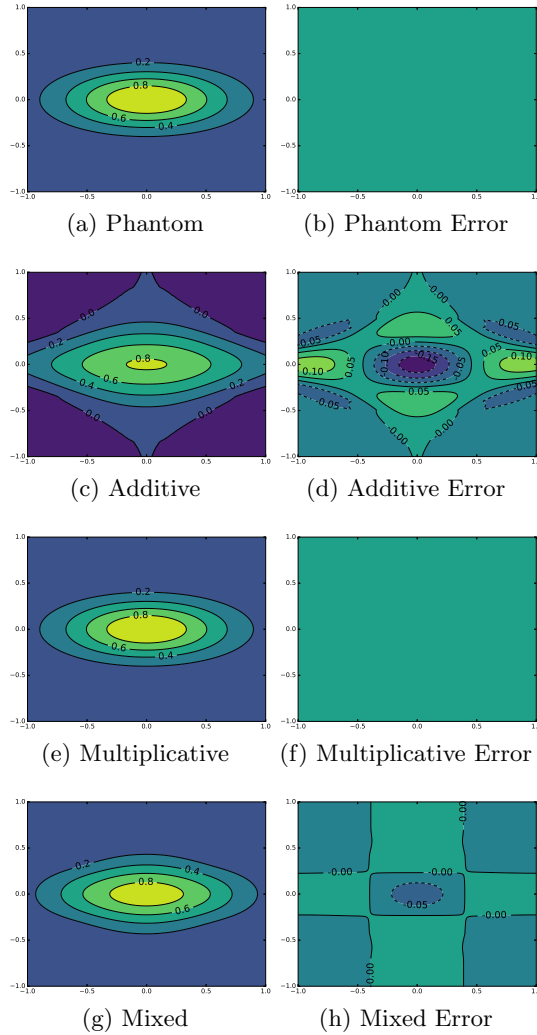


Figure 2.5: A demonstration of the strengths and weaknesses of the 2-projection (vertical and horizontal) additive, multiplicative, mixed, and simultaneous algebraic reconstruction technique (ART). The plots are based on the function $f(x,y) = e^{-(2x^2+10y^2)}$. Note: the reconstruction in (e) is an exact reconstruction of the image in (a).

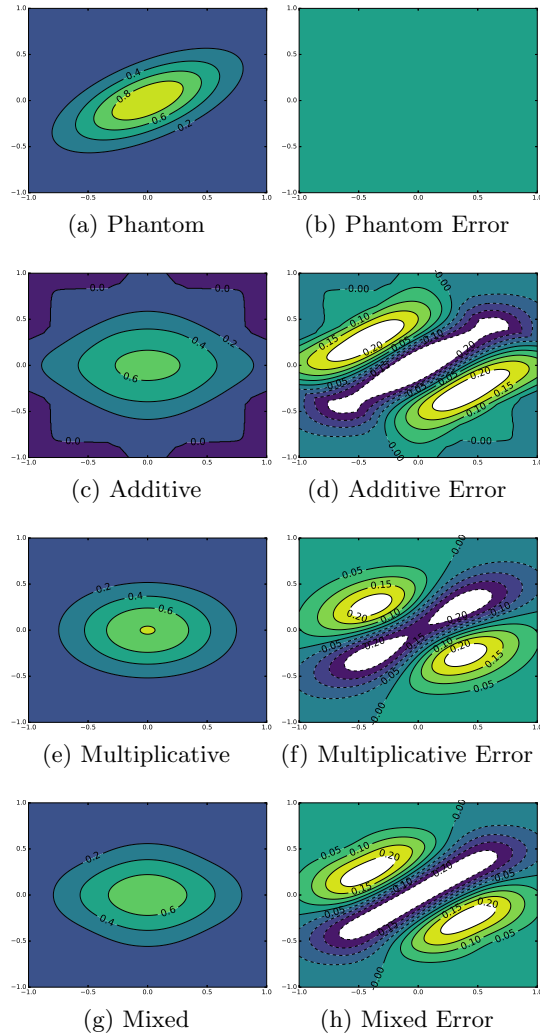


Figure 2.6: A demonstration of the strengths and weaknesses of the 2-projection (vertical and horizontal) additive, multiplicative, mixed, and simultaneous algebraic reconstruction technique (ART). The plots are based on the function $f(x, y) = e^{-(2x^2+10y^2)}$, rotated by 30° . These plots demonstrate how the 2-projection ART is unable to correctly capture the rotation of the density field.

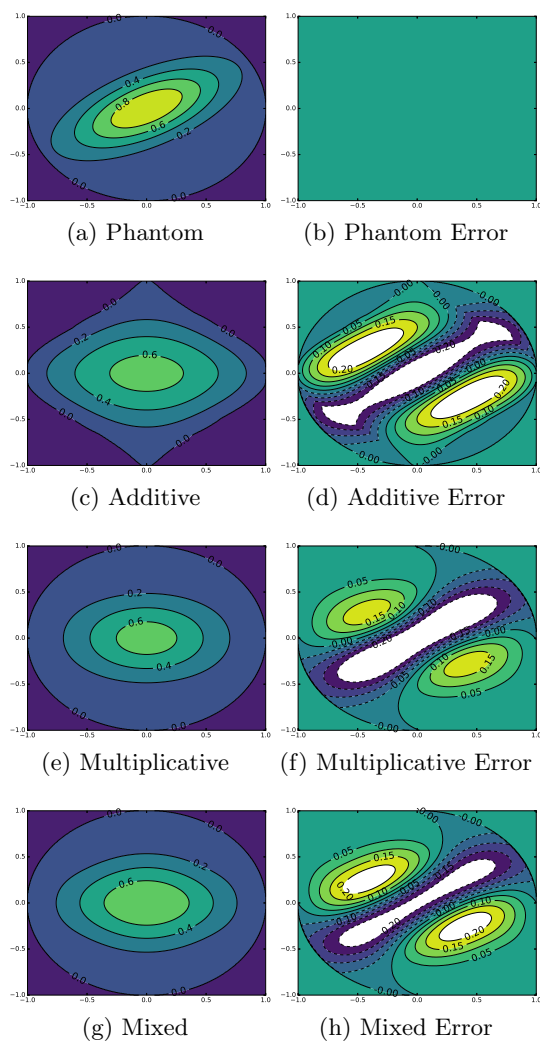


Figure 2.7: A demonstration of the strengths and weaknesses of the constrained 2-projection (vertical and horizontal) additive, multiplicative, mixed, and simultaneous algebraic reconstruction technique (ART). The plots are based on the function $f(x, y) = e^{-(2x^2 + 10y^2)}$, rotated by 30° and solved under the constraint that all points outside the unit circle are zero. The reconstruction using multiplicative ART (e)(f) did not converge.

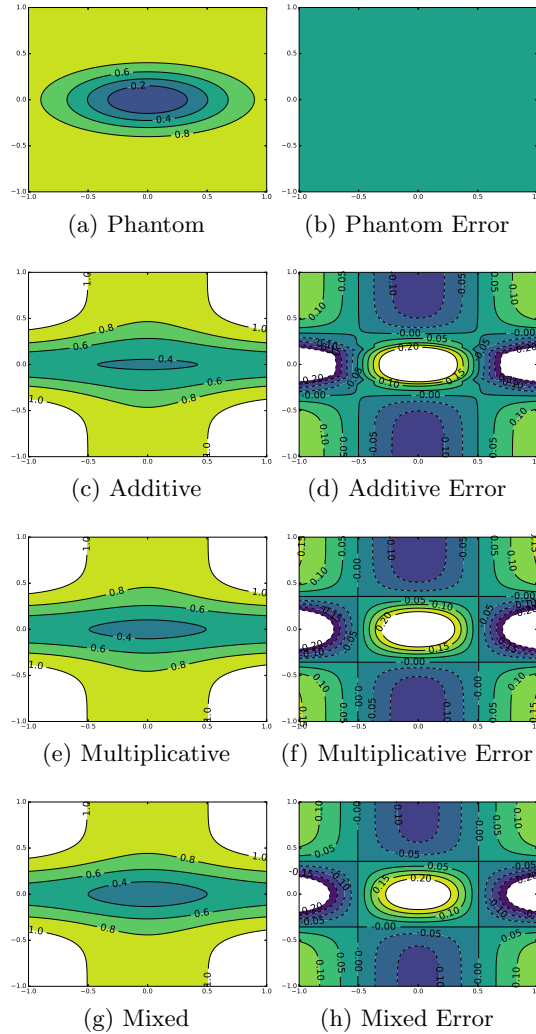


Figure 2.8: A demonstration of the strengths and weaknesses of the 2-projection (vertical and horizontal) additive, multiplicative, mixed, and simultaneous algebraic reconstruction technique (ART). The plots are based on the function $f(x, y) = 1 - e^{-(2x^2+10y^2)}$.

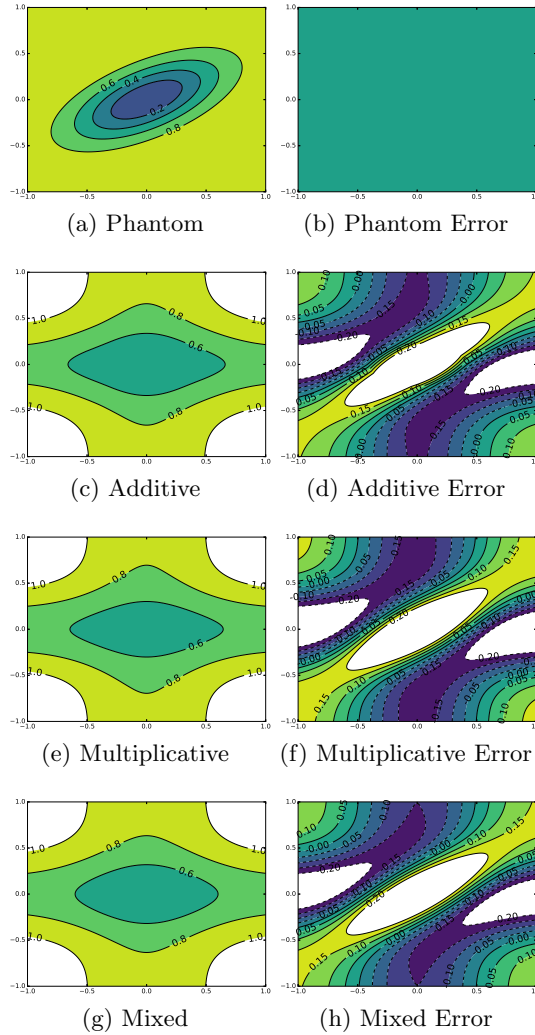


Figure 2.9: A demonstration of the strengths and weaknesses of the 2-projection (vertical and horizontal) additive, multiplicative, mixed, and simultaneous algebraic reconstruction technique (ART). The plots are based on the function $f(x, y) = 1 - e^{-(2x^2 + 10y^2)}$, rotated by 30° .

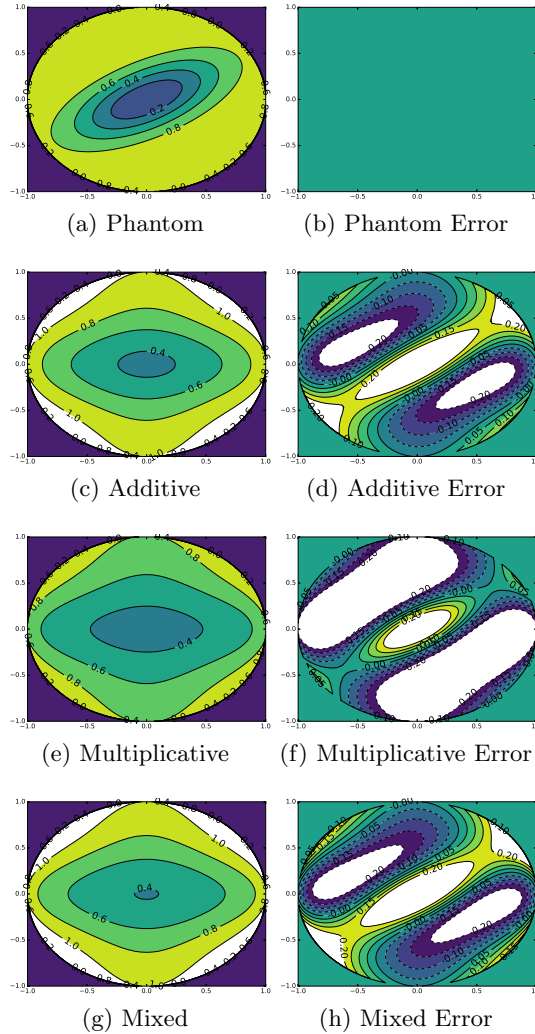


Figure 2.10: A demonstration of the strengths and weaknesses of the constrained 2-projection (vertical and horizontal) additive, multiplicative, mixed, and simultaneous algebraic reconstruction technique (ART). The plots are based on the function $f(x, y) = 1 - e^{-(2x^2 + 10y^2)}$, rotated by 30° and solved under the constraint that all points outside the unit circle are zero. The reconstruction using multiplicative ART (e)(f) did not converge.

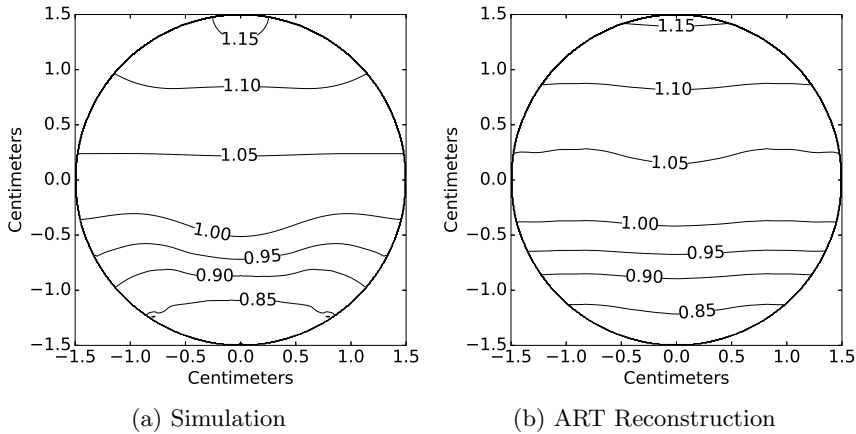


Figure 2.11: A virtual experiment where a representative density field is extracted from a ceramic powder compaction simulation and reconstructed from two orthogonal projections using multiplicative ART. The ART reconstruction method adequately reconstructs the density simulated field, although it does smooth along the projection directions. Because the method is insensitive to the magnitude of the density, the density field of the simulated green body is normalized according to the average density of the slice.

being in line with the only plane of symmetry. The results of the reconstruction, as well as the simulated green body density field, are presented in Figure 2.11.

For this virtual experiment, there is a consistent correlation between the density isosurfaces of the simulation and reconstruction but also a lack of curvature in the reconstruction that is present in the simulated density field. Nevertheless, the reconstructed density field sufficiently resembles the aggregate simulated density field to the extent that the location, magnitude, and size of large-scale density variations can be identified.

When using this density evaluation method to compare a simulated density field to an experimental field, it is recommended that both the simulation and the experiment are to be reconstructed from projections and the resulting reconstructions compared. In this way, the agreement between the simulation and experiment can be assessed in the same reconstruction space, subject to the same dissipation effects inherent to each reconstruction technique in order to yield two images that can be objectively compared. This allows for the case that the simulation accurately predicts the experimental density field

but that the reconstructed field does not exactly represent the actual solution. As discussed in Section 2.3.3, in only the most pathological instances will the reconstructed field exactly represent the actual field, such as in Figure 2.5e. While the set of density fields that satisfy the two projections is infinite, it is deemed unlikely that both a simulation and experiment would have the same projections with fundamentally different density fields.

2.5 Green Body Reconstruction

To complement the virtual experiment, the density analysis technique was used to analyze the truncated-cylinder green body depicted in Figure 2.1, with a diameter of 30.0mm, a maximum height of 9.1mm, and an upper-face inclination of 10° . The green body was formed under a mean axial stress of 120MPa, which is slightly more than the supplier-recommended 100MPa forming pressure to attain a green density of $2.4\text{g}/\text{cm}^3$. The analysis took advantage of the symmetry of the green body along the diameter, thereby yielding two mirror-images of the sample. These two sections of the green body were milled in perpendicular directions to give the minimum two projections to perform the reconstruction.

The sample was milled in transverse slices with a thickness of 1mm. Each transverse slice was partitioned into 1.5mm-wide strips (one-half of the sample milled in one direction and the other half in the perpendicular direction) and then progressively milled the partitioned sections and weighed. After measuring the projections of each transverse slice, the data can immediately be used to generate a reconstruction with a voxel size of $1.5\text{mm} \times 1.5\text{mm} \times 1.0\text{mm}$.

During analysis, it was found that the milled strips that contained relatively small mass were particularly sensitive to the flaking of the sample during milling causing significant variation in the calculated density for that piece. To overcome this, a smoothing step of the transverse slice projections was performed where the milled mass is transformed to density space and smoothed by minimizing a mass-weighted root-mean-squared error function subject to conservation of mass (see Figure 2.12). This gives more weight to the strips that had more mass and, therefore, a more accurate density value. Applying this smoothing step to all the projections allows for resampling of the projection data from the smoothed projections to get a higher resolution reconstruction. The high-resolution 3D reconstruction of the green body can be found in Figure 2.13.

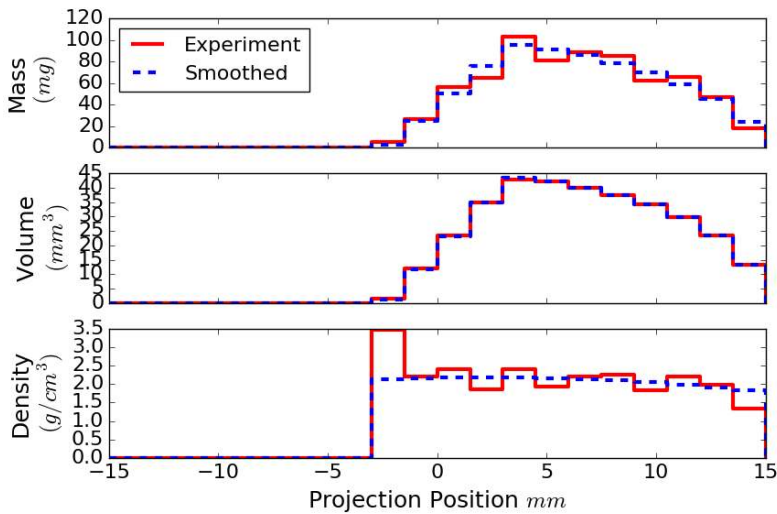
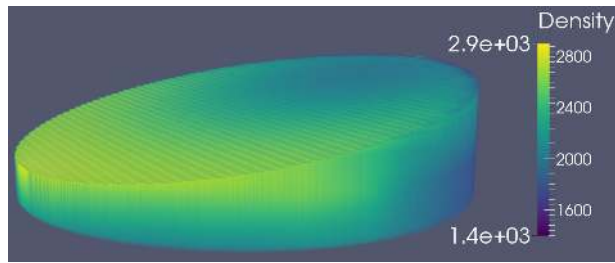


Figure 2.12: A demonstration of the method to regularize the projections in the presence of experimental variation (such as flaking) during the milling process. The experimentally-measured mass can be converted to density by dividing by projection-element volume (found by using sample geometry and milling path). The density profile can then be smoothed by minimizing a mass-weighted root-mean-squared error function while requiring total mass to be unchanged.

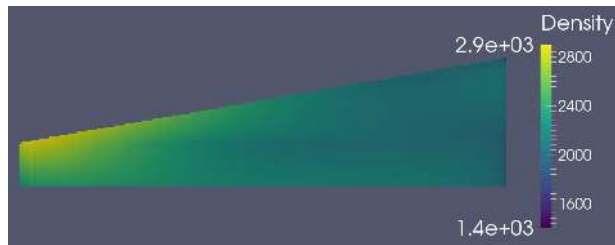
While two projections are unlikely to exactly reproduce the density field, general predictions about the density field can still be readily inferred from the reconstruction. From Figure 2.13, it can be seen that the bulk of the green body has a density that is approximately the reported green density for our alumina powder ($2.4\text{g}/\text{cm}^3$). There is also an area of much higher density, approaching $2.9\text{g}/\text{cm}^3$, at the pinch point and that the other areas of higher density are more localized at the corners of the inclined surface leaving a relatively lower density in the center.

2.6 Conclusion

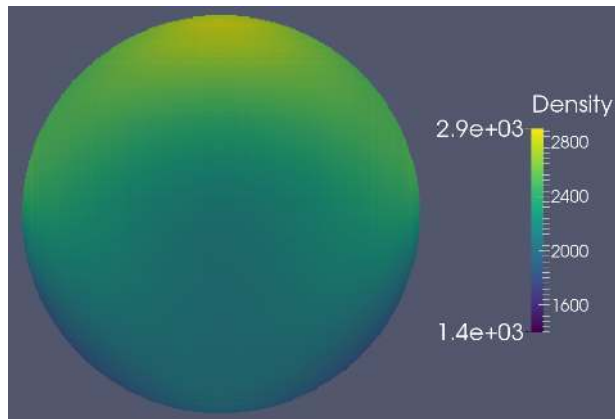
A simple, destructive method has been presented for determining internal density fields of ceramic green bodies, using only readily-available laboratory equipment. The method has been demonstrated as being able to represent location, magnitude, and extent of large-scale density variations with sufficient accuracy. Virtual experiments and experimental reconstructions have confirmed the utility of this method for determining and comparing density fields of green bodies and is now ready for use in research and industrial applications.



(a) 3D Render



(b) Axial Cross-Section



(c) Transverse Cross-Section

Figure 2.13: Visualized experimental data on a truncated cylindrical green body made of alumina powder (see Figure 2.1 for geometry specifications). All densities are given in kg/m^3 with 1200kg/m^3 as the uncompressed powder density and 2400kg/m^3 as the green density at 100MPa . The projections have been smoothed and then re-sampled from a strip width of 1.5mm to 0.1mm .

Appendix

2.A Moiré Diagrams

Tomographic reconstruction methods were developed after the advent of the personal computer because of the massive amount of computation required to perform even a single reconstruction. This is still applicable even today, where the tomographic reconstruction is often dependent on even more computationally-intensive methods. The method presented in this appendix is meant as a way to enable a researcher to reconstruct a density field by hand or with minimal computer assistance.

The history of moiré fringes or moiré patterns goes back to the the French word for the wavy look of Chinese silk. In present times, it usually refers to the interference pattern from two or more geometric patterns being superimposed onto one another. Applications for this phenomenon range from strain analysis[23], to medical techniques[51], to children's books[66]. However, the technique presented here can produce intricate interference patterns when the number of projections is high, but is more useful with fewer projections. This ensures that the attention of the viewer is not stolen by the interference pattern and keeping the number of projections relatively small guards against that. Figure 2.A.3f demonstrates that while there is a strong moiré pattern of concentric ellipses that happen to trace out isosurfaces, there are other patterns perpendicular to those that are completely non-physical. For that reason, it is suggested to keep the number of projections lower, rather than higher. The concept behind the use of moiré diagrams to communicate density field information is that the line intersection density is correlated with the relative density of the field in that vicinity.

To this end, the first step in producing a moiré diagram is to generate the data in much the same way as is presented in Section 2.3. The following demonstration will focus on a density field constrained to be within the unit circle with a density varying according to

$$f(x, y) = e^{-(2x^2+12.5y^2)} \quad (2.8)$$

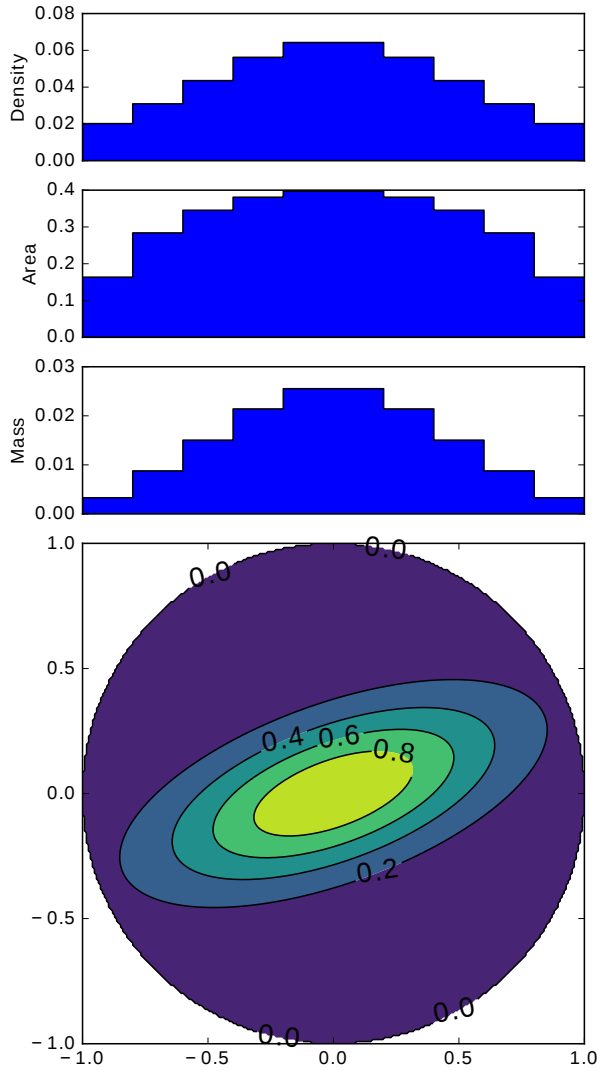


Figure 2.A.1: A single projection of a 2D gaussian function $f(x, y) = e^{-(2x^2 + 12.5y^2)}$, rotated by 20° where the domain of interest is the unit circle. This demonstrates a vertical projection into mass, area, and density data.

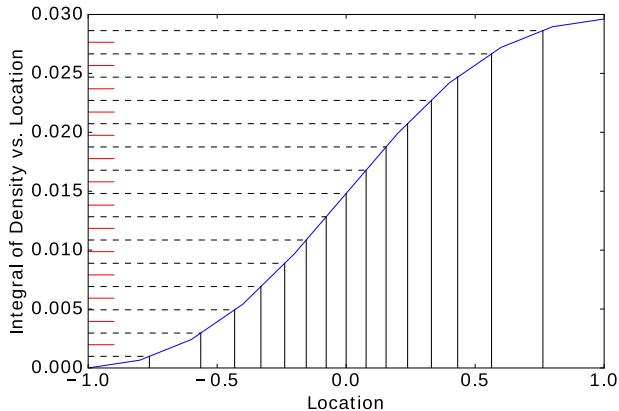


Figure 2.A.2: A graphical depiction of how to determine line spacing for the Moiré projection. The red lines are equally spaced along the ordinate, with the black lines being equally spaced between the red lines. Because the integral is strictly monotonic, the transformation from the evenly-spaced values along the ordinate to the abscissa is unique and easily found given the piecewise-linear nature of the integral.

and rotated counter-clockwise by 20° . A countour plot of the density field is presented in Figure 2.A.1. The following equation (repeated from Equation 2.1)

$$P_j = \int_{g_j} f(x, y) dy dx, \quad (2.9)$$

is evaluated for each projection cell j to produce the piecewise-constant “mass” plot $M(x)$ in Figure 2.A.1. The width of the projection strips is arbitrary, but as this method is intended to be possible to do by hand, ten equally-spaced strips were chosen. Then, the area of each strip is tabulated

$$A_j = \int_{g_j} dy dx, \quad (2.10)$$

to produce the piecewise-constant “area” plot $A(x)$ in Figure 2.A.1.

The piecewise-constant “density” plot $\rho(x)$ in Figure 2.A.1 is found by

$$\rho(x) = \frac{M(x)}{A(x)} \quad (2.11)$$

which gives the average density in the strips as a function of position.

It is intuitive that the parts of the projection with a higher average density should have a higher line density for the moiré diagram.

There are several methods for determining where and how to place the lines that can provide satisfactory results including arbitrarily setting a value of density ρ_{line} associated with one line and placing P_j/ρ_{line} lines in that cell. This method is prone to issues depending on whether or not the number of lines is rounded up or down or causing spurious effects when too many cells are used in a projection.

To alleviate this problem, it is suggested that a piecewise-linear integral of the piecewise-constant density function $\rho(x)$ in Figure 2.A.1 be calculated by

$$f(x) = \int_{-\infty}^x \rho(z) dz. \quad (2.12)$$

Because the density function is piecewise constant, the integral is piecewise linear, which is sufficiently simple that it could still be performed by hand. The integrated function is presented in Figure 2.A.2. Because it is an integral of a non-negative function the integral is assured to be monotonic and, when no zero-valued cells are present, it is strictly monotonic.

The monotonicity of the integral lends itself to being used as a mapping function between density and line placement. So, an arbitrary number of lines N can be chosen for the entire projection and the ordinate divided into N equal parts. In Figure 2.A.2, the number of lines N was chosen to be 15 to demonstrate that the number of lines and number of cells in the projection need not be the same. The short red lines along the ordinate represent the boundaries between the equal parts. Then, for each equal part a horizontal line is drawn (the black, dashed lines) from the middle of the section to the integrated function $f(x)$, the intersection giving the horizontal location of the line for that projection (the black, solid lines). This gives a method for determining line placement that is insensitive to the number of cells in the projection and can even have N be less than the number of cells and still give smooth results.

Figure 2.A.3 demonstrates the effect of the number of projections used for a reconstruction. The figure shows different reconstructions for various numbers of projections to depict the increasing resolution of a rotated object that is not in-line with one of the projections. For this example, using four projections seems to be sufficient to verify that the original density field is rotated and to approximate the angle of rotation. However, of the moiré diagrams presented, the five-projection reconstruction gives the best representation of the density field as well as the angle of rotation.

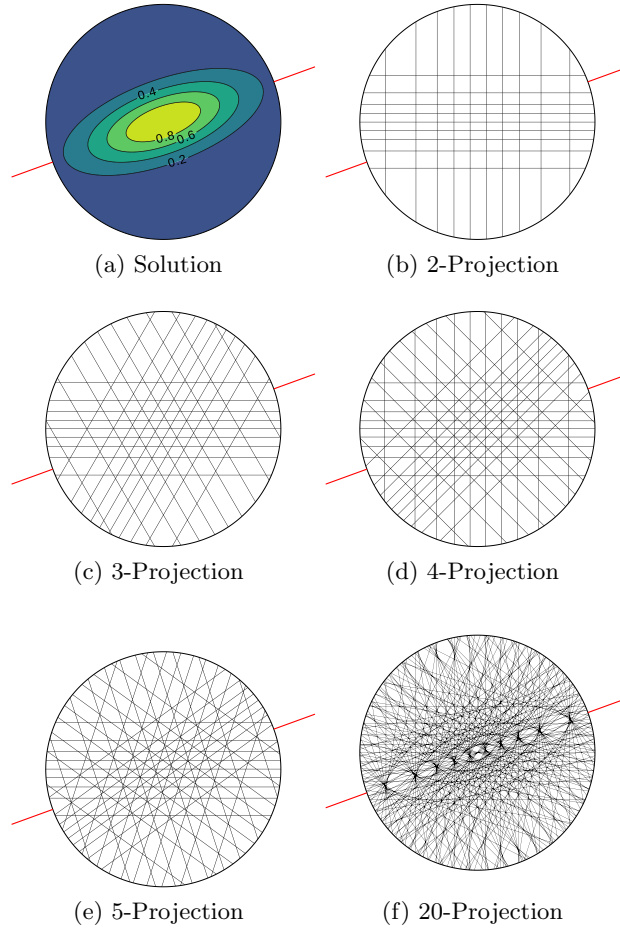


Figure 2.A.3: Reconstruction of a 2D gaussian function $f(x, y) = e^{-(2x^2+12.5y^2)}$, rotated by 20° (compare with Figure 2.7) where the domain of interest is the unit circle. The rotation angle of 20° was chosen so as to be large enough to be noticeable and yet not coincide with any of the projections, a worst-case scenario for determining orientation. The red axis protruding out of each circle is included only to demonstrate the angle by which the 2D gaussian was rotated.

Constitutive Modeling of the Cold-Forming of Ceramic Powders

The consistent, uniform pressing of green bodies is a necessary part of producing high-quality, high-performance ceramics with predictable qualities and behavior. Density variation in the compacted ceramic powder contributes directly to production waste of materials and energy, as well as a decrease in reliability because of the piece failing to meet quality standards or cracking during sintering. The careful control of the green body density field is of the utmost importance to consistently producing high-performance ceramics. Current methods for minimizing heterogeneity of the density field are often based on trial-and-error for mold geometry and forming pressure, which is both costly and prolongs development. The present research presents a continuum-level phenomenological constitutive model for accurately modeling the densification of ceramic powders into green bodies and outlines the numerical implementation of said model. The constitutive model incorporates nonlinear elasticity, elastic-plastic coupling, hydrostatic pressure-limit evolution, pressure- and Lode angle-dependent plasticity, nonassociated flow, and hardening.

3.1 Introduction

The modern world makes use of ceramics in nearly every segment of everyday life. Ceramics are used for bulletproof vests, spacecraft heat shields, mining, machining, nuclear fuels, and even brakepads. Because the uses are many and varied any increase in efficiency in the production process translates into huge time, energy, and environmental savings that would affect a multitude of industries. While the general behavior of ceramic powders has been treated thoroughly, the elastic-plastic behavior of ceramic powders has been little studied considering the numerous possible benefits[7].

The present research focuses on the production of the green bod-

ies from loose ceramic powder undergoing cold, quasistatic pressing. The compaction process is complex with an interplay of the powder response (elastic and plastic) as well as mold friction, aleatory uncertainty, and manufacturing limitations all contributing to the imperfections in the final green body[18, 49]. The negative effects of these imperfections underscore the importance of correctly forming the green bodies as even an optimal sintering process cannot make a flawed green body into a high-quality piece. For the reasons enumerated above, the subject of ceramic production and, specifically, green body formation have been studied for many decades. However, mold geometry and forming pressure are still largely determined through trial-and-error[46], although research efforts to model the compaction process have been ongoing for over two decades[33].

Recent advances in computing power are making virtual prototyping by numerical simulation and optimization possible for even very complex problems. Companies and organizations no longer need supercomputers or large compute clusters to start taking advantage of these tools to streamline research and development, decrease waste during production, and minimize the required time-to-market of advanced, high-performance ceramics. The purpose of this model is to aid industry in becoming more efficient and producing better ceramics through better green bodies.

3.2 Notation

Throughout this work scalars are in regular type (b), second-order tensors are bold (\mathbf{P}), and fourth-order tensors are in blackboard bold (\mathbb{E}). This work also makes use of special operators that act on second-order tensors and are given by

$$\begin{aligned}
 (\mathbf{A} \otimes \mathbf{B})[\mathbf{C}] &= (\mathbf{C} \cdot \mathbf{B}^T)\mathbf{A}, \\
 (\mathbf{A} \underline{\otimes} \mathbf{B})[\mathbf{C}] &= \frac{1}{2}\mathbf{A}(\mathbf{C} + \mathbf{C}^T)\mathbf{B}^T, \\
 (\mathbf{A} \underline{\otimes} \mathbf{B})[\mathbf{C}] &= \mathbf{A}\mathbf{C}\mathbf{B}^T, \\
 (\mathbf{A} \overline{\otimes} \mathbf{B})[\mathbf{C}] &= \mathbf{A}\mathbf{C}^T\mathbf{B}^T,
 \end{aligned} \tag{3.1}$$

or, in indicial notation,

$$\begin{aligned}
 (\mathbf{A} \otimes \mathbf{B})_{ijkl} \mathbf{C}_{kl} &= (\mathbf{B}_{lk} \mathbf{A}_{ij}) \mathbf{C}_{kl}, \\
 (\mathbf{A} \underline{\otimes} \mathbf{B})_{ijkl} \mathbf{C}_{kl} &= \left(\frac{1}{2} \mathbf{A}_{ir} (\delta_{rk} \delta_{sl} + \delta_{rl} \delta_{sk}) \mathbf{B}_{js} \right) \mathbf{C}_{kl}, \\
 (\mathbf{A} \underline{\otimes} \mathbf{B})_{ijkl} \mathbf{C}_{kl} &= (\mathbf{A}_{ik} \mathbf{B}_{jl}) \mathbf{C}_{kl}, \\
 (\mathbf{A} \overline{\otimes} \mathbf{B})_{ijkl} \mathbf{C}_{kl} &= (\mathbf{A}_{il} \mathbf{B}_{jk}) \mathbf{C}_{kl},
 \end{aligned} \tag{3.2}$$

such that the following property holds

$$\underline{\otimes} = \frac{1}{2} (\underline{\otimes} + \overline{\otimes}). \tag{3.3}$$

When these operators act on identity tensors they yield well-known fourth-order tensors that perform fundamental operations on second-order tensors

$$\begin{aligned}
 \mathbf{I} \underline{\otimes} \mathbf{I}: \mathbf{A} &= \mathbf{A} & \mathbf{I} \otimes \mathbf{I}: \mathbf{A} &= \text{tr}(\mathbf{A}) \mathbf{I} \\
 \mathbf{I} \overline{\otimes} \mathbf{I}: \mathbf{A} &= \mathbf{A}^T & \mathbf{I} \underline{\otimes} \mathbf{I}: \mathbf{A} &= \mathbf{A}^{sym} = \frac{1}{2}(\mathbf{A} + \mathbf{A}^T).
 \end{aligned} \tag{3.4}$$

3.3 Constitutive Model Theory

The challenging problem attacked by Piccolroaz et al.[58, 59] and extended here is how to accurately describe the transition of material behavior, induced by cold pressing, from the loose granular state (the ceramic powder) to the fully dense state (the green body). The granular state is characterized by a lack of cohesion (tensile strength), a drop-shaped yield surface with triangular deviatoric cross-section, and pressure dependence of the elastic response with induced anisotropy. The condensed state is more typical, with cohesion, a cigar-shaped yield surface, and linear elastic response. This section presents the governing laws and theory of the constitutive model.

3.3.1 Cooper and Eaton Compaction Relation

The basis of the present model is founded on the paper published by Cooper and Eaton[25] which relates inelastic volume change to hydrostatic pressure for compacting ceramic powders. In that paper, a simple relation was found to be able to fit the hydrostatic compression behavior of a wide variety of ceramic powders. The present model utilizes this relation to define the hardening behavior

of the hydrostatic compressive limit of the yield surface such that, under hydrostatic loading, their results are matched. Thus, the relation between hydrostatic pressure and inelastic volume change can be written in terms of p_c , the hydrostatic elastic limit, and $\text{tr } \epsilon_p$, the logarithmic volumetric plastic strain, as

$$\exp(\text{tr } \epsilon_p) = \det \mathbf{U}_p = 1 - \tilde{a}_1 g(p_c, \Lambda_1) - \tilde{a}_2 g(p_c, \Lambda_2) \quad (3.5)$$

where

$$g(p_c; \Lambda) = \begin{cases} \frac{p_c}{e\Lambda} & p_c < \Lambda \\ e^{-\Lambda/p_c} & \text{otherwise} \end{cases} \quad (3.6)$$

$$\frac{dg(p_c; \Lambda)}{dp_c} = \begin{cases} \frac{1}{e\Lambda} & p_c < \Lambda \\ \frac{\Lambda}{p_c^2} e^{-\Lambda/p_c} & \text{otherwise} \end{cases} \quad (3.7)$$

The relation between the parameters \tilde{a}_1 and \tilde{a}_2 with the parameters a_1 and a_2 as presented by Cooper and Eaton is $\tilde{a} = \phi_0 a$ where ϕ_0 is the initial porosity of the powder (and should not be confused with $\phi(\epsilon_e, \epsilon_p)$, the elastic strain-energy potential in Equation 3.13). The smooth, monotonic, continuous function $g(p_c; \Lambda)$ is introduced for numerical stability and does not negatively affect the fit of the data.

Experimental data and the parameterization for alumina powder is presented in Figure 4.1. Evolution of p_c is only allowed during compaction (when $\text{tr } \dot{\epsilon}_p < 0$) which ensures that a complete collapse of the yield surface does not occur under sustained tensile loading. Due to the formulation of the relation, there is no analytical solution to determine p_c from a given volumetric plastic strain (excepting pathological cases).

The hardening law has been implemented in the large-strain formulation, even though the remainder of the model uses small-strain assumptions. This choice was made as the use-cases for the model are inherently large-strain (the datasheet for KMS-96 states a 50% volume reduction when producing a green body) with the bulk of the volumetric strain being accumulated with loading aligned with the principal directions (during the powder phase with minimal frictional interaction from the mold). Finally, for the material in question, even at infinite forming pressure the small-strain formulation only predicts a 40% plastic volume reduction versus the manufacturer-suggestion 50% reduction at 100MPa.

This pressure-limit evolution law is the link between the weighted transition laws and the elastoplastic behavior of the material as this directly maps p_c to the volumetric plastic strain. While p_c cannot be

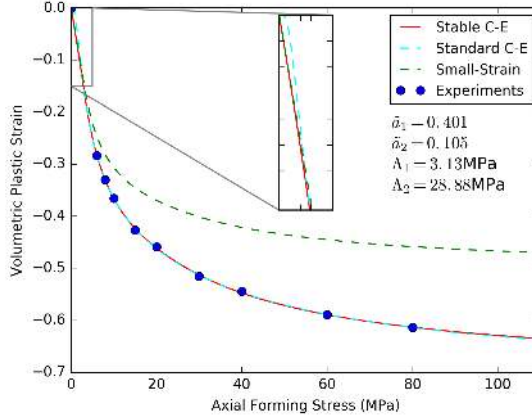


Figure 3.1: A demonstration of how to parameterize the Cooper and Eaton compaction relation using Martoxid KMS-96 alumina powder. A comparison with the small-strain version is included to demonstrate that it underpredicts by a large margin the volumetric plastic strain for a given forming pressure and is unable to achieve the manufacturer-recommended green body density at 100MPa.

directly solved for, it is possible to solve directly for the rate \dot{p}_c by finding $d \operatorname{tr} \epsilon_p / dp_c$, inverting it, and applying the chain rule to get

$$\dot{p}_c = \frac{dp_c}{d \operatorname{tr} \epsilon_p} \operatorname{tr} \dot{\epsilon}_p = - \frac{1 - \tilde{a}_1 g(p_c; \Lambda_1) - \tilde{a}_2 g(p_c; \Lambda_2)}{\tilde{a}_1 \frac{dg(p_c; \Lambda_1)}{dp_c} - \tilde{a}_2 \frac{dg(p_c; \Lambda_2)}{dp_c}}. \quad (3.8)$$

3.3.2 Weighted Transition Law

Inside the model there are several behaviors that are governed by the same linear-interpolation transition law presented by Argani et al[4]. In their research, they found that a simple exponential interpolant between the powder phase at zero pressure and condensed phase at infinite pressure fit the transition behavior of the elastic moduli very well. Because of the simplicity, elegance, and good fit for the elastic moduli evolution during compaction, the same interpolation law is implemented for yield surface evolution, but with different parameters. This yields a faster rate of change with smaller values of p_c and exponentially decreasing rate of change as the material approaches the theoretical fully-condensed state. The generic transformation law T of the quantity Q evolves with respect to the weighting function b

with p_c as the independent variable

$$T^Q(p_c) = b(p_c; \chi)Q_{initial} + (1 - b(p_c; \chi))Q_{final}, \quad b(p_c; \chi) \in [0, 1] \quad (3.9)$$

The unitless interpolating function is chosen to be

$$b(p_c; \chi) = e^{-\chi \langle p_c \rangle}, \quad \langle x \rangle = \begin{cases} 0 & x < 0 \\ x & x \geq 0 \end{cases} \quad (3.10)$$

so that a smooth evolution law over the range of p_c is obtained with χ as a constant function parameters and $\langle x \rangle$ representing the MacAuley brackets. As the parameter p_c has units of stress, χ has units of inverse stress so that the mixing function b remains unitless. The parameter χ (the ‘speed parameter’) controls the rate of transformation with larger values increasing the rate of transformation from the initial state to the final state. While the weighting function is here written with the independent variable p_c , it may also be written with the independent variable ϵ_p because of the relation in presented later in Equation 3.5. There is no difference between the two notations.

Denoting a time rate with a superposed dot, the rate of this general transformation law is given by

$$\dot{T}^Q = \dot{b}(p_c; \chi) (Q_{initial} - Q_{final}) \quad (3.11)$$

where

$$\dot{b}(p_c; \chi) = -\chi e^{-\chi \langle p_c \rangle} \dot{p}_c. \quad (3.12)$$

The rate \dot{p}_c is defined by the Cooper and Eaton compaction relation (Section 3.3.1).

3.3.3 Parameters Subject to the Weighted Transition Law

A crucial feature of our constitutive model is the transition between the initial and final states are cast as elastoplastic evolution through the dependence on the consolidation pressure \dot{p}_c . The plastic deformation drives the evolution of the material behaviour from that typical of a granular state (ceramic powders) to that typical of a compact state (green bodies).

We assume all of the transition laws are of the form of Equation 3.9, controlled by the weighting function $b(p_c; \chi)$, so that the generic transformation law T can be applied to multiple parameters independently by applying different values of χ . The constitutive model has

three different χ values that control different physics, denoted χ_e , χ_c , and χ_f that control the elastic moduli, the cohesion, and the yield function parameters respectively. Instead of writing the full function definition, the notation will be simplified to b_e , b_c , and b_f where the subscripts denote the version of χ to apply.

Therefore, the transformation laws are the following:

- The Elastic potential energy function

$$\phi(\epsilon_e, \epsilon_p) = b_e \phi_I(\epsilon_e) + (1 - b_e) \phi_{II}(\epsilon_e), \quad (3.13)$$

where ϵ_e and ϵ_p denote logarithmic elastic and plastic strain, respectively, and is used throughout this paper. This behavior is controlled by the speed parameter, χ_e , and is discussed further in Section 3.3.4.

- The cohesion c (tensile hydrostatic cutoff)

$$c = b_c c_I + (1 - b_c) c_{II}, \quad (3.14)$$

where c_I , c_{II} , and χ_c are material parameters.

- The yield surface shape-parameters η , m , α , β , and γ (discussed in Section 3.3.5)

$$\eta = b_f \eta_I + (1 - b_f) \eta_{II} \quad (3.15a)$$

$$m = b_f m_I + (1 - b_f) m_{II} \quad (3.15b)$$

$$\alpha = b_f \alpha_I + (1 - b_f) \alpha_{II} \quad (3.15c)$$

$$\beta = b_f \beta_I + (1 - b_f) \beta_{II} \quad (3.15d)$$

$$\gamma = b_f \gamma_I + (1 - b_f) \gamma_{II} \quad (3.15e)$$

where two complete yield surfaces are defined with the parameter suffix I denoting the parameter describing the granular state and II denoting parameters for the fully-condensed state. These parameters all evolve with the same speed parameter χ_f as a parameter in $b(p_c)$. For powder compaction it is suggested that the following dense state parameters be set $\alpha_{II} = 1$, $m_{II} = 2$, and $\gamma_{II} = 0$

3.3.4 Elastic potential

Additive decomposition of the strain into elastic and plastic strains is assumed

$$\epsilon = \epsilon_e + \epsilon_p. \quad (3.16)$$

With the elastic and plastic strains defined, it is possible to define the elastic potential energies for the initial and final states.

- Elastic potential for initial powder (Phase I, $b(p_c) = 1$)

$$\phi_I(\boldsymbol{\epsilon}_e) = \frac{\lambda_I}{2} |\text{tr } \boldsymbol{\epsilon}_e|^n + \mu_I [\text{tr } (\boldsymbol{\epsilon}_e^2)]^l, \quad (3.17)$$

where λ_I , μ_I , n , and l are constant material parameters. A potential of the type in Equation 3.17 has been introduced and motivated on the basis of experiments for the description of the behaviour of granular materials by Gajo and Bigoni[31]. Linear elastic behavior can be achieved by setting $n = 2$ and $l = 1$ then λ_I and μ_I are the Lamé constants.

- Elastic potential for the final green body (Phase II, $b(p_c) = 0$)

$$\phi_{II}(\boldsymbol{\epsilon}_e) = \frac{\lambda_{II}}{2} (\text{tr } \boldsymbol{\epsilon}_e)^2 + \mu_{II} \text{tr } \boldsymbol{\epsilon}_e^2, \quad (3.18)$$

where λ_{II} and μ_{II} are the first and second Lamé constants.

These two elastic potentials are inserted into Equation 3.13 that yields a single elastic potential function that transitions between the initial and final elastic behaviors.

3.3.5 Yield function

The existence of a yield surface is assumed such that when the stress state is inside of this surface the deformation is entirely elastic. The form of the yield surface is taken from Bigoni[6] and Piccolroaz[57] and reproduced here as

$$F(\boldsymbol{\sigma}) = f(p) + \frac{q}{g(\theta)}, \quad (3.19)$$

in which the meridional and deviatoric functions take the form

$$f(p) = \begin{cases} -\eta p_c \sqrt{(\Phi - \Phi^m) [2(1 - \alpha)\Phi + \alpha]}, & \Phi \in [0, 1], \\ +\infty, & \Phi \notin [0, 1], \end{cases} \quad (3.20)$$

$$\frac{1}{g(\theta)} = \cos \left[\beta \frac{\pi}{6} - \frac{\cos^{-1}(\gamma \cos 3\theta)}{3} \right] \quad (3.21)$$

respectively, where

$$\Phi = \frac{p + c}{p_c + c}, \quad (3.22)$$

and p, q and θ are stress invariants defined by

$$p = -\frac{\text{tr } \boldsymbol{\sigma}}{3}, \quad q = \sqrt{3J_2}, \quad \theta = \frac{1}{3} \arccos \left(\frac{3\sqrt{3}}{2} \frac{J_3}{J_2^{3/2}} \right), \quad (3.23)$$

in which J_2 and J_3 the second and third invariant of the deviatoric stress \mathbf{S}

$$J_2 = \frac{1}{2} \text{tr } \mathbf{S}^2, \quad J_3 = \frac{1}{3} \text{tr } \mathbf{S}^3, \quad \mathbf{S} = \boldsymbol{\sigma} - \frac{\text{tr } \boldsymbol{\sigma}}{3} \mathbf{I}, \quad (3.24)$$

where \mathbf{I} is the identity tensor.

The seven material parameters defining the meridional shape function $f(p)$ and the deviatoric shape function $g(\theta)$ have a restricted range of definition to preserve convexity and smoothness and have a precise mechanical meaning. These are defined below.

- $p_c > 0$ is the preconsolidation pressure. The maximum pressure to which the material has been exposed.
- $c \geq 0$ is the cohesion (related to the capability of the material of sustaining tensile stresses). Initially null when the material is in the granular state.
- $\eta > 0$ relates the shear strength to the preconsolidation pressure p_c . The capability of granular material of sustaining larger shear stresses at increasing mean pressure.
- $0 < \alpha < 2$ and $m > 1$ are shape factors for the meridional section of the yield surface. They describe the pressure-dependence of the yield surface.
- $0 \leq \beta \leq 2$ and $0 \leq \gamma < 1$ are shape factors for the deviatoric section of the yield surface. The parameter β controls the bias towards triaxial compression or triaxial extension states and γ controls the smoothness of the corners (with vertices as $\gamma \rightarrow 1$).

The yield surface normal is defined as

$$\mathbf{Q} = \frac{\partial F(\boldsymbol{\sigma})}{\partial \boldsymbol{\sigma}}. \quad (3.25)$$

While the tensor \mathbf{Q} is not unique because the yield function is not unique, the direction of \mathbf{Q} is unique when evaluated on the yield surface.

3.3.6 Nonassociativity

The necessity of including non-associativity is debated [11]. However, the ability to enable it is nevertheless included in this model. Recognizing and complying with the points made in [10], nonassociativity

is not implemented using a flow function, as is often done. This obviates the problems inherent with non-uniqueness in yield and flow functions by calculating the flow direction using only the unique yield function and associated state information. The flow direction \mathbf{P} is implemented in the following form

$$\mathbf{P} = \mathbf{Q} - \frac{\epsilon(1 - \Phi) \operatorname{tr} \mathbf{Q}}{3} \mathbf{I}, \quad \epsilon \in [0, 1), \quad (3.26)$$

yielding an associated flow rule when $\epsilon = 0$.

3.3.7 Combining the Constitutive Equations

The stress is computed by taking the derivative of the total elastic strain energy function with respect to the elastic strain

$$\boldsymbol{\sigma} = b_e \frac{\partial \phi_I(\boldsymbol{\epsilon}_e)}{\partial \boldsymbol{\epsilon}_e} + (1 - b_e) \frac{\partial \phi_{II}(\boldsymbol{\epsilon}_e)}{\partial \boldsymbol{\epsilon}_e}, \quad (3.27)$$

given

$$\frac{\partial \phi_I(\boldsymbol{\epsilon}_e)}{\partial \boldsymbol{\epsilon}_e} = \frac{\lambda_I n}{2} |\operatorname{tr} \boldsymbol{\epsilon}_e|^{n-2} \operatorname{tr} \boldsymbol{\epsilon}_e \mathbf{I} + 2\mu_I l (\operatorname{tr} \boldsymbol{\epsilon}_e^2)^{l-1} \boldsymbol{\epsilon}_e, \quad (3.28)$$

and

$$\frac{\partial \phi_{II}(\boldsymbol{\epsilon}_e)}{\partial \boldsymbol{\epsilon}_e} = \frac{\lambda_{II}}{2} \operatorname{tr} \boldsymbol{\epsilon}_e \mathbf{I} + 2\mu_{II} \boldsymbol{\epsilon}_e. \quad (3.29)$$

Equation 3.27 is a nonlinear equation in $\boldsymbol{\epsilon}_e$ can be rewritten as

$$\boldsymbol{\sigma} = [b_e \mathbb{A} + (1 - b_e) \mathbb{B}] \boldsymbol{\epsilon}_e, \quad (3.30)$$

where

$$\begin{aligned} \mathbb{A} &= \frac{\lambda_I n}{2} |\operatorname{tr} \boldsymbol{\epsilon}_e|^{n-2} \mathbf{I} \otimes \mathbf{I} + 2\mu_I l (\operatorname{tr} \boldsymbol{\epsilon}_e^2)^{l-1} \mathbf{I} \underline{\otimes} \mathbf{I}, \\ \mathbb{B} &= \frac{\lambda_{II}}{2} \mathbf{I} \otimes \mathbf{I} + 2\mu_{II} \mathbf{I} \underline{\otimes} \mathbf{I}. \end{aligned} \quad (3.31)$$

Taking the rate of Equation 3.27 and using the rate form of the additive strain decomposition from Equation 3.16 we obtain

$$\dot{\boldsymbol{\sigma}} = \mathbb{E}[\dot{\boldsymbol{\epsilon}}] - \left\{ \mathbb{E} - \left[(\mathbb{A} - \mathbb{B}) \boldsymbol{\epsilon}_e \otimes \frac{\partial b_e}{\partial \boldsymbol{\epsilon}_e} \right] \right\} \dot{\boldsymbol{\epsilon}}_p, \quad (3.32)$$

3. Constitutive Modeling of the Cold-Forming of Ceramic Powders

where the fourth-order elastic tensor is defined as

$$\mathbb{E} = b_e \mathbb{A} + (1 - b_e) \mathbb{B} + b_e \left\{ \lambda_I \frac{n(n-2)}{2} |\text{tr } \boldsymbol{\epsilon}_e|^{n-2} \mathbf{I} \otimes \mathbf{I} + 4\mu_I l(l-1) (\text{tr } \boldsymbol{\epsilon}_e^2)^{l-2} \boldsymbol{\epsilon}_e \otimes \boldsymbol{\epsilon}_e \right\}, \quad (3.33)$$

which can be written in the compact form

$$\mathbb{E} = \omega_1 \mathbf{I} \otimes \mathbf{I} + \omega_2 \mathbf{I} \underline{\otimes} \mathbf{I} + \omega_3 \boldsymbol{\epsilon}_e \otimes \boldsymbol{\epsilon}_e, \quad (3.34)$$

where

$$\begin{aligned} \omega_1 &= b_e \lambda_I \frac{n(n-1)}{2} |\text{tr } \boldsymbol{\epsilon}_e|^{n-2} + (1 - b_e) \lambda_{II} \\ \omega_2 &= 2b_e \mu_I l \text{tr } (\boldsymbol{\epsilon}_e^2)^{l-1} + 2(1 - b_e) \mu_{II} \\ \omega_3 &= 4b_e \mu_I l(l-1) \text{tr } (\boldsymbol{\epsilon}_e^2)^{l-2}. \end{aligned} \quad (3.35)$$

The determinant of the elastic tensor in Equation 3.34 is (Appendix A)

$$\det \mathbb{E} = \omega_2^4 [(\omega_2 + 3\omega_1)\omega_2 - \omega_1\omega_3 \text{tr}^2 \boldsymbol{\epsilon}_e + (\omega_2 + 3\omega_1)\omega_3 \text{tr } \boldsymbol{\epsilon}_e^2], \quad (3.36)$$

and its inverse (understood to be restricted to the space of all symmetric tensors, such that $\mathbb{E}\mathbb{E}^{-1} = \mathbf{I} \underline{\otimes} \mathbf{I}$, see Appendix A) is

$$\mathbb{E}^{-1} = \frac{1}{\omega_2} \mathbf{I} \underline{\otimes} \mathbf{I} + \Omega_1 \mathbf{I} \otimes \mathbf{I} + \Omega_2 (\boldsymbol{\epsilon}_e \otimes \mathbf{I} + \mathbf{I} \otimes \boldsymbol{\epsilon}_e) + \Omega_3 (\boldsymbol{\epsilon}_e \otimes \boldsymbol{\epsilon}_e), \quad (3.37)$$

where

$$\begin{aligned} \Omega_1 &= -\frac{\omega_1 \omega_2^3 (\omega_2 + \omega_3 \text{tr } \boldsymbol{\epsilon}_e^2)}{\det \mathbb{E}}, \\ \Omega_2 &= \frac{\omega_1 \omega_2^3 \omega_3 \text{tr } \boldsymbol{\epsilon}_e}{\det \mathbb{E}}, \\ \Omega_3 &= -\frac{\omega_3 \omega_2^3 (\omega_2 + 3\omega_1)}{\det \mathbb{E}}. \end{aligned} \quad (3.38)$$

Now we define the rate of the inelastic strain[31], which is different from the rate of the plastic strain, as

$$\dot{\boldsymbol{\epsilon}}_i = \mathbb{G}[\dot{\boldsymbol{\epsilon}}_p], \quad (3.39)$$

where

$$\mathbb{G} = \mathbf{I} \underline{\otimes} \mathbf{I} - [\mathbb{E}^{-1}(\mathbb{A} - \mathbb{B})\boldsymbol{\epsilon}_e] \otimes \frac{\partial b_e}{\partial \boldsymbol{\epsilon}_p}, \quad (3.40)$$

and does not possess major symmetry (except for pathological cases). The invertibility of \mathbb{G} is crucial, since it allows the calculation of the plastic strain rate from the knowledge of the irreversible strain rate. To this end, we require the determinant of \mathbb{G} , given by

$$\det \mathbb{G} = 1 - [\mathbb{E}^{-1}(\mathbb{A} - \mathbb{B})\boldsymbol{\epsilon}_e] \cdot \frac{\partial b_e}{\partial \boldsymbol{\epsilon}_p}, \quad (3.41)$$

to be *strictly positive*, such that the inverse of \mathbb{G} (again restricted to the space of symmetric tensors) can be written as

$$\mathbb{G}^{-1} = \mathbf{I} \underline{\otimes} \mathbf{I} + \frac{1}{\det \mathbb{G}} [\mathbb{E}^{-1}(\mathbb{A} - \mathbb{B})\boldsymbol{\epsilon}_e] \otimes \frac{\partial b_e}{\partial \boldsymbol{\epsilon}_p}. \quad (3.42)$$

The rate of the inelastic strain is determined by a flow rule, much like the rate of plastic strain in other models

$$\dot{\boldsymbol{\epsilon}}_i = \dot{\lambda} \mathbf{P}, \quad (3.43)$$

where λ plays the role of a strictly positive plastic multiplier, null when the plastic flow is null.

Using the irreversible strain flow rule in Equation 3.43 and putting it into Equation 3.32 a familiar result is obtained

$$\dot{\boldsymbol{\sigma}} = \mathbb{E}[\dot{\boldsymbol{\epsilon}}] - \dot{\lambda} \mathbb{E}[\mathbf{P}], \quad (3.44)$$

and, using consistency,

$$\dot{F} = \mathbf{Q} \cdot \dot{\boldsymbol{\sigma}} - \dot{\lambda} h = 0, \quad \mathbf{Q} = \frac{\partial F}{\partial \boldsymbol{\sigma}} \quad (3.45)$$

the plastic modulus can be derived as

$$-\dot{\lambda} h = \frac{\partial F}{\partial p_c} \dot{p}_c + \frac{\partial F}{\partial c} \dot{c} + \frac{\partial F}{\partial \eta} \dot{\eta} + \frac{\partial F}{\partial m} \dot{m} + \frac{\partial F}{\partial \alpha} \dot{\alpha} + \frac{\partial F}{\partial \beta} \dot{\beta} + \frac{\partial F}{\partial \gamma} \dot{\gamma}, \quad (3.46)$$

and expanded using the chain rule

$$-\dot{\lambda} h = \left[\frac{\partial F}{\partial p_c} + \frac{\partial F}{\partial c} \frac{\partial c}{\partial b_c} \frac{\partial b_c}{\partial p_c} + \left(\frac{\partial F}{\partial \eta} \frac{\partial \eta}{\partial b_f} + \frac{\partial F}{\partial m} \frac{\partial m}{\partial b_f} + \frac{\partial F}{\partial \alpha} \frac{\partial \alpha}{\partial b_f} + \frac{\partial F}{\partial \beta} \frac{\partial \beta}{\partial b_f} + \frac{\partial F}{\partial \gamma} \frac{\partial \gamma}{\partial b_f} \right) \frac{\partial b_f}{\partial p_c} \right] \dot{p}_c \quad (3.47)$$

which clearly demonstrates the role of the hardening parameters and the dependence on the transition function b .

The plastic multiplier $\dot{\lambda}$ can be obtained from Equation 3.47 and substituted into Equation 3.44 to obtain the rate constitutive equations in the standard form

$$\begin{aligned}\dot{\boldsymbol{\sigma}} &= \mathbb{E}[\dot{\boldsymbol{\epsilon}}] - \frac{\mathbf{Q} \cdot \mathbb{E}[\dot{\boldsymbol{\epsilon}}]}{h + \mathbf{Q} \cdot \mathbb{E}[\mathbf{P}]} \mathbb{E}[\mathbf{P}], & \text{if } F(\boldsymbol{\sigma}) = 0, \\ \dot{\boldsymbol{\sigma}} &= \mathbb{E}[\dot{\boldsymbol{\epsilon}}], & \text{if } F(\boldsymbol{\sigma}) < 0,\end{aligned}\tag{3.48}$$

where:

- the elastic fourth-order tensor \mathbb{E} is given by Equation 3.33,
- the hardening modulus h can be found using Equation 3.47,
- the flow direction \mathbf{P} discussed in Section 3.3.6 can be equal to the yield function gradient \mathbf{Q} when $\epsilon = 0$, yielding associated flow.

3.4 Conclusions

A novel ceramic powder compaction model is presented. It incorporates nonlinear elasticity, pressure- and Lode-angle-dependent yield surfaces, yield surface evolution, nonassociativity, and a special form of elastoplastic coupling. The model is capable of describing the entire spectrum of the compaction process, from the powder phase to the fully compressed phase and all the states inbetween. The predictive capabilities of the model were demonstrated with a comparison of density fields from a numerical simulation and an experiment. The density fields were compared in a reconstructed space after evaluating projections and reconstructing them using tomographic reconstruction methods. The reconstructed density fields agreed to a large extent and give confidence that the model is accurately predicting the actual density field of the green body. The model has been implemented into a numerical routine and shown to be able to give results in a reasonable amount of time using regular desktop computers, which would allow it to be used in industry and also smaller research institutions.

Appendix

3.A Inverses of Selected Fourth-Order Tensors

The discussion in this appendix is specific to the class of tensors like those in Equation 3.34 and Equation 3.40. Given the scalars a and b , and the symmetric second-order tensors \mathbf{A} and \mathbf{B} , we consider the fourth-order tensor

$$\mathbb{C} = a\mathbf{I} \otimes \mathbf{I} + b\mathbf{I} \underline{\otimes} \mathbf{I} + \mathbf{A} \otimes \mathbf{B}, \quad (3.49)$$

which is a generalization of tensors in Equation 3.34 and Equation 3.40.

First, we assume invertibility of \mathbb{C} and find the inverse. For all tensors $\mathbf{X} \in \text{Sym}$ we have

$$\mathbb{C}[\mathbf{X}] = a(\text{tr } \mathbf{X})\mathbf{I} + b\mathbf{X} + (\mathbf{B} \cdot \mathbf{X})\mathbf{A}, \quad (3.50)$$

so that

$$\mathbf{X} = a(\text{tr } \mathbf{X})\mathbb{C}^{-1}[\mathbf{I}] + b\mathbb{C}^{-1}[\mathbf{X}] + (\mathbf{B} \cdot \mathbf{X})\mathbb{C}^{-1}[\mathbf{A}], \quad (3.51)$$

and consequently we obtain

$$\mathbb{C}^{-1}[\mathbf{X}] = \frac{1}{b} \{ \mathbf{X} - a(\text{tr } \mathbf{X})\mathbb{C}^{-1}[\mathbf{I}] - (\mathbf{B} \cdot \mathbf{X})\mathbb{C}^{-1}[\mathbf{A}] \}. \quad (3.52)$$

Using Equation 3.52 with $\mathbf{X} = \mathbf{I}$ and $\mathbf{X} = \mathbf{A}$ we arrive at the following linear system for $\mathbb{C}^{-1}[\mathbf{I}]$ and $\mathbb{C}^{-1}[\mathbf{A}]$

$$\mathbb{C}^{-1}[\mathbf{I}] = \frac{1}{b} \{ \mathbf{I} - 3a\mathbb{C}^{-1}[\mathbf{I}] - (\text{tr } \mathbf{B})\mathbb{C}^{-1}[\mathbf{A}] \}, \quad (3.53)$$

$$\mathbb{C}^{-1}[\mathbf{A}] = \frac{1}{b} \{ \mathbf{A} - a(\text{tr } \mathbf{A})\mathbb{C}^{-1}[\mathbf{I}] - (\mathbf{B} \cdot \mathbf{A})\mathbb{C}^{-1}[\mathbf{A}] \},$$

which can be solved to yield

$$\mathbb{C}^{-1}[\mathbf{I}] = \frac{b + \mathbf{A} \cdot \mathbf{B}}{D} \mathbf{I} - \frac{\text{tr } \mathbf{B}}{D} \mathbf{A}, \quad \mathbb{C}^{-1}[\mathbf{A}] = \frac{3a + b}{D} \mathbf{A} - \frac{a \text{tr } \mathbf{A}}{D} \mathbf{I}, \quad (3.54)$$

where

$$D = (3a + b)b - a(\text{tr } \mathbf{A})(\text{tr } \mathbf{B}) + (3a + b)(\mathbf{A} \cdot \mathbf{B}), \quad (3.55)$$

a quantity which is clearly equal or proportional to the determinant of \mathbb{C} . A substitution of Equation 3.54 into Equation 3.52 yields the inverse of the fourth-order tensor \mathbb{C}

$$\begin{aligned} \mathbb{C}^{-1} = \frac{1}{b} \mathbf{I} \underline{\otimes} \mathbf{I} - \frac{a(b + \mathbf{A} \cdot \mathbf{B})}{bD} \mathbf{I} \otimes \mathbf{I} + \frac{a \text{tr } \mathbf{B}}{bD} \mathbf{A} \otimes \mathbf{I} \\ + \frac{a \text{tr } \mathbf{A}}{bD} \mathbf{I} \otimes \mathbf{B} - \frac{3a + b}{bD} \mathbf{A} \otimes \mathbf{B}. \end{aligned} \quad (3.56)$$

To conclude our analysis we provide a complete spectral analysis of the tensor \mathbb{C} in Equation 3.49. We rewrite the fourth-order tensor \mathbb{C} splitting tensors \mathbf{A} and \mathbf{B} into their deviatoric and isotropic components as

$$\begin{aligned} \mathbb{C} = \left(a + \frac{\text{tr } \mathbf{A} \text{tr } \mathbf{B}}{9} \right) \mathbf{I} \otimes \mathbf{I} + b \mathbf{I} \underline{\otimes} \mathbf{I} \\ + \frac{\text{tr } \mathbf{B}}{3} \text{dev } \mathbf{A} \otimes \mathbf{I} + \frac{\text{tr } \mathbf{A}}{3} \mathbf{I} \otimes \text{dev } \mathbf{B} + \text{dev } \mathbf{A} \otimes \text{dev } \mathbf{B}, \end{aligned} \quad (3.57)$$

from which it follows that

$$\mathbb{C}[\mathbf{R}] = b\mathbf{R}, \quad \mathbb{C}^T[\mathbf{L}] = b\mathbf{L}, \quad (3.58)$$

for all \mathbf{R} satisfying

$$\text{tr } \mathbf{R} = 0, \quad \text{and} \quad \mathbf{R} \cdot \text{dev } \mathbf{B} = 0, \quad (3.59)$$

and all \mathbf{L} satisfying

$$\text{tr } \mathbf{L} = 0, \quad \text{and} \quad \mathbf{L} \cdot \text{dev } \mathbf{A} = 0. \quad (3.60)$$

We conclude that b is an eigenvalue with multiplicity 4 and all tensors satisfying conditions from Equation 3.59 [Equation 3.60] are right [left] eigenvectors.

The other two right eigenvectors are in the form

$$\omega_1 \mathbf{I} + \omega_2 \text{dev } \mathbf{A}, \quad (3.61)$$

and can be found by solving the eigenvalue problem

$$\mathbb{C}[\omega_1 \mathbf{I} + \omega_2 \text{dev } \mathbf{A}] = \Lambda (\omega_1 \mathbf{I} + \omega_2 \text{dev } \mathbf{A}), \quad (3.62)$$

which leads to the following linear system

$$\begin{cases} \left(3a + \frac{\operatorname{tr} \mathbf{A} \operatorname{tr} \mathbf{B}}{3} + b - \Lambda \right) \omega_1 + \frac{\operatorname{tr} \mathbf{A}}{3} (\operatorname{dev} \mathbf{A} \cdot \operatorname{dev} \mathbf{B}) \omega_2 = 0, \\ 3 \frac{\operatorname{tr} \mathbf{B}}{3} \omega_1 + (b + \operatorname{dev} \mathbf{A} \cdot \operatorname{dev} \mathbf{B} - \Lambda) \omega_2 = 0. \end{cases} \quad (3.63)$$

Introducing the notation

$$\Delta = \sqrt{(\mathbf{A} \cdot \mathbf{B} - 3a)^2 + 4a \operatorname{tr} \mathbf{A} \operatorname{tr} \mathbf{B}}. \quad (3.64)$$

Nontrivial solutions of the system in Equation 3.63 are given by

$$\Lambda_{5,6} = \frac{3a + 2b + \mathbf{A} \cdot \mathbf{B} \pm \Delta}{2}, \quad (3.65)$$

with the corresponding right eigenvectors

$$\begin{aligned} \mathbf{R}^{(5),(6)} = & \frac{3(\mathbf{A} \cdot \mathbf{B} \mp \Delta + 3a)}{2 \operatorname{dev} \mathbf{A} \cdot \operatorname{dev} \mathbf{B}} \mathbf{I} + \\ & \frac{3(3\mathbf{A} \cdot \mathbf{B} \pm 3\Delta - 9a - 2 \operatorname{tr} \mathbf{A} \operatorname{tr} \mathbf{B})}{2 \operatorname{tr} \mathbf{A} (\operatorname{dev} \mathbf{A} \cdot \operatorname{dev} \mathbf{B})} \mathbf{A}, \end{aligned} \quad (3.66)$$

or, when $\operatorname{tr} \mathbf{A} (\operatorname{dev} \mathbf{A} \cdot \operatorname{dev} \mathbf{B}) = 0$, but $\operatorname{tr} \mathbf{B} \neq 0$, we have

$$\mathbf{R}^{(5),(6)} = \frac{3a - \mathbf{A} \cdot \mathbf{B} \pm \Delta}{2 \operatorname{tr} \mathbf{B}} \mathbf{I} + \mathbf{A}. \quad (3.67)$$

The two left eigenvectors corresponding to the eigenvalues from Equation 3.65 are in the form

$$\omega_1 \mathbf{I} + \omega_2 \operatorname{dev} \mathbf{B}, \quad (3.68)$$

so that by solving $\mathbb{C}^T[\omega_1 \mathbf{I} + \omega_2 \operatorname{dev} \mathbf{B}] = \Lambda (\omega_1 \mathbf{I} + \omega_2 \operatorname{dev} \mathbf{B})$, we find

$$\begin{aligned} \mathbf{L}^{(5),(6)} = & \frac{3(\mathbf{A} \cdot \mathbf{B} \mp \Delta + 3a)}{2 \operatorname{dev} \mathbf{A} \cdot \operatorname{dev} \mathbf{B}} \mathbf{I} + \\ & \frac{3(3\mathbf{A} \cdot \mathbf{B} \pm 3\Delta - 9a - 2 \operatorname{tr} \mathbf{A} \operatorname{tr} \mathbf{B})}{2 \operatorname{tr} \mathbf{B} (\operatorname{dev} \mathbf{A} \cdot \operatorname{dev} \mathbf{B})} \mathbf{B}, \end{aligned} \quad (3.69)$$

or, when $\operatorname{tr} \mathbf{B} (\operatorname{dev} \mathbf{A} \cdot \operatorname{dev} \mathbf{B}) = 0$, but $\operatorname{tr} \mathbf{A} \neq 0$, we have

$$\mathbf{L}^{(5),(6)} = \frac{3a - \mathbf{A} \cdot \mathbf{B} \pm \Delta}{2 \operatorname{tr} \mathbf{A}} \mathbf{I} + \mathbf{B}. \quad (3.70)$$

The case in which $\operatorname{tr} \mathbf{A} (\operatorname{dev} \mathbf{A} \cdot \operatorname{dev} \mathbf{B}) = \operatorname{tr} \mathbf{B} (\operatorname{dev} \mathbf{A} \cdot \operatorname{dev} \mathbf{B}) = 0$ is trivial.

Table 3.A.1: Eigensystem of the fourth-order tensor from Equation 3.49.

Eigenvalues	Multiplicity	Left eigenvectors	Right eigenvectors
b	4	$\forall \mathbf{L} \in \text{Sym} :$ $\text{tr } \mathbf{L} = 0,$ $\mathbf{L} \cdot \text{dev } \mathbf{A} = 0$	$\forall \mathbf{R} \in \text{Sym} :$ $\text{tr } \mathbf{R} = 0,$ $\mathbf{R} \cdot \text{dev } \mathbf{B} = 0$
$\Lambda_5 = \frac{3a + 2b + \mathbf{A} \cdot \mathbf{B} + \Delta}{2}$	1	$\mathbf{L}^{(5)}$	$\mathbf{R}^{(5)}$
$\Lambda_6 = \frac{3a + 2b + \mathbf{A} \cdot \mathbf{B} - \Delta}{2}$	1	$\mathbf{L}^{(6)}$	$\mathbf{R}^{(6)}$

In conclusion, we have found the spectral representation of the fourth-order tensor from Equation 3.49 without introducing any assumption on \mathbf{A} and \mathbf{B} , except their symmetry. This is summarized in Table 3.A.1, where the eigenvalues coincides with those derived in a different way by Bigoni and Zaccaria[5].

Finally, in the case when tensors \mathbf{A} and \mathbf{B} are coaxial, we can explicitly write the four eigenvectors corresponding to the eigenvalue b . To this purpose, we assume the spectral representation of \mathbf{A} and \mathbf{B} as

$$\mathbf{A} = \alpha_1 \mathbf{a}_1 \otimes \mathbf{a}_1 + \alpha_2 \mathbf{a}_2 \otimes \mathbf{a}_2 + \alpha_3 \mathbf{a}_3 \otimes \mathbf{a}_3, \quad (3.71)$$

$$\mathbf{B} = \beta_1 \mathbf{a}_1 \otimes \mathbf{a}_1 + \beta_2 \mathbf{a}_2 \otimes \mathbf{a}_2 + \beta_3 \mathbf{a}_3 \otimes \mathbf{a}_3, \quad (3.72)$$

so that the spectral representation of \mathbb{C} in the case of coaxial \mathbf{A} and \mathbf{B} is given by

$$\begin{aligned} \mathbb{C} = & b(\mathbf{R}^{(12)} \otimes \mathbf{L}^{(12)} + \mathbf{R}^{(13)} \otimes \mathbf{L}^{(13)} + \mathbf{R}^{(23)} \otimes \mathbf{L}^{(23)} + \tilde{\mathbf{R}} \otimes \tilde{\mathbf{L}}) \\ & + \Lambda_5 \mathbf{R}^{(5)} \otimes \mathbf{L}^{(5)} + \Lambda_6 \mathbf{R}^{(6)} \otimes \mathbf{L}^{(6)}, \end{aligned} \quad (3.73)$$

where

$$\mathbf{R}^{(12)} = \mathbf{L}^{(12)} = \frac{1}{\sqrt{2}}(\mathbf{a}_1 \otimes \mathbf{a}_2 + \mathbf{a}_2 \otimes \mathbf{a}_1), \quad (3.74)$$

$$\mathbf{R}^{(13)} = \mathbf{L}^{(13)} = \frac{1}{\sqrt{2}}(\mathbf{a}_1 \otimes \mathbf{a}_3 + \mathbf{a}_3 \otimes \mathbf{a}_1), \quad (3.75)$$

$$\mathbf{R}^{(23)} = \mathbf{L}^{(23)} = \frac{1}{\sqrt{2}}(\mathbf{a}_2 \otimes \mathbf{a}_3 + \mathbf{a}_3 \otimes \mathbf{a}_2), \quad (3.76)$$

$$\tilde{\mathbf{R}} = \frac{(\beta_2 - \beta_3)\mathbf{a}_1 \otimes \mathbf{a}_1 + (\beta_3 - \beta_1)\mathbf{a}_2 \otimes \mathbf{a}_2 + (\beta_1 - \beta_2)\mathbf{a}_3 \otimes \mathbf{a}_3}{\sqrt{\text{dev } \mathbf{A} \cdot \text{dev } \mathbf{B}}}, \quad (3.77)$$

3. Constitutive Modeling of the Cold-Forming of Ceramic Powders

$$\tilde{\mathbf{L}} = \frac{(\alpha_2 - \alpha_3)\mathbf{a}_1 \otimes \mathbf{a}_1 + (\alpha_3 - \alpha_1)\mathbf{a}_2 \otimes \mathbf{a}_2 + (\alpha_1 - \alpha_2)\mathbf{a}_3 \otimes \mathbf{a}_3}{\sqrt{\text{dev } \mathbf{A} \cdot \text{dev } \mathbf{B}}}. \quad (3.78)$$

3.B Yield Function Gradient and Derivatives

The yield function gradient \mathbf{Q} , from Equation 3.45, is given by

$$\mathbf{Q} = \frac{\partial F}{\partial \boldsymbol{\sigma}} = a(p) \mathbf{I} + b(\theta) \tilde{\mathbf{S}} + c(\theta) \tilde{\mathbf{S}}^\perp, \quad (3.79)$$

where

$$\tilde{\mathbf{S}} = \sqrt{\frac{3}{2}} \frac{\text{dev } \boldsymbol{\sigma}}{q}, \quad (3.80)$$

$$\tilde{\mathbf{S}}^\perp = -\frac{\sqrt{2}}{\sqrt{3}q} \frac{\partial \theta}{\partial \boldsymbol{\sigma}} = \frac{1}{\sin 3\theta} \left[\sqrt{6} \left(\tilde{\mathbf{S}}^2 - \frac{1}{3} \mathbf{I} \right) - \cos 3\theta \tilde{\mathbf{S}} \right], \quad (3.81)$$

and

$$\begin{aligned} a(p) &= -\frac{1}{3} \frac{\partial f(p)}{\partial p} \\ &= \frac{Mp_c}{3(p_c + c)} \frac{(1 - m\Phi^{m-1}) [2(1 - \alpha)\Phi + \alpha] + 2(1 - \alpha)(\Phi - \Phi^m)}{2\sqrt{(\Phi - \Phi^m)[2(1 - \alpha)\Phi + \alpha]}}, \\ b(\theta) &= \sqrt{\frac{3}{2}} \frac{1}{g(\theta)}, \\ c(\theta) &= -\frac{\sqrt{3}\gamma \sin 3\theta}{\sqrt{2}\sqrt{1 - \gamma^2 \cos^2 3\theta}} \sin \left[\beta \frac{\pi}{6} - \frac{1}{3} \cos^{-1}(\gamma \cos 3\theta) \right]. \end{aligned} \quad (3.82)$$

The derivatives of the yield function with respect to the yield function parameters are given by

$$\frac{\partial F}{\partial p_c} = -\frac{\eta p_c}{p_c + c} \left[\frac{(\Phi - \Phi^m)2(1 - \alpha) + (2(1 - \alpha)\Phi + \alpha)(1 - m\Phi^{m-1})}{2\sqrt{(\Phi - \Phi^m)(2(1 - \alpha)\Phi + \alpha)}} - \eta \sqrt{(\Phi - \Phi^m)(2(1 - \alpha)\Phi + \alpha)} \right] \quad (3.83)$$

$$\frac{\partial F}{\partial c} = -\frac{\eta p_c(1 - \Phi)}{p_c + c} \frac{(\Phi - \Phi^m)2(1 - \alpha) + (2(1 - \alpha)\Phi + \alpha)(1 - m\Phi^{m-1})}{2\sqrt{(\Phi - \Phi^m)(2(1 - \alpha)\Phi + \alpha)}} \quad (3.84)$$

$$\frac{\partial F}{\partial \eta} = -p_c \sqrt{(\Phi - \Phi^m)(2(1 - \alpha)\Phi + \alpha)} \quad (3.85)$$

$$\frac{\partial F}{\partial m} = \eta p_c \frac{(2(1 - \alpha)\Phi + \alpha)\Phi^m \ln(\Phi)}{2\sqrt{(\Phi - \Phi^m)(2(1 - \alpha)\Phi + \alpha)}} \quad (3.86)$$

$$\frac{\partial F}{\partial \alpha} = -\frac{\eta p_c (1 - 2\Phi)(\Phi - \Phi^m)}{2\sqrt{(\Phi - \Phi^m)(2(1 - \alpha)\Phi + \alpha)}} \quad (3.87)$$

$$\frac{\partial F}{\partial \beta} = -\frac{q\pi}{6} \sin\left(\beta\frac{\pi}{6} - \frac{\cos^{-1}(\gamma \cos(3\theta))}{3}\right) \quad (3.88)$$

$$\frac{\partial F}{\partial \gamma} = -\frac{q \cos(3\theta) \sin\left(\beta\frac{\pi}{6} - \frac{\cos^{-1}(\gamma \cos(3\theta))}{3}\right)}{3\sqrt{1 - \gamma^2 \cos^2(3\theta)}}. \quad (3.89)$$

3.C BP Yield Surface Analysis

The numerical implementation of the elastoplastic model *Tridentum* requires several different search algorithms for things such as the increment in volumetric plastic strain during hardening or simply the convergence criterion for the return algorithm. These problems can be aided greatly by an in-depth understanding of the yield surface and its behavior under certain assumptions. Because the behavior of the yield surface is desired, the actual formulation of the yield function is arbitrary, so long as the zero isosurface is unchanged.

To start the analysis, Equation 3.20 is further decomposed into

$$f(p) = -\eta p_c C(\Phi) = -\eta p_c \sqrt{A(\Phi)B(\Phi)} \quad (3.90)$$

where $A(\Phi)$ (Equation 3.92) is the asymmetrical pressure-dependence term and $B(\Phi)$ (Equation 3.102) is the cap shape term, and $C(\Phi)$ is the total meridional shape term. Another constituent equation that deserves individual attention is $g(\theta_c)$, which controls the Lode angle dependence of the yield surface.

As the yield function is defined as the zero-isosurface of the function given in Equation 3.19. Therefore, that equation can be rewritten, solving for q as a function of θ_c and p

$$q = -g(\theta_c)f(p) \quad (3.91)$$

which represents the yield surface, not the yield function.

Function	Minimum	Maximum
$2(1 - \alpha)\Phi + \alpha$	0*	2*
$\Phi - \Phi^m$	0	1*
$g(\theta_c)$	1	2*

Table 3.C.1: A table of absolute maximum and minimum values for the constituent functions of the BP yield surface. This table takes into account all possible parameter values and combinations. Values with a * denote an exclusive interval endpoint.

3.C.1 Asymmetrical Pressure-Dependence Term

One of the two terms in $f(p)$ as defined in Equation 3.90 is the asymmetrical pressure-dependent term which is defined as

$$A(\Phi) = \Phi - \Phi^m. \quad (3.92)$$

3. Constitutive Modeling of the Cold-Forming of Ceramic Powders

Function	Minimum	Maximum
$2(1 - \alpha)\Phi + \alpha$	$1 - \alpha - 1 ^*$	$1 + \alpha - 1 ^*$
$\Phi - \Phi^m$	0	$\left(\frac{1}{m}\right)^{\frac{1}{m-1}} - \left(\frac{1}{m}\right)^{\frac{m}{m-1}}$
$g(\theta_c)$	1^{**}	$\frac{1}{\cos\left(\frac{1}{3} \max(\beta\frac{\pi}{2} - \pi + \cos^{-1}\gamma , \beta\frac{\pi}{2} - \cos^{-1}\gamma)\right)}$

Table 3.C.2: A table of bounded maximum and minimum values for the constituent functions of the BP yield surface. This table takes into account all possible parameter values and combinations and attempts to give better bounds than in Table 3.C.1. *Exclusive interval endpoint. **This minimum for $g(\theta_c)$ is not a tight bound (see Equation 3.127).

This is defined over the same domain as $\Phi \in [0, 1]$ and is only subject to the single user input m which is defined over the left-bounded interval $(1, \infty)$. The constraint that $m \neq 1$ is required so that $A(\Phi) \neq 0 \forall \Phi \in (0, 1)$. A plot of the function for various values of m can be found in Figure 3.C.1.

The minimum of this function over the domain of Φ is zero. This minimum has a multiplicity of two, where $\Phi = 0, 1$.

The value of Φ at the maximum of $A(\Phi)$ can be found by taking the derivative of $A(\Phi)$ with respect to Φ and then finding the zero within the domain of Φ . The derivative is

$$\frac{dA(\Phi)}{d\Phi} = 0 = 1 - m\Phi^{m-1} \quad (3.93)$$

and the zero point is at

$$\Phi_{\max} = \left(\frac{1}{m}\right)^{\frac{1}{m-1}}. \quad (3.94)$$

The value of $A(\phi_{\max})$ is found by

$$\max A(\Phi) = \left(\frac{1}{m}\right)^{\frac{1}{m-1}} - \left(\frac{1}{m}\right)^{\frac{m}{m-1}}. \quad (3.95)$$

To verify these equations it will be demonstrated that for $m = 2$ the function is even symmetric about $\Phi = 1/2$ with a maximum of $1/4$. We can put $A(\Phi)$ into the classical quadratic form with easily identifiable coefficients

$$A(\Phi) = \Phi - \Phi^2 = -1\Phi^2 + 1\Phi + 0 \quad (3.96)$$

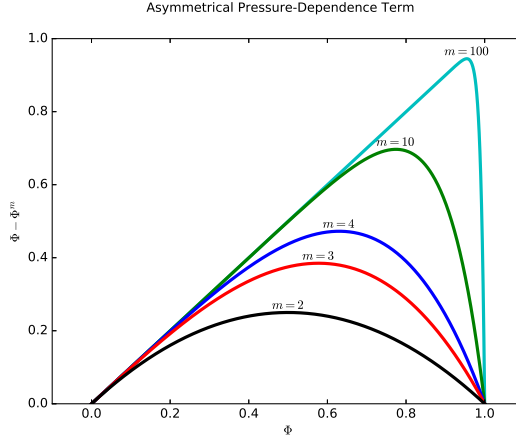


Figure 3.C.1: A plot of the asymmetrical pressure-dependence term from the meridional function of the yield surface.

Because the function can be represented by a quadratic polynomial it is even-symmetric. Using the well-known identity that, for a quadratic equation of the form $ax^2 + bx + c$, the vertex coordinates (h, k) are found by

$$(h, k) = \left(-\frac{b}{2a}, \frac{4ac - b^2}{4a} \right) = \left(-\frac{1}{2(-1)}, \frac{4(-1)0 - 1^2}{4(-1)} \right) = \left(\frac{1}{2}, \frac{1}{4} \right) \quad (3.97)$$

and represent the location of the maximum point of $A(\Phi)$.

These results can be easily verified to be the location and value of the maximum found using the general solution. First, the abscissa of the maximum from Equation 3.94

$$\Phi_{\max} = \left(\frac{1}{2} \right)^{\frac{1}{2-1}} = \frac{1}{2} \quad (3.98)$$

then the ordinate of the maximum

$$\max A(\Phi) = \left(\frac{1}{2} \right)^{\frac{1}{2-1}} - \left(\frac{1}{2} \right)^{\frac{2}{2-1}} = \frac{1}{2} - \frac{1}{2^2} = \frac{1}{4} \quad (3.99)$$

which completes the check.

It is interesting to note that as $m \rightarrow 0$ or $m \rightarrow \infty$ the function $A(\Phi)$ degenerates to very simple linear equations. For the former, $A(\Phi) = 0$ and the latter becomes one cycle of the sawtooth function with a maximum value of unity at $\Phi = 1$. Also, when $m \rightarrow 1$ the

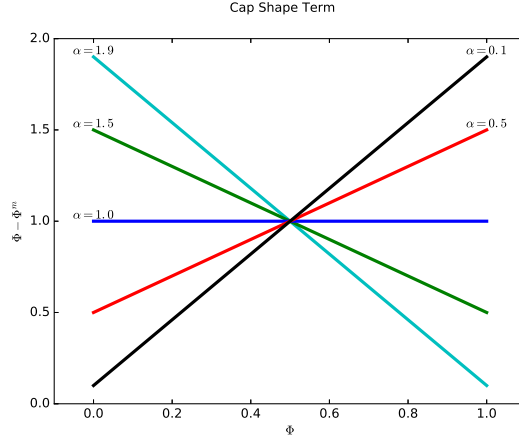


Figure 3.C.2: A plot of the cap shape term from the meridional function of the yield surface. Note that at $\Phi = 1/2$ the function is always equal to unity for all values of α .

maximum value of $A(\Phi)$ is found at $\Phi = 1/e$ with a corresponding maximum value of

$$\lim_{m \rightarrow 1} A(\Phi) = 0 \quad \text{maximum at} \quad \Phi = \frac{1}{e}. \quad (3.100)$$

The maximum value and location for $m \rightarrow \infty$ is

$$\lim_{m \rightarrow \infty} A(\Phi) = \Phi \quad \text{maximum at} \quad \Phi = 1. \quad (3.101)$$

Thus, it is shown that the maximum point will always be $\Phi_{\max} \in (1/e, 1)$, for all valid values for the parameter m .

3.C.2 Cap Shape Term

This function controls how flattened or pointed the tensile and compressive limits are. The second term in $f(p)$ from Equation 3.90 is

$$B(\Phi) = 2(1 - \alpha)\Phi + \alpha. \quad (3.102)$$

This function is unambiguously a simple linear function in slope-intercept form. The function evaluates to unity when $\Phi = 1/2 \forall \alpha \in (0, 2)$. A plot of $B(\Phi)$ for various values of α can be found in Figure 3.C.2.

Because the function is linear the minimum and maximum are located at the extremes of the domain of Φ . To determine the maximum and minimum values we only need to use the mathematical form of the MAX and MIN functions as used in programming languages

$$\text{MAX}(a, b) = \frac{a + b}{2} + \frac{|a - b|}{2}, \quad (3.103)$$

$$\text{MIN}(a, b) = \frac{a + b}{2} - \frac{|a - b|}{2}. \quad (3.104)$$

These forms assist in computations as no branch point is required during evaluation. Applying these identities with $a = B(0) = \alpha$ and $b = B(1) = 2 - \alpha$

$$\max B(\Phi) = \frac{\alpha + (2 - \alpha)}{2} + \frac{|\alpha - (2 - \alpha)|}{2} = 1 + |\alpha - 1| \quad (3.105)$$

$$\min B(\Phi) = \frac{\alpha + (2 - \alpha)}{2} - \frac{|\alpha - (2 - \alpha)|}{2} = 1 - |\alpha - 1| \quad (3.106)$$

Note that the range of the function $B(\Phi)$ is $(0, 2)$ for the domain on which Φ is defined $[0, 1]$.

Total Meridional Shape Term

Combining the functions from Section 3.C.1 and Section 3.C.2 it is possible to analyze the unscaled form of the meridional profile of the yield surface. The unscaled form is given by

$$C(\Phi) = \sqrt{A(\Phi)B(\Phi)} = \sqrt{(\Phi - \Phi^m)[2(1 - \alpha)\Phi + \alpha]} \quad (3.107)$$

and is only defined on the domain of $\Phi \in [0, 1]$. This function differs from the actual yield surface in p - q space only by scalar multiples in both directions and a shift along the abscissa. As was found in Section 3.C.1 and Section 3.C.2 the only zeros of the arguments of the square root are at $\Phi = 0, 1$ and so the only zeros of $C(\Phi)$ are also at $\Phi = 0, 1$.

In order to find the coordinates of the maximum of this function, it is necessary to take the derivative with respect to Φ and solve for Φ when the derivative equals zero. The derivative is given by

$$\frac{dC(\Phi)}{d\Phi} = \frac{(2(1 - \alpha)\Phi + \alpha)(1 - m\Phi^{m-1}) + (\Phi - \Phi^m)2(1 - \alpha)}{2\sqrt{(\Phi - \Phi^m)[2(1 - \alpha)\Phi + \alpha]}}. \quad (3.108)$$

Notice that the denominator only has zeros at $\Phi = 0, 1$, causing $dC/d\Phi = +\infty, -\infty$ respectively at those points. Therefore, to determine the Φ -location of the maximum value of $C(\Phi)$ it is sufficient to set the numerator equal to zero and solve. However, the expanded numerator of the above equation yields a polynomial of the form $a\Phi^m + b\Phi^{m-1} + c\Phi + d$ which cannot be solved in a general manner but can be solved for particular values of m or α . Specifically, it can be solved when $m = 2$ or $m = 3$ where the numerator degenerates to a quadratic or cubic function, respectively, or when $\alpha = 1$ or $\alpha \rightarrow 0$. There may be other instances where the function can be analyzed analytically but these cases are too pathological to be treated here.

From Section 3.C.1 and Section 3.C.2 enough information exists to bound the total meridional shape function. Using the triangle inequality

$$\max C(\Phi) = \max \sqrt{A(\Phi)B(\Phi)} \leq \sqrt{(\max A(\Phi))(\max B(\Phi))} \quad (3.109)$$

$$\max C(\Phi) \leq \sqrt{\left[\left(\frac{1}{m} \right)^{\frac{1}{m-1}} - \left(\frac{1}{m} \right)^{\frac{m}{m-1}} \right] [1 + |\alpha - 1|]} < \sqrt{2} \quad (3.110)$$

The maximum value is strictly less than $\sqrt{2}$ because of the interval over which α is defined $0 < \alpha < 2$. This upper bound is useful for the implementation of iterative return methods that must be sufficiently close to the yield surface in order to converge. While the upper bound of $\sqrt{2}$ is generally sufficient to determine a characteristic length for use as a convergence tolerance, it may be orders of magnitude larger than the actual maximum. This is due to $\max C(\Phi) \rightarrow 0$ as $m \rightarrow \infty$.

Notwithstanding the utility of this upper bound, there exist tighter bounds for all instances where $\alpha \neq 1$ because the maxima of $A(\Phi)$ and $B(\Phi)$ are only coincident for $\alpha = 1$. Figure 3.C.3 contains plots depicting $C(\Phi)$ for various values of m and α along with the upper bound from Equation 3.110 for each realization. Also, in Figure 3.C.5 it is easily discernible that the bound is less accurate for $\alpha = 2$ as m increases but the bound, for the common range of parameters, will not be more than roughly double the actual maximum even if the true maximum is much less than $\sqrt{2}$.

Total Meridional Shape Term when $\alpha = 1$

When $\alpha = 1$, the function $C(\Phi)$ in Equation 3.107 simplifies considerably to

$$C(\Phi) = \sqrt{\Phi - \Phi^m}, \quad (3.111)$$

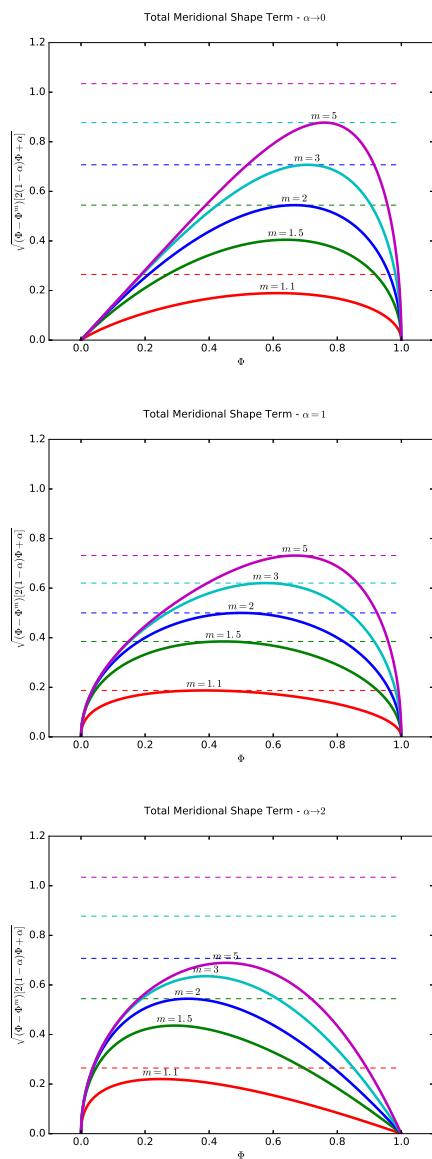


Figure 3.C.3: Plots of the total meridional shape term for various values of m and α . Notice that, for $\alpha = 1$ the upper bounds are exact.

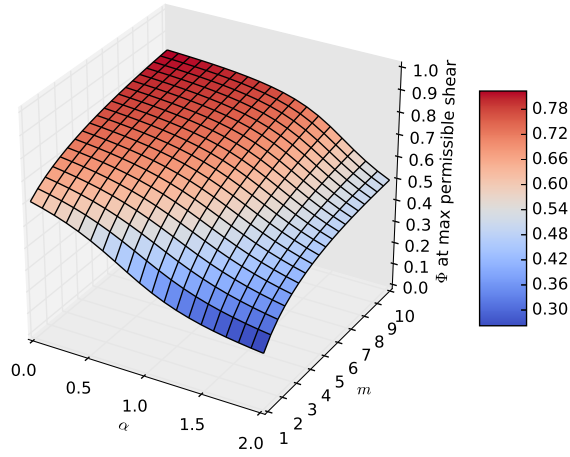


Figure 3.C.4: A 3D plot depicting the Φ -location of the maximum permissible shear for given values of α and m . Not surprisingly, the ϕ value at maximum approaches unity as m increases.

and the derivative with respect to Φ simplifies to

$$\frac{dC(\Phi)}{d\Phi} = \frac{1 - m\Phi^{m-1}}{2\sqrt{\Phi - \Phi^m}}. \quad (3.112)$$

From this it is possible to find that the maximum value of $C(\Phi)$ is located at

$$\Phi_{\max} = \left(\frac{1}{m}\right)^{\frac{1}{m-1}} \quad \text{where} \quad \Phi_{\max} \in \left(\frac{1}{e}, 1\right) \forall m \in (1, \infty) \quad (3.113)$$

in the same manner as in Equation 3.94.

Total Meridional Shape Term when $\alpha \rightarrow 0$

When $\alpha \rightarrow 0$, the function $C(\Phi)$ in Equation 3.107 simplifies to

$$C(\Phi) = \sqrt{2\Phi(\Phi - \Phi^m)}, \quad (3.114)$$

and the derivative with respect to Φ simplifies to

$$\frac{dC(\Phi)}{d\Phi} = \frac{2\Phi - (m+1)\Phi^m}{\sqrt{2(\Phi^2 - \Phi^{m+1})}}. \quad (3.115)$$

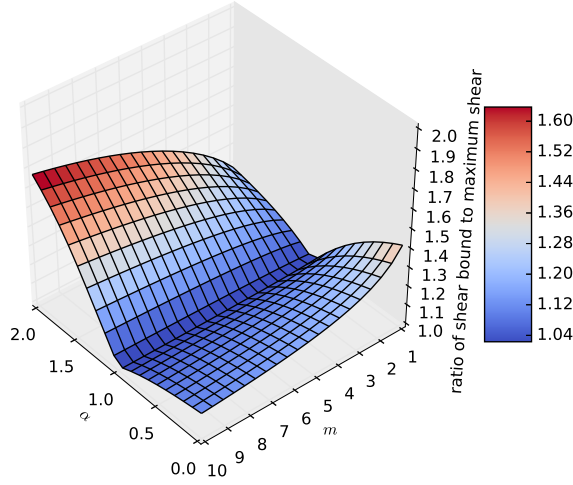


Figure 3.C.5: A 3D plot depicting the ratio of the upper bound of the maximum permissible shear (Equation 3.110) divided by the actual maximum permissible shear for common ranges of α and m .

Because the roots of the denominator are $\Phi = 0, 0, 1$ only the numerator needs be considered for determining where the maximum is located. From the numerator, the maximum value of $C(\Phi)$ is located at

$$\Phi_{\max} = \left(\frac{2}{m+1} \right)^{\frac{1}{m-1}} \quad \text{where} \quad \Phi_{\max} \in \left(\frac{1}{\sqrt{e}}, 1 \right) \quad \forall m \in (1, \infty). \quad (3.116)$$

It is insightful to compare the domain of Φ_{\max} for $\alpha = 1$ and $\alpha \rightarrow 0$.

Total Meridional Shape Term when $\alpha \rightarrow 2$

When $\alpha \rightarrow 2$, the ability to solve the general problem for all values of m is lost. This is due to the fact that the equation becomes a polynomial of arbitrary order. Generally, equations of this nature are not solvable analytically and, as such, will not be treated here.

Total Meridional Shape Term when $m = 2$

When $m = 2$, the total meridional shape function $C(\Phi)$ simplifies to

$$C(\Phi) = \sqrt{(\Phi - \Phi^2)[2(1 - \alpha)\Phi + \alpha]}, \quad (3.117)$$

which happens to be a cubic function in Φ under the radical. The derivative is given by

$$\frac{dC(\Phi)}{d\Phi} = \frac{(6\alpha - 6)\Phi^2 + (4 - 6\alpha)\Phi + \alpha}{2\sqrt{(\Phi - \Phi^2)[2(1 - \alpha)\Phi + \alpha]}}. \quad (3.118)$$

As before, the denominator of the derivative only has zeros in the domain of interest at $\Phi = 0, 1$ so finding zeros in the numerator is sufficient.

For this we may use the standard formula for the roots of a quadratic equation

$$\Phi = \frac{-(4 - 6\alpha) \pm \sqrt{(4 - 6\alpha)^2 - 4(6\alpha - 6)\alpha}}{2(6\alpha - 6)} \quad (3.119)$$

There are two issues with this equation. The first is that the denominator is equal to zero when $\alpha = 1$. The second is that the discriminant in the radical could possibly be negative, giving us complex roots.

To address the second issue first, we can expand the discriminant into standard polynomial notation to find

$$f(\alpha) = (4 - 6\alpha)^2 - 4(6\alpha - 6)\alpha = 12\alpha^2 - 24\alpha + 16 \quad (3.120)$$

which has a positive coefficient on the α^2 term, so we know that it is concave-up. Using the same identity that was used in Equation 3.97, the vertex of the parabola is found to be located at $\alpha = 1$, where $f(1) = 4$. Knowing that the parabola is concave-up and that the vertex is positive, it is proven that $f(\alpha) > 0 \forall \alpha$ and that the discriminant is strictly positive.

The first issue can be addressed by imposing the constraint that the desired root given by Equation 3.119 must give reasonable values of Φ near $\alpha = 1$. Taking the limit of Equation 3.119

$$\lim_{\alpha \rightarrow 1} \frac{-(4 - 6\alpha) \pm \sqrt{(4 - 6\alpha)^2 - 4(6\alpha - 6)\alpha}}{2(6\alpha - 6)} = \frac{2 \pm 2}{2(6 - 6)} \quad (3.121)$$

In the positive branch of the above equation the roots are asymptotic towards infinity as $\alpha \rightarrow 1$ whereas in the negative branch the limit converges to $1/2$. Because of the smooth, continuous behavior of

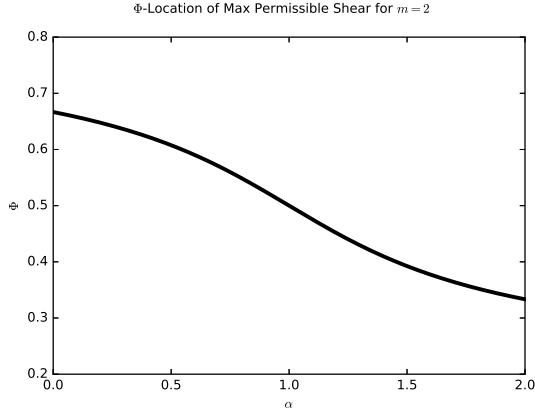


Figure 3.C.6: A plot depicting the Φ -location of the maximum permissible shear over the entire domain of α of the total meridional shape term for $m = 2$.

the negative branch, it is deemed the valid root for the maximum of Equation 3.117. Further analysis of this equation demonstrates that, for $m = 2$, the maximum allowable shear will occur somewhere on the domain of $\Phi \in (1/3, 2/3)$ (see Figure 3.C.6).

Octahedral Shape Term

Here the function $g(\theta_c)$ is analyzed, which is defined by

$$g(\theta_c) = \frac{1}{\cos\left(\beta\frac{\pi}{6} - \frac{\cos^{-1}(\gamma\cos(3\theta_c))}{3}\right)}. \quad (3.122)$$

First off, it is desirable to get the global maximum and minimum values for the function for all values of β and γ . It is given that $\beta \in [0, 2]$, $\gamma \in [0, 1)$, $\theta_c \in (-\infty, \infty)$, and, therefore, $\cos(3\theta_c) \in [-1, 1]$. From this, it can be inferred that the argument of the outer-most cosine exists on $(-\pi/3, \pi/3)$ which entails that $g(\theta_c) \in [1, 2)$.

These bounds can be improved upon given specific values of β or γ . For example, when $\gamma = 0$ the it is trivial to show that the function domain is $[1, 2/\sqrt{3}]$ for all acceptable values of β . It is slightly more difficult to show that when $\gamma = 1$ the function domain is $[1, 2]$ for all acceptable values of β .

While the argument of the outer-most cosine function might not be able to be equal to zero, it can be solved to determine what values

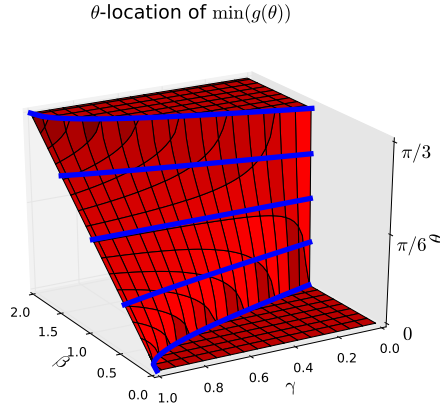


Figure 3.C.7: A plot depicting the θ_c -location of the minimum of $g(\theta_c)$ for various values of β and γ . The black grid shows the contours for constant β or γ . The blue lines depict the contours of constant θ_c . The lower plateau is at $\theta_c = 0$ which is triaxial extension, while the upper plateau is at $\theta_c = \pi/3$ which is triaxial compression.

of β and γ allow the globally-minimum value of $g(\theta_c)$ to be accessed

$$\beta \frac{\pi}{6} - \frac{\cos^{-1}(\gamma \cos(3\theta))}{3} = 0 \quad (3.123)$$

$$\theta = \frac{\cos^{-1}\left(\frac{\cos(\beta\pi/2)}{\gamma}\right)}{3}. \quad (3.124)$$

The observant reader will readily notice that, for increasingly smaller values of γ , the inverse cosine becomes undefined. This equation is only valid when $-\gamma \leq \cos(\beta\pi/2) \leq \gamma$, which is the relation that must hold for $g(\theta_c)$ to equal unit for a given β and γ . Outside of this range the inverse cosine is undefined because the minimum of $g(\theta_c)$ does not reach zero. In Figure 3.C.7 the above equation is visualized.

The θ_c location of the minimum value of $g(\theta_c)$ is known for subset of the range of possible inputs. The general solution is presented with the assistance of three helper variables

$$G_1 = \beta \frac{\pi}{2} - \pi + \cos^{-1} \gamma \quad (3.125)$$

$$G_2 = \beta \frac{\pi}{2} - \cos^{-1} \gamma. \quad (3.126)$$

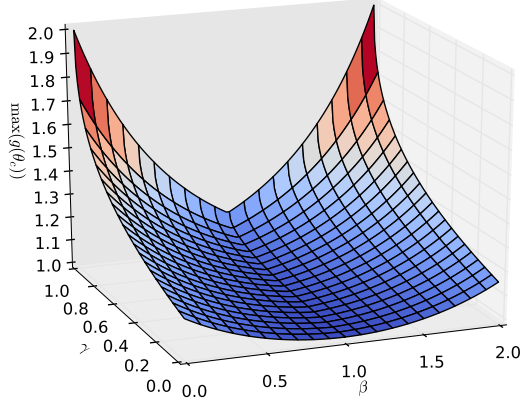


Figure 3.C.8: A plot of $\max(g(\theta_c))$ for all allowable values of γ and β . Note the symmetry around the $\beta = 1$ line.

Using these helper values, the minimum value of $g(\theta_c)$ can be succinctly defined by

$$\min(g(\theta_c)) = \begin{cases} 1 & \text{sign}(G_1) \neq \text{sign}(G_2) \\ \frac{1}{\cos(\frac{1}{3} \min(|G_1|, |G_2|))} & \text{otherwise} \end{cases}. \quad (3.127)$$

The maximum value of $g(\theta_c)$ is very similar to equation 3.127 and makes use of the helper values from Equation 3.125

$$\max(g(\theta_c)) = \frac{1}{\cos(\frac{1}{3} \max(|G_1|, |G_2|))}. \quad (3.128)$$

In Figure 3.C.8 the function $\max(g(\theta_c))$ has been plotted for all valid values of β and γ . From the figure it is easy to see that when $\gamma \approx 1$ and either $\beta \approx 0$ or $\beta \approx 2$ the function $\max(g(\theta_c))$ is at the global maximum. When $\beta = 1$ the function has two maxima at triaxial compression and triaxial extension.

3.D Parameterization for Classical Plasticity Models

The Bigoni-Piccolroaz yield surface is very flexible and is capable of mimicking many more basic yield surfaces. Most of the basic yield surfaces are variations on one of two yield surfaces: an ellipsoid centered at the origin and a cone-like surface with the vertex in the tensile portion of the hydrostatic axis.

The ellipsoid can be parameterized with only two parameters: A and B , which are the pressure limit p_{int} and shear limit q_{int} , respectively. Both are positive. The parameterization is as follows

$$\begin{aligned}
 \beta &= 1 && \text{Ensure } g(\theta) = 1 \\
 \gamma &= 0 && \text{Ensure } g(\theta) = 1 \\
 m &= 2 && \text{Invokes pressure symmetry} \\
 \alpha &= 1 && \text{Invokes pressure symmetry} \\
 c &= p_{\text{int}} && \text{Some large number} \\
 p_c &= p_{\text{int}} && \text{Some large number} \\
 \eta &= \frac{2q_{\text{int}}}{p_c} && \text{Set radius of the yield surface}
 \end{aligned} \tag{3.129}$$

The cone-like yield surface is described by a vertex on the tensile hydrostatic axis with a constant slope from that point for a given Lode angle. The pressure at the vertex is denoted p_{int} . However, the slope is not necessarily constant for all Lode angles. The parameterization is as follows

$$\begin{aligned}
 m &= 100 && \text{Some large number} \\
 \alpha &= 0.0001 && \text{Some small number} \\
 c &= p_{\text{int}} && \text{Some large number} \\
 p_c &= 1000c && \text{Some large number}
 \end{aligned} \tag{3.130}$$

where the remaining parameters β , γ , and η can be found by the following relation

$$\text{slope} = \frac{r}{z} = \frac{2g(\theta_c)\eta p_c}{3(p_c + c)} \tag{3.131}$$

where the slope is in isomorphic stress space.

3.D.1 Sphere

While a spherical yield surface is not particularly useful for real-world materials, it is useful for model testing. With the limit magnitude of

the stress tensor defined by A , the parameterization is

$$\begin{aligned}
 \beta = 1 & \quad \text{Ensure } g(\theta) = 1 \\
 \gamma = 0 & \quad \text{Ensure } g(\theta) = 1 \\
 m = 2 & \quad \text{Invokes pressure symmetry} \\
 \alpha = 1 & \quad \text{Invokes pressure symmetry} \\
 c = \frac{A}{\sqrt{3}} & \quad \text{Tensile pressure limit} \\
 p_c = \frac{A}{\sqrt{3}} & \quad \text{Compressive pressure limit} \\
 \eta = 3\sqrt{2} & \quad \text{Set radius of the yield surface}
 \end{aligned} \tag{3.132}$$

3.D.2 Elasticity

The Bigoni-Piccolroaz yield surface can be parameterized to be set at numerical infinity (always elastic) by

$$\begin{aligned}
 \beta = 1 & \quad \text{Ensure } g(\theta) = 1 \\
 \gamma = 0 & \quad \text{Ensure } g(\theta) = 1 \\
 m = 2 & \quad \text{Invokes pressure symmetry} \\
 \alpha = 1 & \quad \text{Invokes pressure symmetry} \\
 c = 1000K & \quad \text{Some large number} \\
 p_c = c & \quad \text{Some large number} \\
 \eta = 1 & \quad \text{Set radius of the yield surface}
 \end{aligned} \tag{3.133}$$

where K is the bulk modulus of the material.

3.D.3 von Mises

Starting with the definition of the yield surface

$$F = \sqrt{J_2} - k \tag{3.134}$$

For this parameterization only one only needs Y_t or Y_s , the yield in tension and yield in shear, respectively, which are related to k by

$$k = Y_s = \frac{Y_t}{\sqrt{3}}. \tag{3.135}$$

The Bigoni-Piccolroaz yield surface can be parameterized by

$$\begin{aligned}
 \beta = 1 & && \text{Ensure } g(\theta) = 1 \\
 \gamma = 0 & && \text{Ensure } g(\theta) = 1 \\
 m = 2 & && \text{Invokes pressure symmetry} \\
 \alpha = 1 & && \text{Invokes pressure symmetry} \\
 c = 1000k & && \text{Some large number} \\
 p_c = c & && \text{Some large number, equal to } c \\
 \eta = \frac{2\sqrt{3}k}{p_c} & && \text{Set radius of the yield surface}
 \end{aligned} \tag{3.136}$$

3.D.4 Tresca

The yield function for the Tresca yield surface can be written

$$F = \sqrt{J_2} \cos \theta_s - k = \sqrt{J_2} \cos(\theta_c - \pi/2) - k \tag{3.137}$$

where the model is fully parametrized with only the yield in shear $k = Y_s$ being defined. The Bigoni-Piccolroaz yield surface can be parameterized by

$$\begin{aligned}
 \beta = 1 & && \text{Equal preference to TXC and TXE} \\
 \gamma = 0.999 & && \text{Approach unity} \\
 m = 2 & && \text{Invokes pressure symmetry} \\
 \alpha = 1 & && \text{Invokes pressure symmetry} \\
 c = 1000k & && \text{Some large number} \\
 p_c = c & && \text{Some large number, equal to } c \\
 \eta = \frac{2\sqrt{3}k}{p_c} & && \text{Set radius of the yield surface}
 \end{aligned} \tag{3.138}$$

3.D.5 Linear Drucker-Prager

Starting with the most simple definition of the linear Drucker-Prager yield surface

$$F = \sqrt{J_2} - A - BI_1, \tag{3.139}$$

the values for A and B can be found using $q_{\text{int}}, p_{\text{int}}$ or $r_{\text{int}}, z_{\text{int}}$ (the pure-shear and pure-pressure intercepts) as follows

$$A = \frac{q_{\text{int}}}{\sqrt{3}} = \frac{r_{\text{int}}}{\sqrt{2}} \tag{3.140}$$

$$B = \frac{q_{\text{int}}}{3\sqrt{3}p_{\text{int}}} = -\frac{r_{\text{int}}}{\sqrt{6}z_{\text{int}}}. \quad (3.141)$$

The Bigoni-Piccolroaz yield surface can be parameterized by

$$\begin{aligned} \beta &= 1 && \text{Ensure } g(\theta) = 1 \\ \gamma &= 0 && \text{Ensure } g(\theta) = 1 \\ m &= 100 && \text{Some large number} \\ \alpha &= 0.0001 && \text{Some small number} \\ c &= -\frac{A}{3B} && \text{tensile pressure limit} \\ p_c &= 100c && \text{Some large number} \\ \eta &= \frac{\sqrt{3}A(p_c + c)}{\sqrt{2}p_c c} && \text{Set the slope of the yield surface} \end{aligned} \quad (3.142)$$

3.D.6 Principal Stress Cutoff

The principal stress cutoff yield function is

$$F = \max(\sigma_1, \sigma_2, \sigma_3) - A \quad (3.143)$$

where σ_1 , σ_2 , and σ_3 are the unordered principal stresses. The only parameter required is A , which is the maximum principal stress allowable. The Bigoni-Piccolroaz yield surface can be parameterized by

$$\begin{aligned} \beta &= 0 && \text{Preference to TXC} \\ \gamma &= 0.999 && \text{Approach unity} \\ m &= 100 && \text{Some large number} \\ \alpha &= 0.0001 && \text{Some small number} \\ c &= A && \text{tensile pressure limit} \\ p_c &= 100c && \text{Some large number} \\ \eta &= \frac{3(p_c + c)}{2\sqrt{2}p_c} && \text{Set the slope of the yield surface} \end{aligned} \quad (3.144)$$

3.D.7 Mohr-Coulomb

The yield function for a Mohr-Coulomb yield surface is given by

$$F = (\sigma_{\max} - \sigma_{\min}) + (\sigma_{\max} + \sigma_{\min}) \sin B - 2A \cos B \quad (3.145)$$

where the user inputs are A and B , traditionally called c and ϕ , respectively. The symbols A and B were chosen to alleviate confusion

with the BP yield surface parameters. The Bigoni-Piccolroaz yield surface can be parameterized by

$$\begin{aligned}
 \beta &= \sqrt{3} \left(\frac{4}{3 + \sin(B)} - 1 \right) && \text{Deviatoric cross section} \\
 \gamma &= 0.999 && \text{Approach unity} \\
 m &= 100 && \text{Some large number} \\
 \alpha &= 0.0001 && \text{Some small number} \\
 c &= \frac{A}{\tan B} && \text{tensile pressure limit} \\
 p_c &= 100c && \text{Some large number} \\
 \eta &= 3\sqrt{2} \cos\left(\beta \frac{\pi}{6}\right) \frac{\sin B}{3 + \sin B} && \text{Deviatoric cross section}
 \end{aligned} \tag{3.146}$$

3.D.8 Gurson

The Gurson yield surface for spherical voids and fully plastic flow, to the first order, is given in[36] as

$$T_{\text{eqv}}^2 + 2f \cosh\left(\frac{T_{nn}}{2}\right) - 1 - f^2 = 0, \tag{3.147}$$

where $T = \sigma/Y_t$ and Y_t is the yield in tension of the matrix material (assuming a von Mises matrix). So, it can be rewritten in more standard form

$$\frac{q^2}{Y_t^2} + 2f \cosh\left(\frac{3p}{2Y_t}\right) - 1 - f^2 = 0 \tag{3.148}$$

where q is the equivalent shear and p is the hydrostatic pressure. Because $\cosh()$ is a symmetric function, the sign of the argument is arbitrary. To mimick the first-order Gurson yield surface, it is necessary to first substitute the first-order Taylor expansion of $\cosh()$ and rearrange to get

$$q^2 = 1 + f^2 - 2f \left(1 + \frac{1}{2} \left(\frac{3p}{2Y_t}\right)^2\right), \tag{3.149}$$

which is, in fact, an ellipse in $p - q$ space or any linearly-transformed space (such as $z - r$ space) with the intersects on the p -axis and q -axis given by a and b respectively,

$$a = \frac{2b}{3\sqrt{f}} \quad b = Y_t(1 - f). \tag{3.150}$$

This gives the parameterization

$$\begin{aligned}
 \beta &= 1 && \text{Ensure } g(\theta) = 1 \\
 \gamma &= 0 && \text{Ensure } g(\theta) = 1 \\
 m &= 2 && \text{Some large number} \\
 \alpha &= 1 && \text{Some small number} \\
 c = a = \frac{2b}{3\sqrt{f}} = \frac{2Y_t(1-f)}{3\sqrt{f}} &&& \text{tensile pressure limit} \\
 p_c = c &&& \text{compressive pressure limit} \\
 \eta = 3\sqrt{f} &&& \text{Set the shear limit}
 \end{aligned} \tag{3.151}$$

Parameterizing Tridentum for Alumina Powder KMS-96

*The purpose of this document is to outline the suggested method for parameterizing the material model **Tridentum**. The model is complex with 30 parameters that span the powder phase and condensed phase and that govern the behavior during the transition. As it is with most complex material models, it is very difficult to develop tests from which single parameters can be directly measured, let alone find the equipment and funding to perform all the required tests that the theory requires. This document is a guide for parameterizing the model using simple experiments to determine reasonable starting values and then applying inverse analysis to improve those values. The material used for the the parameterization herein is Martoxid KMS-96 alumina powder from Albemarle. The powder is 96% aluminum oxide with a bulk density of 1200kg/m^3 and a green density of 2400kg/m^3 at 100MPa.*

4.1 Experiments

As **Tridentum** has nearly 30 user inputs, the topic of parameterization is a challenging one. Ideally, there would be a unique test for every parameter or set of parameters, where each parameter could be exactly measured from the experimental data. With the exception of very simple models, this is usually not plausible due to the complex interplay between effects which are dependent on the changing material state and may be path dependent.

This chapter covers how to parameterize **Tridentum** using relatively simple experimental data, information from the literature, and assumptions to fill in the gaps. This is included as a guide to help parameterize the model, but could be extended by adding tests beyond those described. When data are not available or there is conflicting data or the parameter is not directly measurable, the technique of inverse analysis can be applied to get reasonable, but not necessarily correct, values for the parameterization.

The material being parameterized is an alumina powder, produced by Albemarle, called Martoxid KMS-96. From the datasheet produced by the company[1], it is 96% Al_2O_3 with a bulk density of 1200kg/m^3 , a median granule size of $170\mu\text{m}$, and a moisture content of $\leq 0.3\%$. The reported green density at 100MPa is 2400kg/m^3 , a doubling of the bulk density, with a theoretical upper bound of 3970kg/m^3 (the density of solid aluminum oxide)[43].

4.1.1 Uniaxial Strain - Disk Forming

The most simple experimental data obtainable for parameterizing *Tridentum* are disk forming experiments.

The mold used to create the disks is a cylindrical, single-action die made of steel with a 30mm-diameter. The mold also has a removable base and plunger, both made of steel, which allow for easy removal of the formed disk by removing the base and continuing to apply force to the plunger with the press. If the ejection force is being measured with a load cell, the maximum ejection force and the resistance from wall friction can be measured and compared with simulations as an additional check. This may be important as wall friction is known to be the single greatest source of density variation in green bodies[63].

The loading was applied using a 100kN electromechanical universal testing machine (Beta 100 from Messphysik Materials Testing). The target crosshead speed was kept to a low value 0.01mm/s , but the actual value varied due to the compliance in the press (see Figure 4.1). The actual displacement of the crosshead was measured with a PY-2-F-010-S01M external displacement transducer from Gefran Italy.

While disk forming experiments are fairly simple, a serious issue that arose during the initial data acquisition phase was that of variability (inability to reproduce the test). After performing several disk-forming experiments with the same amount of powder and the same loading conditions, the stress-strain path was observed to be significantly different from the previous sample. The solution to this problem is to vibrate the samples prior to compaction. The samples were vibrated (mold and powder) for approximately 10s at a low, variable frequency $< 350\text{Hz}$. The density of the alumina powder before vibration was measured to be 1119kg/m^3 with a standard deviation of 28kg/m^3 and after vibration the average density was measured to be 1320kg/m^3 with a standard deviation of 14kg/m^3 . Thus, vibration ensures a more consistent initial configuration in the grains, as is evidenced by the 50% reduction in the standard devia-

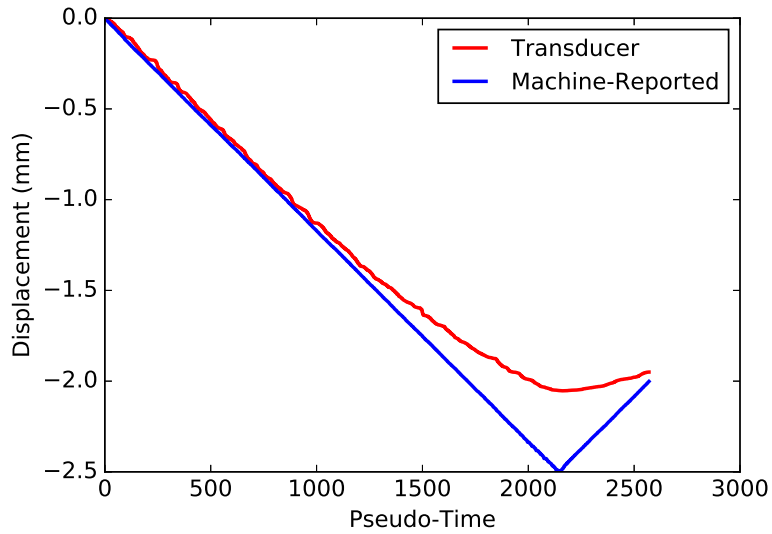


Figure 4.1: A demonstration of the difference of the machine-reported crosshead displacement with the displacement as measured by a transducer for a disk-forming experiment with a maximum load of approximately 56kN. The press is a Beta 100 from Messphysik Materials Testing and the transducer is a PY-2-F-010-S01M external displacement transducer from Gefran Italy. The working limit of the equipment (press and load cell) is 100kN.

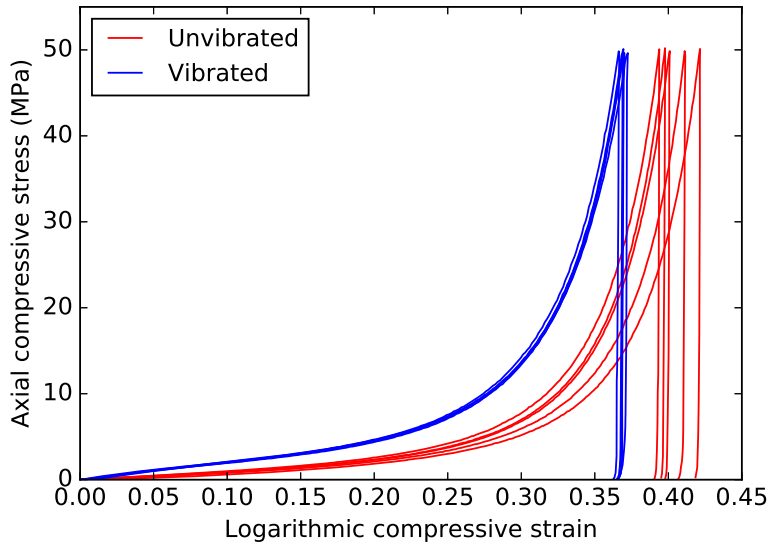


Figure 4.2: A demonstration of the effects of vibrating the sample while in the mold prior to the test. Each test is of 6g of alumina powder. Note the significant difference in strain to produce the same target stress between vibrated and non-vibrated samples. The average initial density of the unvibrated samples is 1120kg/m^3 and 1320kg/m^3 for the vibrated samples.

tion of densities. Ensuring that the initial response of the samples is uniform across tests is imperative as variability is less pronounced with increasing pressures[20]. Figure 4.2 contains a comparison of five non-vibrated samples and five vibrated samples of 6g each, compressed to 50MPa. As consistency is key for parameterization, unless otherwise noted, all samples for all tests have been vibrated prior to being testing. However, the efficacy of vibrating the samples before loading was observed to decrease with increasing sample size, but.

Another characteristic of the disk-forming experiments is that of wall friction and aspect ratio. As the aspect ratio increases, the effect of friction against the die wall increases[13]. These effects include artificial stiffness as the load is transferred to the die and density heterogeneities. The best method for decreasing the effects of friction is to have a very low-aspect ratio sample.

4.1.2 Ultrasonic Measurement of Elastic Parameters

After a variety of disks have been formed at a variety of pressures as described in Section 4.1.1, those disks can then be analyzed using ultrasonic measurement techniques. The data used in the parameterization is the same data that was presented by Argani et al[4].

In their paper, the authors use pressure and shear waves to measure the sound speed through the samples in the axial direction. Then, knowing the sample density, the elastic moduli can be calculated by the relation

$$G = \rho c_t^2 \quad M = \rho c_l^2 \quad (4.1)$$

where c_l and c_t are the longitudinal and shear wave speeds, respectively.

From multiple evaluations at different forming pressures, elastic moduli evolution can be determined as a function of forming pressure. However, these measurements only represent the elastic behavior in the axial direction whereas the elastic behavior in cold, quasi-isostatically pressed green bodies have been shown to behave anisotropically[38][40][39].

4.1.3 Triaxial Compression and Extension

The triaxial compression and extension data come from unpublished experiments performed by Bosi[8]. These tests were performed on the same alumina powder, KMS-96, but were not vibrated prior to loading.

The tests focused on the behavior of green bodies that have been hydrostatically compressed up to 40MPa. After that peak pressure has been reached, the sample is unloaded hydrostatically to the target initial pressure from which the triaxial compression test begins with increasing force in the axial direction or the triaxial extension test begins with increasing lateral pressure. The benefits of triaxial testing data are twofold: the ability to measure the elastic response (Young's modulus) and the ability to probe the shape of the yield surface.

There are several issues with the data that is reproduced here. The most critical shortcoming is that the lateral deformation could not be measured which leaves the actual stress unknown. Bosi attempts to correct for this by assuming that the sample is incompressible starting with the beginning of the triaxial loading, as opposed to assuming constant cross-sectional area (the two extremes). Both stress curves are shown in this work but only the portion of the data where there is less than 1% discrepancy between the constant-cross section stress and the incompressible stress is used.

The second issue with the data is that the loading history for the 5MPa triaxial compression data was incomplete, in such a way that the displacement data was unusable but the stresses were still valid. So, the 5MPa test is missing from the stress-strain plots but is present when attempting to parameterize the yield surface.

Finally, the third issue is due to limitations with the testing equipment that was used to perform the triaxial testing and the fact that it could not perform triaxial extension tests in a computer-controlled fashion. As such, the triaxial extension tests were erratic with large testing artifacts. Because of these limitations, only the yield surface points on the meridional profile are used, and then with skepticism.

4.2 Hydrostatic Limit Parameters

This section will show how to determine the values for the compressive hydrostatic limit parameters P_{c0} , a_1 , a_2 , Λ_1 , and Λ_2 using disk-forming experiments. All of these parameterizations will suffer from the same uncertainty in the lateral stresses (related to an unknown Poisson's ratio) as well as uncertainty in the shape of the yield surface.

Because the powder is assumed to always have some plastic flow for increasing pressure, the stress state is always on the yield surface for monotonically-increasing hydrostatic pressure. Because the stress state during disk formation is not hydrostatic loading, the pressure of

the current stress state will always be lower than the pressure cutoff.

The hydrostatic limit parameters describe the point where the yield surface intersects the compressive hydrostat and not the pressure at the current stress state. For this reason, it is not sufficient to know how Poisson's ratio evolves with respect to pressure because there would still be insufficient information about the shape of the yield surface and the actual, path-dependent lateral stresses.

These two uncertainties have opposite effects on the parameters. If we assume $p = -\sigma_a$, where p is the pressure of the current stress state and σ_a is the axial stress, then p is an upper-bound for the actual pressure because the material is compressible ($\nu < 1/2$). However, because of the unknown shape of the yield surface, it is only known that the pressure cutoff $p_c > p = -\sigma_a$ (assuming $\nu = 0$). Therefore, we can, with reasonable confidence, determine the parameterization to within a factor of 3, as well as deduce some hard limits to guide optimization through inverse analysis.

4.2.1 Initial Pressure Cutoff p_{c0}

This value should simply be small, but non-zero. The simplest and most accurate value would be to determine the mass exerted by the dead weight of the plunger and determine an order-of-magnitude value for p_{c0} , from the hard minimum value, using

$$p_{c0} = \frac{Mg}{3\pi r^2}, \quad (4.2)$$

where M and r are the mass and radius of the plunger and g is acceleration due to gravity. This assumes that, for the uncompressed powder, Poisson's ratio is zero. For $M = 0.4\text{kg}$, $g = 9.81\text{m/s}^2$, $r = 15\text{mm}$ the associated initial pressure cutoff is

$$p_{c0} \approx 1850\text{Pa}. \quad (4.3)$$

However, it has been found that p_{c0} can be several orders of magnitude higher without noticeably affecting the results while also significantly decreasing computation time.

4.2.2 Initial Cohesion c_I

As a loose powder has essentially zero cohesion, this value should simply be set to zero or to some small value with respect to p_{c0} or Λ_1 :

$$c_I = 1000\text{Pa}. \quad (4.4)$$

4.2.3 Cooper-Eaton Compaction ($a_1, a_2, \Lambda_1, \Lambda_2$)

The Cooper and Eaton compaction law[25], as implemented in the material model **Tridentum**, is governed by four parameters and can be parameterized from a set of disk-forming experiments. The maximum axial stress of each of the experiments should be chosen so as to give better coverage to the lower pressures. This allows better resolution of the compaction behavior during the initial phases of compaction where curvature is higher in stress-plastic strain space. As an example, nine different disk-forming experiments were used with maximum axial stresses of 6, 8, 10, 15, 20, 30, 40, 60, and 80MPa. This was found to give reasonable coverage for all parts of the compaction process, but additional tests at or above 100MPa would increase confidence in the fit.

For these tests it is imperative that the samples be as close to the same as possible. The amount of powder should be tightly controlled, placed in the mold, then thoroughly vibrated before loading to give consistent results.

For this parameterization, each disk-forming experiment provides one data point for fitting. This data point is comprised of the logarithmic volumetric plastic strain ($\text{tr } \varepsilon_p$) and the maximum axial stress. To calculate the volumetric plastic strain, the required measurements are: 1) The initial height of the powder before compaction h_o 2) the mold radius r_0 3) the final height of the disk after compaction and ejection h_f 4) the final radius of the disk after compaction and ejection r_f . It is given by

$$\text{tr } \varepsilon_p = \ln \left(\frac{h_f}{h_o} \right) + \ln \left(\frac{r_f}{r_0} \right) + \ln \left(\frac{r_f}{r_0} \right) = \ln \left(\frac{h_f r_f^2}{h_o r_0^2} \right). \quad (4.5)$$

The formulation of the Cooper-Eaton compaction law has been modified from its original form to increase numerical stability. This was accomplished by removing the non-physical zero-slope section around zero pressure. The relation, as implemented in **Tridentum**, is

$$e^{\text{tr } \varepsilon_p} = 1 - a_1 g(p_c, \Lambda_1) - a_2 g(p_c, \Lambda_2) \quad (4.6)$$

where

$$g(p_c, \Lambda) = \begin{cases} \frac{p_c}{\Lambda e}, & \text{if } p_c < \Lambda \\ e^{-\Lambda/p_c}, & \text{otherwise} \end{cases}. \quad (4.7)$$

There is one simple constraint for decreasing the search space for the a -parameters which utilizes the bulk density ρ_0 and theoretical

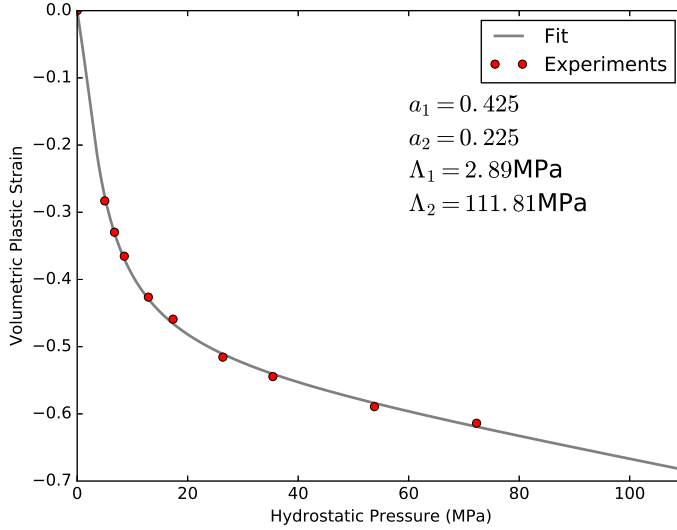


Figure 4.1: Plot of the experimental data and the calibrated Cooper-Eaton compaction law.

density ρ_∞ , which are approximately 1320kg/m^3 and 3900kg/m^3 respectively. The constraint relationship is given by

$$\frac{\rho_0}{\rho_\infty} = e^{\text{tr}\varepsilon_p} = 1 - a_1 - a_2 \quad (4.8)$$

or

$$1 - \frac{\rho_0}{\rho_\infty} = a_1 + a_2 \approx 0.65 \quad (4.9)$$

Utilizing this constraint ensures that only the proper amount of volumetric plastic strain is possible, even when subjected to infinite pressure.

Numerical optimization was used to find the compaction law parameters, using the RMS error between experimental and computed responses. Because the actual relationship between the stress state and the hydrostatic limit is unknown, the absolute value of the stress was used in the place of p_c . The Cooper-Eaton hardening law was found to fit the experimental data very well (see Figure 4.1).

The parameters are

$$a_1 = 0.425 \quad (4.10)$$

$$a_2 = 0.225 \quad (4.11)$$

$$\Lambda_1 = 2.89\text{MPa} \quad (4.12)$$

$$\Lambda_2 = 111.81\text{MPa}. \quad (4.13)$$

Because this parameterization also suffers from the fact that the transverse stresses and yield surface shape are unknown, the parameters should not be accepted as completely correct. At the end of initial parameterization these parameters will be optimized through the process of inverse analysis.

4.3 Elasticity

The elastic behavior of *Tridentum* is governed by seven different parameters: λ_I , μ_I , n , l , k_{II} , μ_{II} , and χ_e . The first four parameters are the only active parameters in the no-stress, loose state. With the introduction of any volumetric plastic strain the remaining three parameters become active. This makes parameterizing the elastic behavior very difficult as, except for the trivial zero-stress state, there are seven parameters that are controlling some portion of the elastic behavior which is coupled to the plastic response.

There are three different types of tests that were used for the parameterization of the elastic response. These tests were discussed individually in Section 4.1.1, Section 4.1.2, and Section 4.1.3. In the following sections the types of tests are discussed specifically concerning elastic behavior.

4.3.1 Elastic Response from Ultrasonic Tests

Obtaining elasticity behavior parameters from the ultrasonic tests is fairly straightforward. The data that comes directly from the analysis are values of the constrained modulus and shear modulus for various forming pressures.

To determine the elastic parameters for the loose powder phase and for the fully condensed phase it is necessary to fit the interpolating function. Following one of the suggestions by Argani et al.[4], the transition law was chosen to be

$$M = e^{-\chi_e p_c} M_I + (1 - e^{-\chi_e p_c}) M_{II}, \quad (4.14)$$

where M is the constrained modulus or any other elastic modulus (such as λ , μ , E , or K). It is assumed that all aspects of the elastic response transition at the same rate (χ_e is the same for all parameters).

The ultrasonic measurement data provides the basis for determining χ_e through fitting the transition law to the data (see Figure 4.1). Again, the objective function of the optimization routine is the RMS

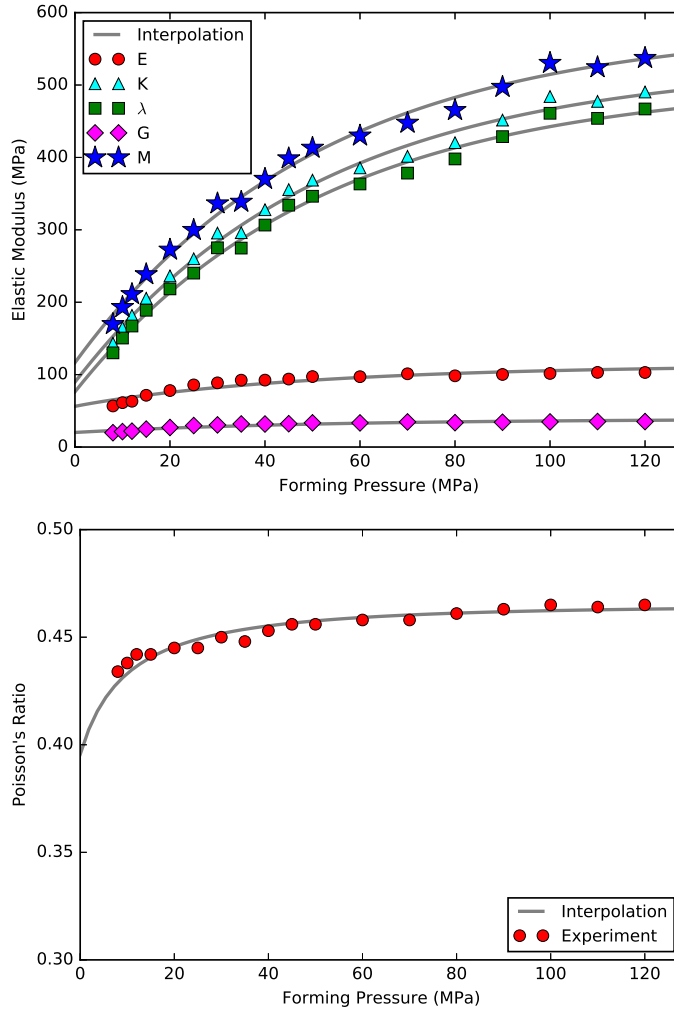


Figure 4.1: Plots of the elastic moduli (top) and Poisson's ratio (bottom) with respect to forming pressure for alumina powder. In each plot, the markers represent the ultrasonic experimental data and the solid lines represent the model interpolation function.

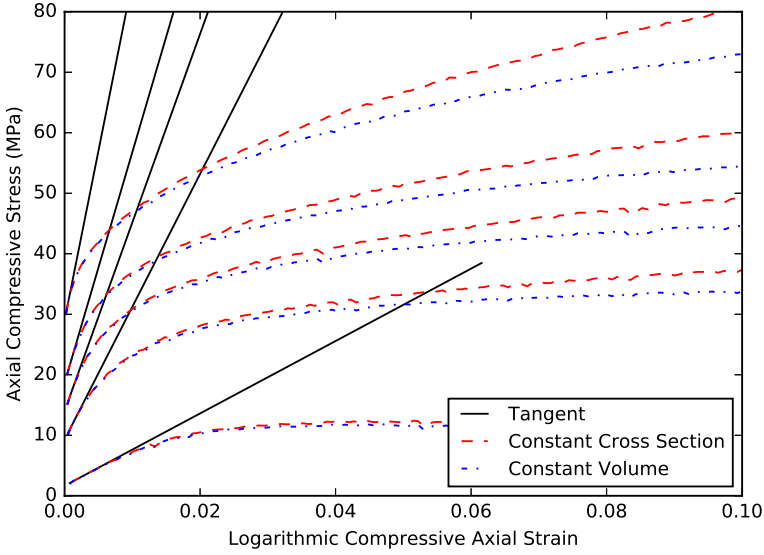


Figure 4.2: Compressive axial stress versus compressive axial strain from triaxial compression tests of alumina powder. The triaxial tests were all loaded hydrostatically to 40MPa, then unloaded hydrostatically to one of 2MPa, 10MPa, 15MPa, 20MPa, and 30MPa. At that point, the lateral stresses were held constant with increasing axial pressure. The dashed lines represent stress assuming a constant cross-section during compression and the dashed-dotted line assumes constant volume. Young's modulus was calculated from the initial slopes as 0.59GPa, 2.19GPa, 3.12GPa, 3.81GPa, and 5.60GPa for the 2MPa, 10MPa, 15MPa, 20MPa, and 30MPa tests, respectively, and is depicted by the solid tangent lines.

error between the experimental data and the interpolated function. The values obtained by this method are

$$\lambda_I = 76.2 \text{ MPa} \quad (4.15)$$

$$\mu_I = 20.1 \text{ MPa} \quad (4.16)$$

$$K_{II} = 530.2 \text{ MPa} \quad (4.17)$$

$$\mu_{II} = 38.7 \text{ MPa} \quad (4.18)$$

$$\chi_e = 1.933 \times 10^{-8} \text{ Pa}^{-1}. \quad (4.19)$$

4.3.2 Elastic Response from Triaxial Compression Tests

The triaxial compression tests yield five different stress-strain relations for equivalent amounts of volumetric plastic strain. The samples are loaded hydrostatically to 40MPa and then unloaded to the target initial pressure. From there, the triaxial compression tests begin with the initial portion of the curve being elastic. The plot in Figure 4.2 depicts the reported stress-strain relations (both the aforementioned incompressible and constant cross-section stresses) as well as tangent lines for the initial slope. The slope of these tangent lines is, by definition, Young’s modulus.

However, the data does not give a consistent value for Young’s modulus between each experiment, with the values ranging from 0.59GPa to 5.60GPa. While the nonlinear elastic law implemented in *Tridentum* does account for some strain-induced anisotropic stiffening, it does not allow hydrostatic elastic strains to stiffen in non-bulk modes. Therefore, the singular value taken from these tests is the average of the values of Young’s modulus for a sample precompressed to 40MPa

$$E_{40\text{MPa}} = 3.06\text{GPa}. \quad (4.20)$$

However, it is exceedingly interesting to note the monotonic stiffening for increasing volumetric elastic strains which could be a direction for future investigation.

4.3.3 Elastic Response from Disk-Forming Tests

In a similar way to the triaxial compression tests in Section 4.3.2, it is possible to determine the constrained modulus from the unloading path of the disk-forming tests. Because the stress state is continuously plastic throughout the entirety of the loading phase, when the loading direction changes the response is elastic.

The constrained modulus M is, by definition, the slope of the elastic stress-strain path under uniaxial strain. The plot in Figure 4.3 depicts the final section of the stress-strain path for three tests of 4g alumina samples undergoing compression to 40MPa, 60MPa, and 80MPa. The black lines along the unloading curve were calculated using a linear regression on all the unloading points and discarding “tail” points until the fit parameter $r^2 \geq 0.95$.

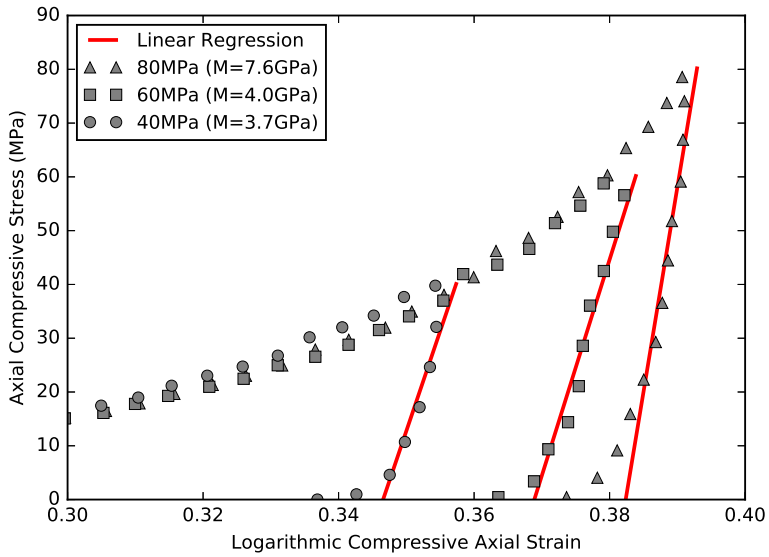


Figure 4.3: The tail-end of compressive axial stress versus compressive axial strain of uniaxial strain compression tests on alumina powder. The black lines are the linear regressions of the unloading portion, neglecting the spurious tail. The slope of the linear regressions are, by definition, the constrained modulus.

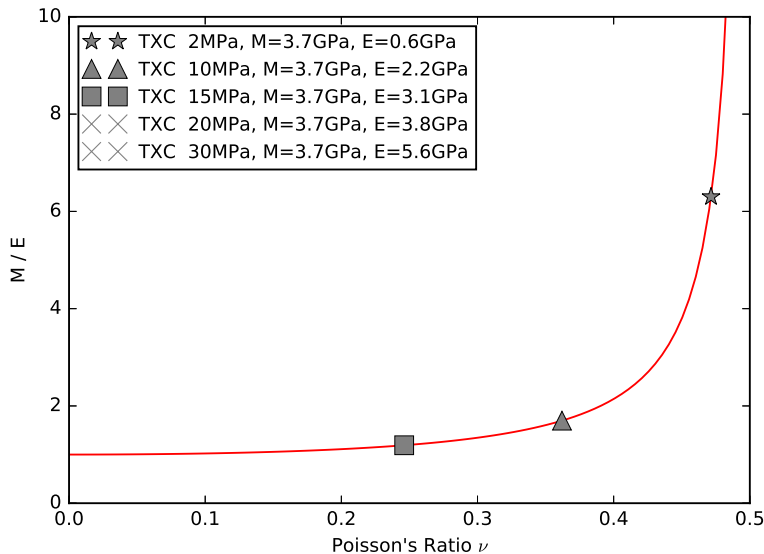


Figure 4.4: The ratio of the constrained modulus to Young’s modulus versus Poisson’s ratio. This plot is a union of the elastic modulus information from the triaxial compression data (Figure 4.2) and the uniaxial strain data (Figure 4.3). Compare the range of Poisson’s ratios with that of the ultrasonic test data (Figure 4.1). Note: the last two points (with “X” markers) are undefined as M cannot be less than E (which would yield an imaginary Poisson’s ratio).

The values that were found by the linear regression are

$$M_{40\text{MPa}} = 3.7\text{GPa} \quad (4.21)$$

$$M_{60\text{MPa}} = 4.0\text{GPa} \quad (4.22)$$

$$M_{80\text{MPa}} = 7.6\text{GPa}. \quad (4.23)$$

4.3.4 Unifying Elasticity Parameters

There is an old saying used by sailors in the 19th century that says “Never go to sea with two chronometers, take one or three.” The purpose of an accurate chronometer is that it allows a sailor to determine his longitude using only a sextant, the sun, and a chronometer. The purpose of three chronometers, as opposed to two, is that if two agree and one is wrong it is most likely to be that the two chronometers are correct.

In this situation, the data from Section 4.3.1 is an order of magnitude smaller than the data from Section 4.3.2 or Section 4.3.3.

To analyze the values from the triaxial compression data from Section 4.3.2 and the uniaxial strain data from Section 4.3.3 it is convenient to cast the Young's modulus data and the constrained modulus data into values of Poisson's ratio. As all of the elastic moduli are homogeneous functions of degree one, the ratio of constrained modulus to Young's modulus can be uniquely mapped to Poisson's ratio for all non-negative values of Poisson's ratio. Figure 4.4 maps the multiple values for Young's modulus from the triaxial compression data along with the single constrained modulus value for 40MPa to values of Poisson's ratio. The points associated with the higher hydrostatic pressures are non-physical as the larger values of Young's modulus cannot be greater than the constrained modulus.

It's interesting to note that the lower Young's modulus value yields a value of Poisson's ratio that is most in agreement with the Poisson's ratio data from the ultrasonic measurements. The other values of Young's modulus are more closely grouped but still exhibit consistent stiffening with higher amounts of volumetric elastic strain. These larger values of Young's modulus associated with greater volumetric elastic strains actually push the Poisson's ratio trend towards zero, which seems to contradict intuition for stiffening.

To cast further doubt on the situation, Lambe[50] gives an estimate of Young's modulus for various sands undergoing initial loading (loose sands). His estimate ranges from 14MPa for a loose sand with angular, breakable particles to 103MPa for a dense sand with hard, rounded particles. Which is in agreement with the initial elastic behavior predicted by the ultrasonic measurements $E_I = 50.6\text{MPa}$.

Given the mechanical, real-world nature of the triaxial and uniaxial tests, the magnitude of the elastic moduli should agree with those whereas the trend and approximate relations should be taken from the ultrasonic data. Thus, to bring the ultrasonic predicted value $M_{40\text{MPa}}$ into agreement with the uniaxial data for the same forming pressure, the elastic moduli should be multiplied by a factor of 10.08, yielding

$$\lambda_I = 768.1 \text{ MPa} \tag{4.24}$$

$$\mu_I = 202.6 \text{ MPa} \tag{4.25}$$

$$K_{II} = 5,344.9 \text{ MPa} \tag{4.26}$$

$$\mu_{II} = 390.1 \text{ MPa} \tag{4.27}$$

$$\chi_e = 1.933 \times 10^{-8} \text{ Pa}^{-1}. \tag{4.28}$$

These parameters should only be used as a starting point and guides for inverse analysis. Optimization should be done with both these parameters and those at the end of the ultrasonic measurement section (Section 4.3.1), and the final values compared.

4.4 Yield Surface Parameterization

The yield surface is a source of many of the nearly 30 parameters in *Tridentum*. There are six parameters for the powder phase yield surface and six more for the fully condensed phase yield surface with two speed parameters that govern the transition from powder to compacted phases. The powder phase parameters are c_I , η_I , m_I , α_I , β_I , and γ_I . The compacted phase parameters are c_{II} , η_{II} , m_{II} , α_{II} , β_{II} , and γ_{II} . The transition parameters are χ_c and χ_f which control the transition of the cohesion and the remaining yield function parameters, respectively.

Considering that the only yield surface data that is available is from the triaxial compression and extension tests which were performed with a precompression of 40MPa hydrostatic pressure, it is necessary to rely on the literature to guide the choice of parameters.

General information about parameterizing the BP yield surface for classic yield surfaces can be found in Appendix 3C.

4.4.1 Powder Phase Yield Surface Parameters

For the powder phase, it is assumed that the basic form of the yield surface is similar to the Mohr-Coulomb yield surface as the strength of loose sand is governed by frictional effects[32]. According to [65], the friction angle for quartz sand is anywhere from 22 – 35°. For the purposes of parameterizing *Tridentum*, a value of $\phi' = 30^\circ$ is assumed (near the middle of the range for quartz). The initial yield surface parameters are then

$$c_I = 1000.0 \text{ Pa} \quad (4.29)$$

$$\eta_I = 0.601 = 3\sqrt{2} \cos\left(\beta \frac{\pi}{6}\right) \frac{\sin(30^\circ)}{3 + \sin(30^\circ)} \quad (4.30)$$

$$m_I = 10.0 \quad (4.31)$$

$$\alpha_I = 0.05 \quad (4.32)$$

$$\beta_I = 0.247 = \sqrt{3} \left(\frac{4}{3 + \sin(30^\circ)} - 1 \right) \quad (4.33)$$

$$\gamma_I = 0.95 \quad (4.34)$$

where β_I and η_I are controlled by the friction angle and the remaining parameters c_I , m_I , α_I , and γ_I are variable, but are guided by the theory.

With regards to inverse analysis, the single most uncertain parameter is m_I because that controls the hydrostatic limit behavior which is not a part of the Mohr-Coulomb theory. The other parameters are more straightforward, with $c_I \rightarrow 0$, $\alpha_I \rightarrow 0$, and $\gamma_I \rightarrow 1$.

4.4.2 Compacted Phase Yield Surface Parameters

The fully condensed state yield surface is assumed to behave in a manner similar to condensed clay. For this reason, the Modified Cam-Clay model[64] was chosen to describe the meridional profile. The octahedral profile of the yield surface is allowed to vary to account for the asymmetry between triaxial compression and triaxial extension data. The only parameter for the Modified Cam-Clay model is referred to as M in the seminal paper and is equivalent to the parameter η_{II} . The paper[64] suggests setting η_{II} from the internal friction angle ϕ' using the following relation

$$\eta_{II} = \frac{6 \sin(\phi')}{3 - \sin(\phi')}. \quad (4.35)$$

To exactly mimic the Modified Cam-Clay model, the cohesion c_{II} should be set to zero, but the consolidated powder does have cohesive strength. However, at the point where the compacted phase becomes active, the preconsolidation pressure p_c is large enough that $c_{II} \ll p_c$, which yields a good approximation to the Modified Cam-Clay model while allowing for some cohesion.

Assuming, for simplicity, that ϕ' is equal to the friction angle for the powder phase ($\phi' = 30^\circ$), the basic parameterization is

$$c_{II} = 2.3 \text{ MPa} \quad (4.36)$$

$$\eta_{II} = \frac{6}{5} \quad (4.37)$$

$$m_{II} = 2 \quad (4.38)$$

$$\alpha_{II} = 1 \quad (4.39)$$

$$\beta_{II} = 1 \quad (4.40)$$

$$\gamma_{II} = 0. \quad (4.41)$$

The value for the cohesion of the fully condensed state c_{II} is taken from Stupkiewicz et al[68]. The value with the most uncertainty are η_{II} and the Lode angle-related parameters β_{II} and γ_{II} .

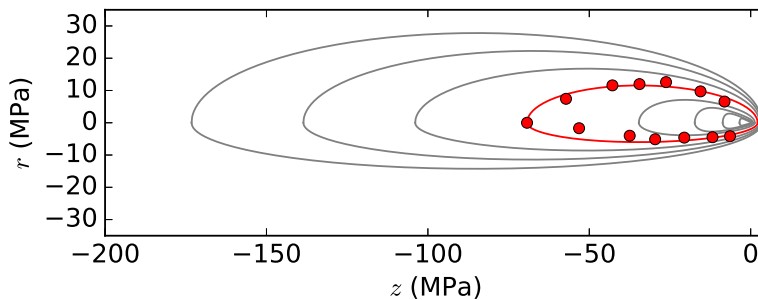


Figure 4.1: A plot in isomorphic stress space depicting the triaxial compression (positive r) and triaxial extension (negative r) experimental data with the evolution of the fitted yield surface. The red yield surface is the 40MPa yield surface that the data points were fitted to. The evolution of the yield surface is depicted with preconsolidation pressures of 2MPa, 5MPa, 10MPa, 20MPa, 40MPa, 60MPa, 80MPa, and 100MPa.

4.4.3 Using Triaxial Tests to Unify Yield Surface Parameterizations

From the triaxial compression and extension experiments performed by Bosi[8], there are 13 data points for the yield surface of alumina powder that has been hydrostatically pressed up to 40MPa. Of these, six are triaxial compression, six are triaxial extension, and one is hydrostatic compression. These points are used to fit the most uncertain parameters of the initial and final yield surfaces, namely m_I , η_{II} , β_{II} , γ_{II} , and the speed parameters χ_f and χ_c . The initial value for the optimization for finding χ_f and χ_c is to set them equal to χ_e . However, the effects of cohesion on the optimization problem is so small that it was necessary to set $\chi_c = \chi_f$ so that the optimizer would not drive χ_c to some nonphysical value.

The fitting process was done by minimizing the square root of the sum of the square of the differences between the experimental shear value and the associated shear limit on the yield surface for the same pressure and Lode angle. Acknowledging that the quality of the triaxial extension data is suspect, the objective function weighted the triaxial compression data 1000x more than the triaxial extension data, favoring a better triaxial compression fit. Figure 4.1 contains a plot of the experimental data along with several example yield surfaces to demonstrate the evolution with respect to increasing

consolidation pressures.

The final optimized parameters are

$$m_I = 10 \quad (4.42)$$

$$\eta_{II} = 0.349 \quad (4.43)$$

$$\beta_{II} = 0.0003 \quad (4.44)$$

$$\gamma_{II} = 0.999 \quad (4.45)$$

$$\chi_c = 1.04 \times 10^{-7} \text{MPa}^{-1} \quad (4.46)$$

$$\chi_f = 1.04 \times 10^{-7} \text{MPa}^{-1}. \quad (4.47)$$

Allowing m_I to change did not greatly effect the fit at 40MPa and so was left at $m_I = 10$. The highly skewed value β_{II} , which favors triaxial compression over triaxial extension, was not expected. Neither were the appearance of vertices (as $\gamma_{II} \rightarrow 1$) expected. The outcomes with β_{II} and γ_{II} might be an artifact of the poor triaxial extension data. At the current time, these values are acceptable, but will be further refined through inverse analysis.

4.5 Parameters Not Mentioned

Suspiciously absent from the sections above are the nonlinear-elastic powder-phase parameters, n_I and l_I , and the nonassociativity parameter ϵ . The nonlinear-elastic powder phase parameters were not addressed because the data available does not justify the use of a more complex elasticity relation than isotropic, linear elasticity. Also, up to this point no data has been presented that requires nonassociativity to describe the observed material behavior.

Thus, by Occam's razor, the parameters are set to $n_I = 2$ and $l_I = 1$ to mimic isotropic linear elasticity and $\epsilon = 0$ for associated flow.

For full-featured finite element simulations, Coulomb friction is assumed and a value of $\mu = 0.2$ is used based on the findings from Briscoe et al[14].

4.6 Inverse Analysis Using a Material Point Simulator

Having a tentative parameterization from the above sections, it is now possible to run simulations of the experiments that were used to parameterize `Tridentum` to assess the quality of the parameterization.

The method for running these simulations is to use a material point simulator to drive the material model.

A material point simulator is a program that directly interfaces with the material model to drive it according to a user-defined loading path. The primary benefits of using a material point simulator over a full-featured FE program is the simplicity and speed.

Material point simulators, take the concept of a single element test and simplify it. Single element tests still require the definition of an element type as well as load and/or displacement boundary conditions. Associated with those are hourglass stiffness, solver tolerances, and tabulating nodal displacements to give the desired input strains (which is nontrivial for non-axial loading). There are also inertial effects and rotations that may cause divergence from known solutions. Finally, there are licensing requirements, high start-up costs, and then postprocessing from (often proprietary) output databases.

A material point simulator does not deal with any of those issues because it only simulates a single integration point. All of the issues with choosing an element type, meshing, boundary conditions, and processing time are all non-existent.

A limitation of material point simulators is that the loading path must be formulated in terms of stresses and strains, because it has no context as it has no mesh. For the disk-forming experiments, this is not an issue: the disks were chosen to have a very low aspect ratio to minimize frictional effects and give a homogeneous response. Knowing the initial height, crosshead displacement, cross sectional area, and load, the stresses and strains are easily calculated.

4.6.1 Basic Response

Figure 4.1 contains plots comparing the tentative parameterization behavior with that of the disk-forming experiments. Considering the extreme uncertainty of the elastic behavior and the assumptions required to parameterize the yield surface, the fit is surprisingly accurate. However, the peak stress of the simulation of the 80MPa experiment is about 15MPa too low, but otherwise follows the loading curve rather well. The unloading legs also agree surprisingly well; but a two-fold increase or decrease in the constrained modulus would be nearly imperceptible in those plots.

The second plot in Figure 4.1 is the most important as it compares the simulated output with the highest quality data available. The axial plastic strain versus axial forming stress data is considered the highest quality data because these values are directly measurable

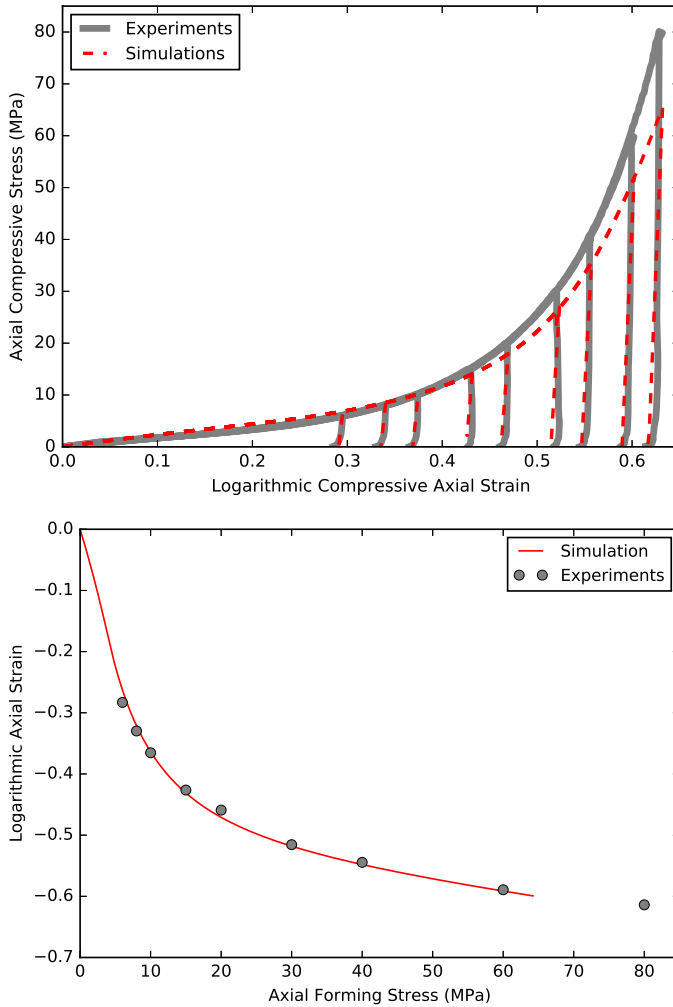


Figure 4.1: Plots comparing the simulated response using the tentative parameterization to the experimental data for disk-forming experiments. The upper plot shows the stress-strain response while the lower compares the axial stress and axial logarithmic plastic strain. Note, in the lower plot each data point represents a single disk-forming experiment.

through the load cell during pressing and with calipers before and after the experiment. For these reasons, the goodness of the initial fit bodes well for further improvements to the tentative parameterization through inverse analysis.

The alternative elastic behavior parameterization from the ultrasonic measurements was not pursued beyond this point due to the decency of the fit of the tentative parameterization, especially in comparison with the alternative behavior. Optimization was attempted, but was never able to produce an acceptable fit with elastic parameters similar to the parameters from the ultrasonic tests.

4.6.2 Optimized Response

At this point, there are several discoveries that have been made concerning the numerical implementation of the model and its behavior in simulations. The first, and probably most important, is that the initial consolidation pressure p_{c0} can be increased an order of magnitude or two without noticeably affecting the solution. This allows faster computation as well as more stable initial steps during compaction. This is because the initial steps induce copious amounts of volumetric plastic strain and push the capabilities of the return algorithm to the limit. By increasing p_{c0} several orders of magnitude, the yield surface is that much larger (decreasing local curvature) and the rate of parameter change (associated with the transition law) will decrease as the rate of change is greatest as $p_{c0} \rightarrow 0$.

The second discovery is the extent to which the model's response is dependent on time step size. The useful limit was found to be about 100 equally-spaced steps from powder to fully compacted. Beyond this level of refinement, the additional computational time does not produce significantly different solutions. The behavior under time step refinement is regular and converges. It is likely that time steps with logarithmic spacing would allow better integration for less computational effort.

A time-saving property of the disk-forming experiments is that, when optimizing against the axial stress-axial strain curve and the axial stress-axial plastic strain curve, it is only necessary to simulate the experiment with the highest axial stress and then only the loading portion. By comparing the axial plastic strains during loading, it is as if a multitude of loading/unloading simulations were done and compared. This has the benefit of cutting down on the computational costs, but also increases the information density of the objective function which makes the optimization better.

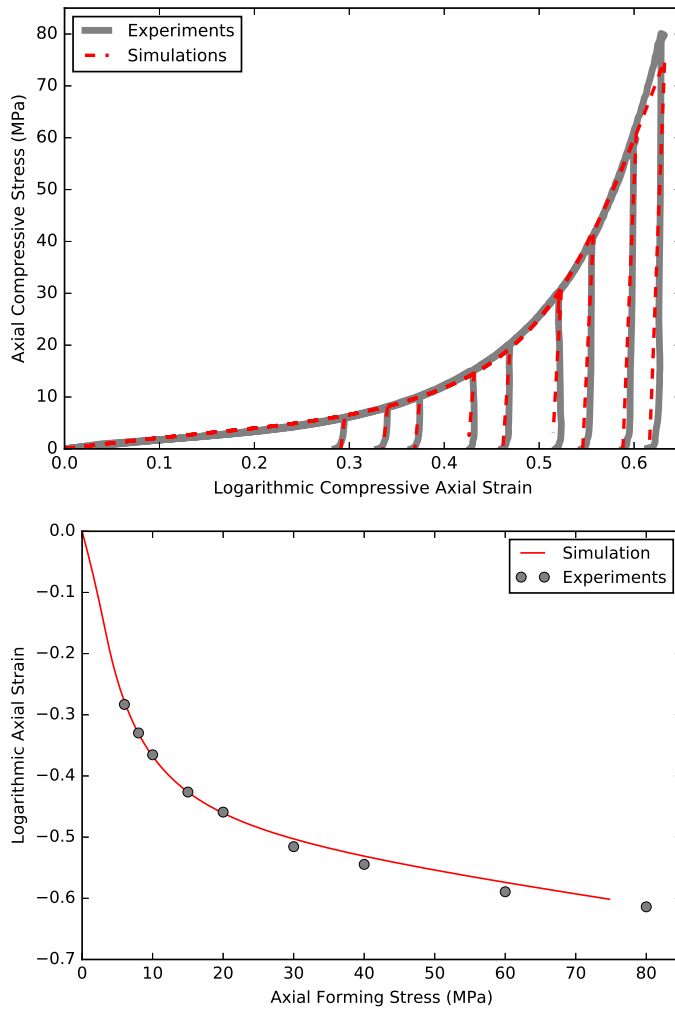


Figure 4.2: Plots comparing the simulated response using the optimized inverse-analysis parameterization to the experimental data for disk-forming experiments. The upper plot shows the stress-strain response while the lower compares the axial stress and axial logarithmic plastic strain. Note, in the lower plot each data point represents a single disk-forming experiment.

In the first round of inverse analysis, the only parameters to be optimized are the Cooper-Eaton parameters. These were chosen because they were originally parameterized under assumptions of lateral stresses, pressures, and yield surface shape.

The optimization was performed using the Nelder-Mead simplex method[56]. The optimized parameters and the percent increase or decrease are

$$a_1 = 0.405 \quad (-4.7\%) \quad (4.48)$$

$$a_2 = 0.263 \quad (+16.9\%) \quad (4.49)$$

$$\lambda_1 = 2.44\text{MPa} \quad (+18.4\%) \quad (4.50)$$

$$\lambda_2 = 113.9\text{MPa} \quad (+1.8\%). \quad (4.51)$$

At the conclusion of this round of optimization, further optimization was attempted with a broad range of parameters without any significant improvement in the fit. Therefore, this parameterization is in an optimal point (a local minimum). Confidence in the parameterization is gained by perturbing the parameters, optimizing, and finding similar parameters.

4.7 Conclusion

The numerical material model *Tridentum* has been parameterized using values from the literature and from experimental data. The experimental data is comprised of uniaxial strain disk-forming experiments, triaxial extension, triaxial compression, and ultrasonic measurement of the formed disks for elastic properties. After initial parameterization, further adjustments were made by inverse analysis using a material point simulator to drive the simulations. Using those resources for parameterization, *Tridentum* has been shown to reproduce the disk-forming stress-strain curves to acceptable levels. The next step is validation, where *Tridentum* is used to predict material behavior for a loading path on which it was not parameterized.

Appendix

4.A Tridentum Inputs for Alumina Powder

The table below lists all the model parameters for *Tridentum*, as well as the values used for an alumina powder, KMS-96.

Table 4.A.1: The final parameterization for the material model *Tridentum* for alumina powder.

#	Name	Value	Units (MKS)	Interval	Description
Elastic Parameters for Phase I (Powdered State) - See Equation 3.17					
1	λ_I	768.1×10^6	Pa	$(0, \infty)$	Elastic constant. If mimicing linear elastic response it is Lamé's first parameter.
2	μ_I	202.6×10^6	Pa	$(0, \infty)$	Elastic constant. If mimicing linear elastic response it is the shear modulus.
3	n	2.0	1	$[2, \infty)$	Elastic exponent. If linear elastic behavior is desired, n should be set to 2.
4	l	1.0	1	$[1, \infty)$	Elastic exponent. If linear elastic behavior is desired, l should be set to 1.
Elastic Parameters for Phase 2 (Solid State) - See Equation 3.18					
5	K_{II}	5.344×10^9	Pa	$(0, \infty)$	Linear elastic bulk modulus.
6	μ_{II}	0.390×10^9	Pa	$(0, \infty)$	Linear elastic shear modulus.
Initial Yield Surface Definition					
7	c_I	1.0×10^3	Pa	$[0, \infty)$	Initial tensile intercept of the yield function with the hydrostatic axis.
8	η_I	0.601	1	$(0, \infty)$	Meridional profile size parameter. The yield surface meridional profile is multiplied directly by η_I . If η_I is doubled, the shear required to cause yield is doubled for a given pressure.
9	m_I	10.0	1	$(1, \infty)$	Shape parameter that defines the meridional profile. Higher values of m_I cause the compressive cap to be flattened. As $m_I \rightarrow \infty$ the transition from shear-supporting to the pressure cutoff is a step function.

10	α_I	0.05	1	(0, 2)	Shape parameter that defines the meridional profile; α_I is a bias parameter. When $\alpha_I \rightarrow 0$ compressive states are more admissible, when $\alpha_I = 1$ the center of the yield surface is most admissible, when $\alpha_I \rightarrow 2$ tensile states are more admissible. Large values of m_I can undo the bias introduced by α_I .
11	β_I	0.247	1	[0, 2]	Shape parameter that defines the octahedral profile. This parameter controls the bias of the octahedral profile towards being stronger in either triaxial compression or triaxial extension. When $\beta_I = 0$ triaxial compression is more favorable; when $\beta_I = 2$ triaxial extension is more favorable; when $\beta_I = 1$ they are equally favorable.
12	γ_I	0.95	1	[0, 1)	Shape parameter that defines the octahedral profile. Qualitatively, it controls the 'pointiness' of the octahedral profile. When $\gamma_I=0$ the octahedral profile is always circular. When $\gamma_I \rightarrow 1$ vertices are possible at $\theta = 0, \pi/3$ (depending on the value of β_I).
Final Yield Surface Definition					
13	c_{II}	2.3×10^6	Pa	$[0, \infty)$	Final state value. See c_I above.
14	η_{II}	0.349	1	$(0, \infty)$	Final state value. See η_I above.
15	m_{II}	2	1	$(1, \infty)$	Final state value. See m_I above.
16	α_{II}	1	1	(0, 2)	Final state value. See α_I above.
17	β_{II}	0.0003	1	[0, 2]	Final state value. See β_I above.
18	γ_{II}	0.999	1	[0, 1)	Final state value. See γ_I above.
Hardening Law Parameters					
19	\tilde{a}_1	0.405	1	[0, 1]	Void ratio associated with the compaction mechanism that is active around a pressure of Λ_1 . Constrained by $\tilde{a}_1 + \tilde{a}_2 \leq 1$. Setting all hardening law parameters to zero gives perfect plasticity.
20	\tilde{a}_2	0.263	1	[0, 1]	Void ratio associated with the compaction mechanism that is active around a pressure of Λ_2 . Constrained by $\tilde{a}_1 + \tilde{a}_2 \leq 1$. Setting all hardening law parameters to zero gives perfect plasticity.

4. Parameterizing Tridentum for Alumina Powder KMS-96

21	Λ_1	2.44×10^6	Pa	$[0, \infty)$	Pressure value around which the compaction mechanism associated with \tilde{a}_1 is active. Setting all hardening law parameters to zero gives perfect plasticity.
22	Λ_2	113.9×10^6	Pa	$[0, \infty)$	Pressure value around which the compaction mechanism associated with \tilde{a}_2 is active. Setting all hardening law parameters to zero gives perfect plasticity.
Transition Parameters					
23	p_{c0}	1.85×10^4	Pa	$(0, \infty)$	Sets the initial value for p_c , the compressive intercept of the yield surface with the hydrostatic axis. In essence, the material has been subjected to the pressure p_{c0} then unloaded before the simulation begins.
24	χ_e	1.933×10^{-8}	1/Pa	$[0, \infty)$	Value controlling how quickly the elastic response evolves from the hyperelastic model (powder material) to the linear elastic model (compacted material).
25	χ_f	1.04×10^{-7}	1/Pa	$[0, \infty)$	Value controlling how quickly the yield surface evolves from the user-defined yield surface to the fully compressed yield surface.
26	χ_c	1.04×10^{-7}	1/Pa	$[0, \infty)$	Value controlling how quickly the cohesion evolves from c_I to c_{II} .
Non-associativity					
27	ϵ	0.0	1	$[0, 1]$	Associativity factor. Set to zero for associative plastic flow, unity for maximum non-associative flow, and a value between for less non-associativity.
Model Behavior Parameters					
28	ρ_0	1320.0	kg/m ³	$[0, \infty)$	Used only for output. Initial density at time t=0. If set to 1, relative density changes are tracked.
29	NSUB	0.0	1	$[0, \infty)$	Substepping limit. Allow 2^{NSUB} number of steps.
30	SQA	0.0	1	$(-\infty, \infty)$	When SQA is not zero the model prints copious amounts of material state information. Intended for developer use only.

Green Body Truncated Cylinder Experiment and Simulation Comparison

*The primary function of a material model is to predict material response for which no experimental data is available. The entire process leading up to this point is an attempt to glean information from simpler experiments so that more complex physics can be understood. This chapter presents the validation process of **Tridentum** by using the formation of a green body in the shape of a truncated cylinder using a ceramic powder (alumina, KMS-96). The experimental data is a 3D density field produced using the tomographic reconstruction method presented in Chapter 2. The simulation is performed with the commercial finite-element software Abaqus with **Tridentum** implemented as a user material subroutine. The simulated density field is also evaluated in the same manner as the experimental sample and those reconstructed fields are presented, along with the actual simulated density field.*

5.1 Introduction

The process of material model development has three primary phases: creation, verification, and validation. Simply put, verification is ensuring that the constitutive equations are being solved correctly whereas validation ensures that the correct equations are being solved. Chapter 1 advocates that the verification and creation steps should be inseparable and inextricably interwoven with each other. These first two steps are guided by physical phenomena inasmuch as the model is based on real-world observations, but are not in any way required to accurately model any real-world phenomena.

The final step, that of validation, is the process by which a model that has been created and verified is exercised to increase confidence in the predictions made. The benefits of validation are dependent on which validation tests are chosen. For example, validating the model against the data on which it was parameterized does not increase

confidence in the predictive capabilities. A test where the model is exercised in a different mode or even a similar mode but outside of the parameterization envelope could be beneficial to improving confidence.

Finally, when the model does not accurately describe the material behavior, validation is part of the larger process called uncertainty quantification. Uncertainty quantification finds error bars within which the correct solution is expected to reside. Thus, as Box and Draper stated[9] “all models are wrong, but some are useful”, and the level of usefulness is determined though extensive validation and uncertainty quantification.

5.2 Model Validation against Experimental Results

The usefulness of the model can only be determined by comparing the numerical simulations to real-world experiments that exercise the model in ways different from those used to parameterize the model. As the primary concern of the ceramics industry is the homogeneity of the green body, the best measure of predictability of our model is to compare computed and actual density fields for the experimental results.

To this end, it was decided to perform an experiment that is similar to the disk-forming experiments used to parameterize the model but that introduce more friction and also break axial symmetry. The geometry for the model was decided to be a truncated cylinder with a diameter of 30mm and an inclination of 10° . A diagram can be found in Figure 5.1.

Some additional reasons for using this simple experiment are that it introduces frictional effects, particularly on the inclined surface, and that the mold geometry is expected to yield a spectrum of densities. For the suggested 100MPa forming pressure, the anticipated density field should have densities higher than the nominal 2400kg/m^3 near the pinch point and should have lower densities at the tip of the inclined surface. Correctly predicting these densities is the primary goal of the model, but the final simulation behavior is intrinsically linked to the frictional behavior of the alumina powder on the steel mold. As the focus of this research is to produce a new powder compaction constitutive model and not to explore the difficulties of simulating frictional effects of a powder on steel, a simple Coulomb friction law was chosen. The coefficient of friction between

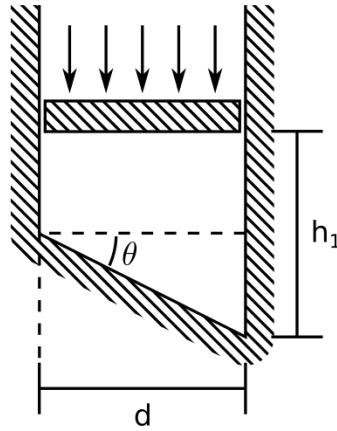


Figure 5.1: A cross-section of the truncated cylinder experimental setup.

the alumina powder and steel was assumed to be $\mu = 0.2$ based on ceramic green body ejection data from Briscoe[14].

5.3 Evaluation of the Predictive Capabilities

As was previously discussed, the most pertinent way to evaluate the utility of the present model is to compare the simulated density field to that of an experiment. Although there are many methods for density evaluation for green bodies, such as using scratch hardness[15] for local surface properties or x-ray attenuation[2], the method of choice for evaluating a green body density field is to use tomographic reconstruction on mass projections using a CNC[70]. The main benefit of this method is that it produces a 3D density field instead of only density at the surface or density along a line. Although mentioned in their paper, it should be noted that the tomographic reconstruction method proposed utilizes only two projections and, except in extremely pathological cases, does not reconstruct the actual field. However, if the evaluation and reconstruction steps are performed on two different fields and then those reconstructed fields compared it is possible to infer correlation in real space from correlation in reconstructed space. In this way the method still provides useful insight to density field evaluation even though it does not produce faithful representations of the actual fields.

As can be seen in Figure 5.1, the two reconstructed fields have a

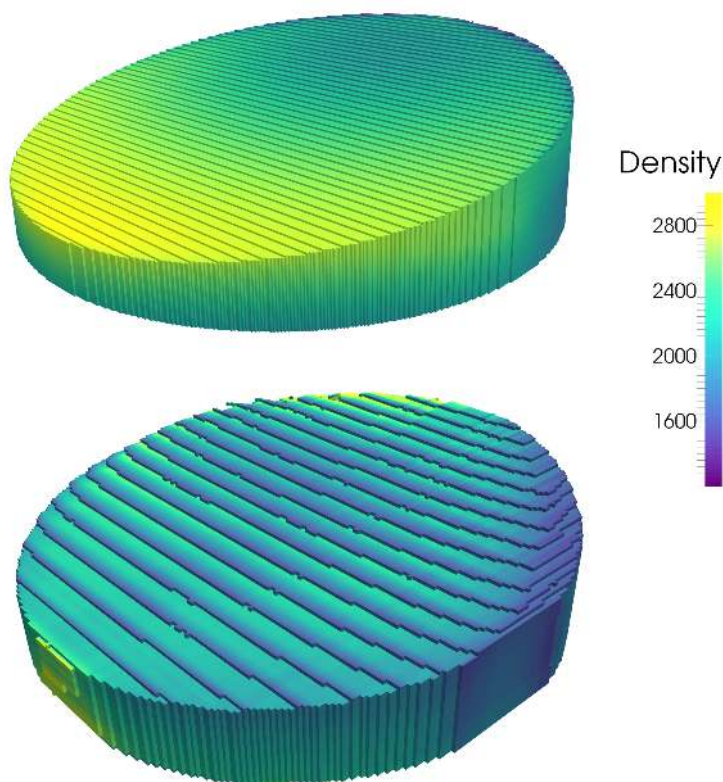


Figure 5.1: Comparison of the reconstructed density fields from the experiment (top) and the simulation (bottom) from the production of a truncated cylinder from alumina powder. All densities are given in kg/m^3 with $1200\text{kg}/\text{m}^3$ as the uncompressed powder density and $2400\text{kg}/\text{m}^3$ as the manufacturer-reported green density at 100MPa. The true measure of the accuracy of the model is related to how well the reconstructed fields agree. Regions of low density along the inclined surface of the simulation are non-physical effects of the reconstruction process.

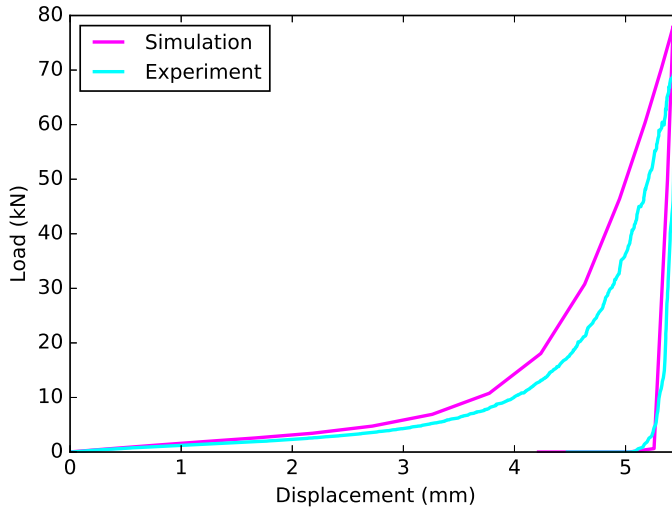


Figure 5.2: A comparison of the force-displacement data for the experiment and simulated green body forming. The simulation was driven by imposing a prescribed displacement on the punch. The excess simulated load is likely due to inaccuracies in the implementation of friction (e.g. incorrect friction coefficient or non-realistic friction law).

decent amount in common. It is readily visible that the maximum and minimum densities of the green body are very close to one another. It can also be seen that the sudden transition from high density to low density along the wall of the green body is present in the reconstructions from both the simulation and experiment. The crescent shape of high density that circles around from the pinch point along the sides of the inclined surface is also present.

Figure 5.2 presents the load versus displacement plots for the simulation and the experiment. While the simulated maximum load is about 10% higher than the experimental maximum load, this is assumed to be due to the effect of friction between the powder and the mold walls. This could be due to an incorrect coefficient of friction, which seems possible as the value of the coefficient of friction was based on ejection data and not compaction data. Another possible issue is that Coulomb friction is not the most accurate friction model to use in this case. Connected to both of these are the nearly limitless options available in commercial finite-element codes for implementing contact. As the focus of this research is the development of a model

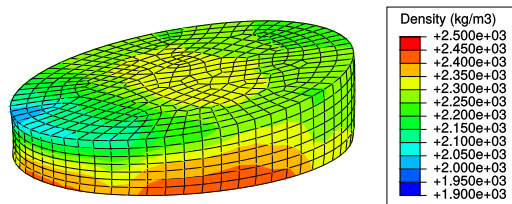


Figure 5.3: A 3D view of the final simulated density field. Inclined surface facing up.

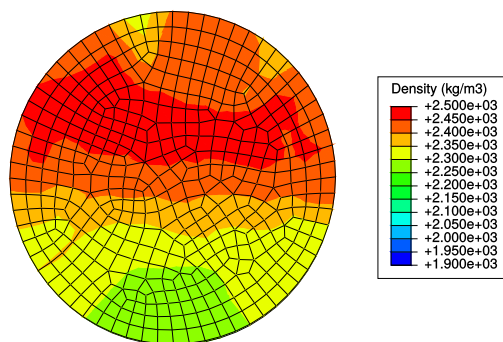


Figure 5.4: A view of the top (inclined surface) of the final simulated density field. Thinnest section on top.

and not the exhaustive evaluation of friction law implementations, the discrepancy is noted as a possible direction for future work.

While of no consequence to the actual comparison, it is interesting to note that the actual simulated density field has more gradual variations in the density field as well as the center of the inclined plane having a higher density than most of the edges. The reversal of the crescent shape on the inclined surface between the reconstructed field and the simulated field is not surprising. Because the reconstruction method uses only two projections and is constrained by the geometry of the piece, we expect the diffusion of the high-density area around the pinch point to be aggregated to the boundary, giving the reversal of the crescent. While not physical, it is expected.

Figures 5.3, 5.4, 5.5, and 5.6 show the density field of the sim-

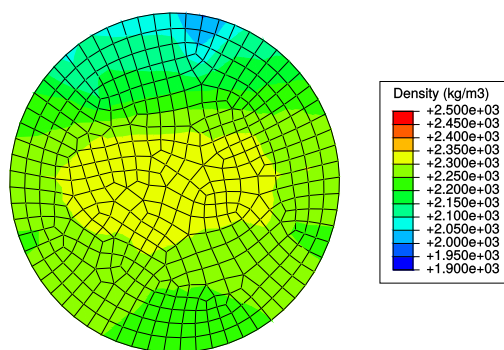


Figure 5.5: A view of the bottom (punch surface) of the final simulated density field. Thinnest section on top.

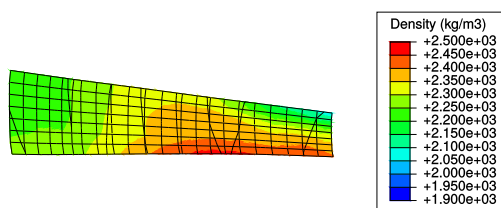


Figure 5.6: A view of the inside of the final simulated density field. Inclined surface facing up.

ulated green body. The reconstructed and simulated density fields all agree that there is a steep decrease in density near the halfway point in the direction from the thinnest point to thickest point (compare Figure 5.1 and Figure 5.3). However, beyond this large-scale trend, the reconstructed fields differ greatly from the simulated field, as expected.

A very intriguing issue with the simulated density fields (both reconstructed and actual) is that the density distributions do not have average values similar to that of the experimental density field. Figure 5.7 shows the probability density function and cumulative density function for the density fields. The median of the simulated density fields is in better agreement with the manufacturer-reported green density of 2400kg/m^3 , with a median value of 2320kg/m^3 , as opposed with the median of the reconstructed experimental field 2200kg/m^3 .

5.4 Conclusions

A novel ceramic powder compaction model is presented. It incorporates nonlinear elasticity, pressure- and Lode-angle-dependent yield surfaces, yield surface evolution, nonassociativity, and a special form of elastoplastic coupling. The model is capable of describing the entire spectrum of the compaction process, from the powder phase to the fully compressed phase and all the states in between. The predictive capabilities of the model were demonstrated with a comparison of density fields from a numerical simulation and an experiment. The density fields were compared in a reconstructed space after evaluating projections and reconstructing them using tomographic reconstruction methods. The reconstructed density fields agreed to a large extent and give confidence that the model is accurately predicting the actual density field of the green body. The model has been implemented into a numerical routine and shown to be able to give results in a reasonable amount of time using regular desktop computers, which would allow it to be used in industry and also smaller research institutions.

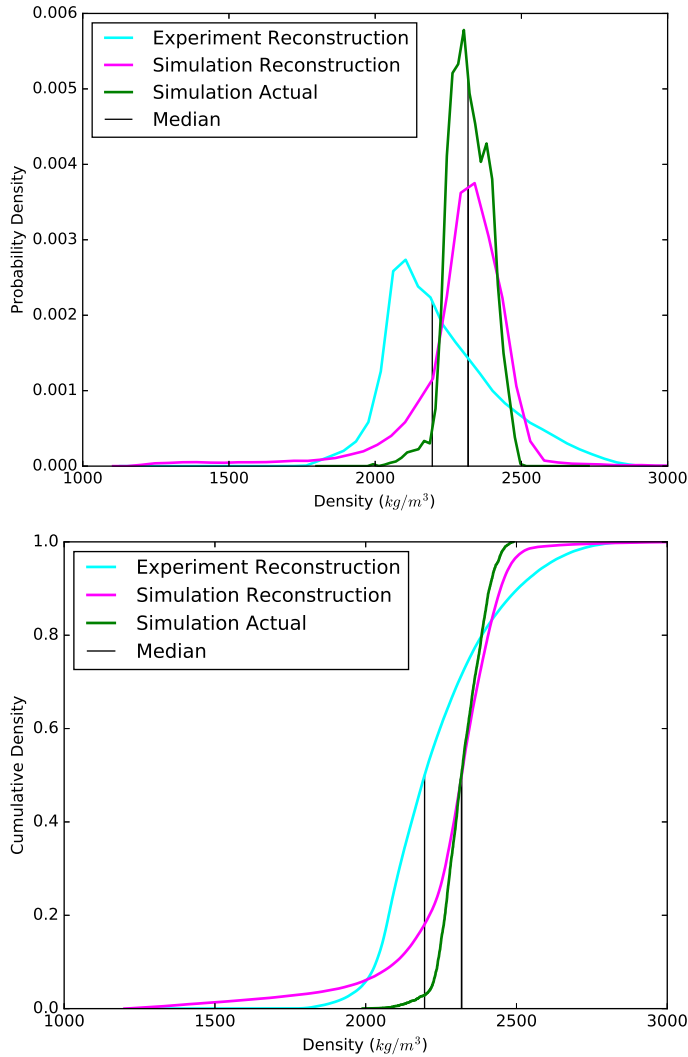


Figure 5.7: A probability density function (PDF) and cumulative density function (CDF) for the density distributions of the reconstructed experimental density field, reconstructed simulated density field, and the actual simulated density field. Note: the median values for the simulated distributions are coincident.

Conclusions

The results of the present research can be summarized as follows:

- A publication detailing the benefits of Test-Driven Development for constitutive models, with examples of tests and functioning example code, as well as new tests for material point simulators. Test-Driven Development advocates for shorter units of code with fewer branch points which, in turn, produces a lower fault density and easier unit testing of the sections of code. These things combine to produce objectively better, more readable code as well as the assurance that future code changes will not negatively impact current functionality.

In tandem with the release of the publication, an example Tresca model written in Python was published with all of the tests detailed in the publication implemented. This allows any researchers to reproduce the findings of the paper with ease, which is the cornerstone of good science.

- The development of a new density field evaluation method using a CNC mill and analytical balance. The method makes use of tomographic reconstruction techniques to visualize density fields, the accuracy of which is entirely dependent on the number and resolution of the projections used. However, it was found that even two projections can provide qualitative information on large-scale density variations.

This method is particularly well-adapted to universities and small research labs where density evaluations are infrequent, but can greatly aid the pace of research.

- The development and implementation of a numerical material model for simulating material response of ceramic powders undergoing cold, quasi-isostatic compression. The primary aspects of the model are elastoplastic coupling, phase transformations (from powder to fully condensed), pressure and Lode angle dependence of the yield surface, hardening, nonassocia-

tivity, nonlinear elasticity in the powder phase, and the ability to mimick many classical elastic and plastic models.

This model was developed using the programming paradigm of Test-Driven Development and was written in Fortran 95. There are currently over 500 automated tests (including unit, integration, and system-level tests) that can be compiled and run in under a minute. This ensures continued quality of the code and facilitates debugging.

- A demonstration of the efficacy of the aforementioned model to predict density fields in green bodies. The model performed well in predicting density fields and force-displacement response during a simulation forming a truncated cylinder green body. The tomographic reconstruction-based density evaluation method was used to compare the simulated and experimental green bodies.

Bibliography

- [1] Albemarle. *Martoxid KMS-96*, 1 2011.
- [2] J.L. Amorós, J. Boix, D. Llorens, G. Mallol, I. Fuentes, and C. Feliu. Non-destructive measurement of bulk density distribution in large-sized ceramic tiles. *Journal of the European Ceramic Society*, 30(14):2927 – 2936, 2010. Special Issue: 4th Conference on Shaping of Advanced Ceramics.
- [3] A.H. Andersen and A.C. Kak. Simultaneous algebraic reconstruction technique (sart): A superior implementation of the art algorithm. *Ultrasonic Imaging*, 6(1):81 – 94, 1984.
- [4] L.P. Argani, D. Misseroni, A. Piccolroaz, Z. Vinco, D. Capuani, and D. Bigoni. Plastically-driven variation of elastic stiffness in green bodies during powder compaction: Part I. experiments and elastoplastic coupling. *Journal of the European Ceramic Society*, 36(9):2159 – 2167, 2016.
- [5] D. Bigoni and D. Zaccaria. On the eigenvalues of the acoustic tensor in elastoplasticity. *European Journal of Mechanics - A/Solids*, 13(5):621–638, 1994.
- [6] Davide Bigoni and Andrea Piccolroaz. Yield criteria for quasibrittle and frictional materials. *International Journal of Solids and Structures*, 41(1112):2855 – 2878, 2004.
- [7] F. Bosi, A. Piccolroaz, M. Gei, F. Dal Corso, A. Cocquio, and D. Bigoni. Experimental investigation of the elastoplastic response of aluminum silicate spray dried powder during cold compaction. *Journal of the European Ceramic Society*, 34(11):2633 – 2642, 2014. Modelling and Simulation meet Innovation in Ceramics Technology.
- [8] Federico Bosi. Experimental data on alumina green body. FP7-PEOPLE-286110, 10 2011.

- [9] George EP Box and Norman Richard Draper. *Empirical model-building and response surfaces*, volume 424. Wiley New York, 1987.
- [10] R. M. Brannon and S. Leelavanichkul. A multi-stage return algorithm for solving the classical damage component of constitutive models for rocks, ceramics, and other rock-like media. *International Journal of Fracture*, 163(1):133–149, 2009.
- [11] Rebecca M. Brannon. Elements of phenomenological plasticity: Geometrical insight, computational algorithms, and topics in shock physics. In Yasuyuki Horie, editor, *ShockWave Science and Technology Reference Library*, pages 225–274. Springer Berlin Heidelberg, 2007.
- [12] R.M. Brannon. Functional and structured cartesian tensor analysis for engineers. Unpublished, December 2008.
- [13] B.J. Briscoe and S.L. Rough. The effects of wall friction in powder compaction. *Colloids and Surfaces A: Physicochemical and Engineering Aspects*, 137(1-3):103 – 116, 1998.
- [14] B.J. Briscoe and S.L. Rough. The effects of wall friction on the ejection of pressed ceramic parts. *Powder Technology*, 99(3):228 – 233, 1998.
- [15] Brian J. Briscoe and Sujeet K. Sinha. Density distributions characteristics of green ceramic compacts using scratch hardness. *Tribology International*, 30(7):475 – 482, 1997.
- [16] Philippe P. Bruyant. Analytic and iterative reconstruction algorithms in spect. *Journal of Nuclear Medicine*, 43(10):1343–1358, 2002.
- [17] E.J. Candes, J. Romberg, and T. Tao. Robust uncertainty principles: exact signal reconstruction from highly incomplete frequency information. *Information Theory, IEEE Transactions on*, 52(2):489–509, Feb 2006.
- [18] P. Carlone and G. S. Palazzo. Computational modeling of the cold compaction of ceramic powders. *International Applied Mechanics*, 42(10):1195–1201, October 2006.
- [19] K. Carlsson and M. Ekh. Constlab.jl, 2016. [Online; accessed 03-January-2017].

- [20] Tamara J. Carneim and David J. Green. Mechanical properties of dry-pressed alumina green bodies. *Journal of the American Ceramic Society*, 84(7):1405–1410, 2001.
- [21] David Carrington. Teaching software testing. In *Proceedings of the 2nd Australasian Conference on Computer Science Education*, ACSE '97, pages 59–64, New York, NY, USA, 1996. ACM.
- [22] J. Chakrabarty. In J. Chakrabarty, editor, *Theory of Plasticity (Third Edition)*. Butterworth-Heinemann, Oxford, third edition edition, 2006.
- [23] Fu-Pen Chiang. Moiré methods of strain analysis. *Experimental Mechanics*, 19(8):290–308, 1979.
- [24] Changho Choi. Development of an easy user interface for constitutive modeling of fine-grained soil. *KSCE Journal of Civil Engineering*, 10(6):419, 2006.
- [25] A. R. COOPER and L. E. EATON. Compaction behavior of several ceramic powders. *Journal of the American Ceramic Society*, 45(3):97–101, 1962.
- [26] Dassault Systemes Simulia Corp. *Abaqus User Subroutines Reference Guide*. Dassault Systems, 2014.
- [27] CR Dohrmann, MW Heinstein, J Jung, SW Key, and WR Witkowski. Node-based uniform strain elements for three-node triangular and four-node tetrahedral meshes. *International Journal for Numerical Methods in Engineering*, 47(9):1549–1568, 2000.
- [28] N.A. Fleck, H. Otoyoy, and A. Needleman. Indentation of porous solids. *International Journal of Solids and Structures*, 29(13):1613 – 1636, 1992.
- [29] A.F. Fossum and R.M. Brannon. The sandia geomodel: Theory and user’s guide. Technical Report SAND2004-3226, Sandia National Laboratories, August 2004.
- [30] T. Fuller, M.S. Swan, B. Leavy, and P. Newell. The material model laboratory, 2017. [Online; accessed 03-January-2017].
- [31] A. Gajo and D. Bigoni. A model for stress and plastic strain induced nonlinear, hyperelastic anisotropy in soils. *International Journal for Numerical and Analytical Methods in Geomechanics*, 32(7):833–861, 2008.

- [32] A. Gajo and D. Muir Wood. A kinematic hardening constitutive model for sands: the multiaxial formulation. *International Journal for Numerical and Analytical Methods in Geomechanics*, 23(9):925–965, 1999.
- [33] S. Jill Glass and Kevin G. Ewsuk. Ceramic powder compaction. *MRS Bulletin*, 22:24–28, 12 1997.
- [34] R. Gordon. A tutorial on ART (algebraic reconstruction techniques). *Nuclear Science, IEEE Transactions on*, 21(3):78–93, June 1974.
- [35] Richard Gordon, Robert Bender, and Gabor T. Herman. Algebraic reconstruction techniques (ART) for three-dimensional electron microscopy and x-ray photography. *Journal of Theoretical Biology*, 29(3):471 – 481, 1970.
- [36] A.L. Gurson. *Continuum theory of ductile rupture by void nucleation and growth. Part I. Yield criteria and flow rules for porous ductile media*. Sep 1975.
- [37] J.O. Hallquist and R.G. Whirley. *A material model driver for DYNA3D*. Feb 1990.
- [38] M. L. Hentschel and N. W. Page. Elastic properties of powders during compaction. part 1: Pseudo-isotropic moduli. *Journal of Materials Science*, 42(4):1261–1268, 2006.
- [39] M. L. Hentschel and N. W. Page. Elastic properties of powders during compaction. part 3: Evaluation of models. *Journal of Materials Science*, 41(23):7902–7925, 2006.
- [40] M. L. Hentschel and N. W. Page. Elastic properties of powders during compaction. part 2: elastic anisotropy. *Journal of Materials Science*, 42(4):1269–1278, 2007.
- [41] Nicholas J Higham. Computing the polar decomposition-with applications. *SIAM Journal on Scientific and Statistical Computing*, 7(4):1160–1174, 1986.
- [42] Michael A. Homel, James E. Guilkey, and Rebecca M. Brannon. Numerical solution for plasticity models using consistency bisection and a transformed-space closest-point return: a nongradient solution method. *Computational Mechanics*, 56(4):565–584, 2015.

- [43] International Programme on Chemical Safety. *International Chemical Safety Cards*, 2 2000.
- [44] Avinash C. Kak, Malcolm Slaney, IEEE Engineering in Medicine, and Biology Society. *Principles of computerized tomographic imaging*. IEEE Press, New York, 1988. Published under the sponsorship of the IEEE Engineering in Medicine and Biology Society.
- [45] Kamm, R. Steinberg, and M. A. Wulff. Lead-grid study of metal powder compaction. *Metals Technology*, December 1948.
- [46] K. T. Kim, S. W. Choi, and H. Park. Densification behavior of ceramic powder under cold compaction. *Journal of Engineering Materials and Technology*, 122:238 – 244, April 2000.
- [47] Attila Kossa and László Szabó. Exact integration of the von mises elastoplasticity model with combined linear isotropic-kinematic hardening. *International Journal of Plasticity*, 25(6):1083 – 1106, 2009.
- [48] H. Kostler, M. Prummer, U. Rude, and J. Hornegger. Adaptive variational sinogram interpolation of sparsely sampled CT data. In *18th International Conference on Pattern Recognition*, volume 3, pages 778–781, August 2006.
- [49] Y. S. Kwon, H. T. Lee, and K. T. Kim. Analysis for cold die compaction of stainless-steel powder. *Journal of Engineering Materials and Technology*, 119:366 – 373, October 1997.
- [50] T.W. Lambe and R.V. Whitman. *Soil Mechanics*. John Wiley & Sons, Inc., 1969.
- [51] W Lotmar. Apparatus for the measurement of retinal visual acuity by moiré fringes. *Investigative Ophthalmology and Visual Science*, 19(4):393, 1980.
- [52] J. Lubliner. *Plasticity Theory*. Macmillan, New York, 1990.
- [53] Y. K. Malaiya and J. Denton. Module size distribution and defect density. In *Proceedings 11th International Symposium on Software Reliability Engineering. ISSRE 2000*, pages 62–71, 2000.
- [54] S. Matej and R. M. Lewitt. Efficient 3D grids for image reconstruction using spherically-symmetric volume elements. *IEEE Transactions on Nuclear Science*, 42(4):1361–1370, Aug 1995.

- [55] E. M. Maximilien and L. Williams. Assessing test-driven development at IBM. In *25th International Conference on Software Engineering, 2003. Proceedings.*, pages 564–569, May 2003.
- [56] John A Nelder and Roger Mead. A simplex method for function minimization. *The computer journal*, 7(4):308–313, 1965.
- [57] Andrea Piccolroaz and Davide Bigoni. Yield criteria for quasi-brittle and frictional materials: A generalization to surfaces with corners. *International Journal of Solids and Structures*, 46(20):3587 – 3596, 2009.
- [58] Andrea Piccolroaz, Davide Bigoni, and Alessandro Gajo. An elastoplastic framework for granular materials becoming cohesive through mechanical densification. part I - small strain formulation. *European Journal of Mechanics - A/Solids*, 25(2):334 – 357, 2006.
- [59] Andrea Piccolroaz, Davide Bigoni, and Alessandro Gajo. An elastoplastic framework for granular materials becoming cohesive through mechanical densification. part II - the formulation of elastoplastic coupling at large strain. *European Journal of Mechanics - A/Solids*, 25(2):358 – 369, 2006.
- [60] J. Radon. On the determination of functions from their integral values along certain manifolds. *IEEE Transactions on Medical Imaging*, 5(4):170–176, Dec 1986.
- [61] M. Rajab and D. S. Coleman. Density distributions in complex shaped parts made from iron powders. *Powder Metallurgy*, 28(4):207–216, 1985.
- [62] D. Raparia, J. Alessi, and A. Kponou. The Algebraic Reconstruction Technique (ART). In *APS Meeting Abstracts*, May 1997.
- [63] F. Ren, E.D. Case, A. Morrison, M. Tafesse, and M.J. Baumann. Resonant ultrasound spectroscopy measurement of young’s modulus, shear modulus and poisson’s ratio as a function of porosity for alumina and hydroxyapatite. *Philosophical Magazine*, 89(14):1163–1182, 2009.
- [64] K. H. Roscoe. On the generalised stress-strain behaviour of ‘wet’ clay. *Engineering Plasticity*, pages 535–609, 1968.

- [65] A. SADREKARIMI and S.M. OLSON. Critical state friction angle of sands. *Geotechnique*, 61(9):771–783, 2011.
- [66] R.B. Seder. *Gallop!: A Scanimation Picture Book*. Workman Publishing Co., November 2007.
- [67] B.R. Seth. Generalized strain measure with applications to physical problems. Technical report, Wisconsin University - Madison Mathematics Research Center, Jul 1961.
- [68] S. Stupkiewicz, A. Piccolroaz, and D. Bigoni. Elastoplastic coupling to model cold ceramic powder compaction. *Journal of the European Ceramic Society*, 34(11):2839 – 2848, 2014. Modelling and Simulation meet Innovation in Ceramics Technology.
- [69] B. Su, S. Dhara, and L. Wang. Green ceramic machining: A top-down approach for the rapid fabrication of complex-shaped ceramics. *Journal of the European Ceramic Society*, 28(11):2109 – 2115, 2008.
- [70] M. Scot Swan, Andrea Piccolroaz, and Davide Bigoni. Application of tomographic reconstruction techniques for density analysis of green bodies. *Ceramics International*, 43(1, Part A):749 – 754, 2017.
- [71] G. Tassef. The economic impacts of inadequate infrastructure for software testing, 2002.
- [72] Joost Visser, Sylvain Rigal, Rob van der Leek, Pascal van Eck, and Gijs Wijnholds. *Building Maintainable Software, Java Edition: Ten Guidelines for Future-Proof Code*. O’Reilly Media, Inc., 1st edition, 2016.
- [73] L. Williams, E. M. Maximilien, and M. Vouk. Test-driven development as a defect-reduction practice. In *14th International Symposium on Software Reliability Engineering, 2003. ISSRE 2003.*, pages 34–45, Nov 2003.

The consistent, uniform pressing of green bodies is a necessary part of producing high-quality, high-performance ceramics with predictable qualities and behavior. Undesirable density variation in the compacted ceramic powder causes variability in performance, failure to meet quality control standards, and, possibly, complete piece failure during successive processing. These issues contribute directly to a decrease in production efficiency through lost time and an increase in energy and material use. The careful control of the green body density field is of the utmost importance to consistently producing high-performance ceramics. Current methods for minimizing heterogeneity of the density field are often based on trial-and-error to optimize mold geometry and forming pressure, which is both expensive and prolongs development. The present research presents a continuum-level constitutive model for accurately modeling the densification of ceramic powders into green bodies and outlines the numerical implementation of said model. The constitutive model incorporates nonlinear elasticity, elatic-plastic coupling, cap evolution, pressure- and Lode angle-dependent plasticity, and hardening. To evaluate the constitutive model, a new method for measuring density in green bodies has been developed. This method utilizes readily-available laboratory equipment to produce density projection data for the sample and subsequently processes that data to produce a 3D density field using well-developed tomographic reconstruction techniques. Finally, a green body is produced from alumina powder (Martoxid KMS-96) and the density field is evaluated and compared to that of a numerical simulation. They are shown to agree within the error of the density measurements. These comparisons demonstrate the performance of the developed constitutive model and the potential utility for companies and research institutions that are in the ceramics production field.

Matthew Scot Swan is a husband and father, as well as a scientist, researcher, material model developer, and open source contributor. He received a Bachelors degree in Physics and a Masters degree in mechanical engineering from the University of Utah. After two years of PhD studies at the University of California, San Diego, he transferred to the University of Trento in Trento, Italy, to complete his PhD studies.